Integration of Grid Forming Inverter Based Resources in Power Systems

Varun Nand

A thesis submitted to Auckland University of Technology in fulfilment for the requirements for the degree of

Master of Engineering

July 2026

School of Engineering, Computer and Mathematical Sciences

AUT

Supervisor: Dr. Zoey Zhou

Abstract

The rising global commitment into zero carbon emissions technologies for the future of energy security has led to increased investment in and adoption of renewable energy sources. This transition characterized by the rapid shift toward distributed energy resources and simultaneous the displacement of fossil fuel based synchronous generation has introduced specific challenges to the signal quality and operational stability of the electric grid.

The wide adoption of inverter-based resources for the integration of renewable energy on to the grid has led to the requirement of incorporating power quality and grid stability features in new smart inverters used in microgrids that connect to the wider power system. Though this is achievable on the large-scale generation of renewable power sources such as photovoltaic (PV) and wind, smaller utility scale distributed energy generation still requires more work.

This thesis presents the end-to-end design, implementation and real time hardware-in-loop (HIL) based simulation of a grid forming inverter capable of ancillary services and fault tolerance in order to maintain the power quality and system stability when integrated into the power grid. The MATLAB/Simulink based software environment, and the OPAL-RT HIL platform was used to implement a 100kW grid-forming inverter which was integrated into and grid connected microgrid to establish the core results of this thesis. The empirical data validated the efficacy of the implemented grid-forming inverter in maintaining transient and steady state stability in islanded and grid connected operational modes. The inverter asset demonstrated precise frequency and voltage regulation within the dynamic boundaries mandated by the New Zealand grid code. Furthermore, the inverter exhibited exceptional fault tolerance by successfully executing low voltage ride through (LVRT) during transient anomalies. Crucially, this structural reliance was achieved at the local inverter interface removing the need for load shedding schemes or the deployment of auxiliary flexible AC transmission system (FACTS) devices, while simultaneously satisfying New Zealand grid compliance and power quality benchmarks through the alignment with IEEE 519-2022 standard for harmonic compliance.

The research provides a blueprint for commercial operators to meet the operation constraints and grid compliance with the high-fidelity modelling of systems to evaluate and benchmark capabilities prior to commissioning of their renewable energy assets onto the power grid.

Attestation of Authorship

I hereby declare that this submission is my own work and that to the best of my knowledge and belief, it contains no material previously published or written by another person (except where explicitly defined in acknowledgements), nor material which to a substantial extent has been submitted for the award of any other degree or diploma of a university or other institution of higher learning.

Signed .....

Date: 06/07/2026

Dedication

To the scientists, engineers, researchers and educators who came before me: you are the giants on whose shoulders we stand.

This work is dedicated in reverence to you.

Acknowledgements

I would like to express my deepest gratitude to my supervisor, Dr. Zoey Zhou of the Department of Electrical & Electronics Engineering at AUT, for their invaluable guidance, patients and support throughout this research. Their insightful feedback and exacting standards challenged me to elevate the quality of my work and helped develop true confidence as an independent researcher.

I would also like to thank my postgraduate student mentor Rasool Peykarporsan for their invaluable guidance throughout this research. Whether troubleshooting experimental setbacks or helping make sense of complex data, their support and technical expertise were indispensable to the completion of this work.

I am also deep grateful to the dedicated staff of the AUT library for providing an exceptional research environment and access to critical resources be it available in country or elsewhere in the world. Their prompt assistance in sourcing references and navigating databases was invaluable to this research.

Auckland, New Zealand
July 2026
V.N.

Table of Contents

Abstract **2**

Attestation of Authorship **3**

Dedication **4**

Acknowledgements **5**

Table of Figures **9**

List of Tables **11**

Acronyms **12**

1 Introduction **13**

1.1 The Renewable Energy Shift 13

1.2 Technical Challenges 14

1.3 Research Aim and Objectives 16

1.4 Thesis Structure 17

2 Literature Review **19**

2.1 Power System Transition 19

2.2 GFL IBR Limitations 20

2.3 Ancillary Services Problem 23

2.3.1 Frequency Regulation *23*

2.3.2 Voltage Regulation *24*

2.3.3 Inertia *25*

2.3.4 Black Start *26*

2.4 GFM Control Architectures 27

2.4.1 Droop Control *27*

2.4.2 Key Strengths of Droop Control *29*

2.4.3 Primary Limitations of Droop Control *30*

2.4.4 Virtual Synchronous Generator *31*

2.4.5 Key Strengths of VSG *32*

2.4.6 Primary Limitations of VSG *33*

2.4.7 Other GFM Architectures *34*

2.5 Power Sharing and Coordination 35

2.5.1 Justification of Scope Boundaries *35*

2.5.2 Stability Analysis or Droop Control *36*
2.5.3 Grid Integration Constraints *39*
2.6 Research Gaps, Synthesis and Thesis Position 42
3 GFM IBR Design 44
3.1 Mathematical Modelling of Critical Signals 45
3.2 System Design Components 51
3.2 DC Source 53
3.3 Three Phase Inverter 61
3.4 LCL Filter 65
4 Droop Controller Design 71
4.1 Droop Control Architecture 71
4.2 Power Calculation 72
4.3 Frequency and Voltage Droop 73
4.4 Reference Signal Generation 76
4.5 Outer Voltage Control Loop 77
4.6 Inner Current Control Loop 78
4.7 IGBT Gate Driver 79
4.8 Grid Forming Inverter Base Resource 80
5 Grid Integration of GFM IBR 81
5.1 SMIB Connected System 81
5.2 Radial Distribution Network Connection 82
5.3 Autonomous Power Sharing 84
5.4 Methodological Summary 86
6 Simulation Results and HIL Validation 87
6.1 HIL Configuration 87
6.2 Peer Reviewed Publication 89
6.3 Islanded Mode – HIL Validation 90
6.3.1 Primary Droop Response – Island Mode *90*
6.3.2 Steady State Response – Island Mode *92*
6.3.3 Transient State Response – Island Mode *93*
6.4 Grid Connected Mode – HIL Validation 94
6.4.1 Primary Droop Response – Grid Mode *94*

6.4.2 Steady State Response – Grid Mode *97*
6.4.3 Transient State Response – Grid Mode *98*
6.5 LVRT Compliance – HIL Validation 99
6.6 Harmonic Compliance – HIL Validation 100
6.7 Simulation Results of IEEE 33 Bus System 103
6.7.1 IEEE 33 Bus System Baseline *103*
6.7.2 Single IBR on Bus 18 ..... *104*
6.7.3 Twin IBR on Bus 18 ..... *104*
6.7.4 Grid Integration of Multiple GFM IBR Configuration *105*
6.8 Summary of Results 106
7 Discussion and Critical Analysis 107
7.1 Model Simplifications and Environmental Assumptions 107
7.1.1 DC Source Assumptions *107*
7.1.2 IGBT Dead Time Compensation *108*
7.1.2 Hardware and Software Simplifications *108*
7.2 Physical and Operational Limitations 109
7.2.1 Hunting Oscillations *109*
7.2.2 Grid Synchronization *111*
7.3 Critical Analysis 112
8 Conclusions and Future Research 114
8.1 Fulfilment of Research Objectives 114
8.2 Synthesis of Empirical Contributions 115
8.3 Industrial and Regulatory Significance 115
8.4 Recommendations for Future Research 116
References 117

Table of Figures

Figure	Caption	Page
Fig 2.1	Architecture of Conventional Droop Controller	36
Fig 2.2	Illustrates Eigen Value Interpretation	37
Fig 2.3	A Typical Centralized Grid Architecture	40
Fig 2.4	A Typical Radial Distribution Network	40
Fig 2.5	The IEEE 33 Bus System	41
Fig 3.1	The Signal Processing Model	44
Fig 3.2	Architecture of Conventional Droop Controller	52
Fig 3.3	Block Diagram of DC System	53
Fig 3.4	The Power Curves of the PV Array	54
Fig 3.5	Boost Converter Schematic	55
Fig 3.6	P&O Algorithm for MPPT	56
Fig 3.7	Bi-directional DC-DC Converter	57
Fig 3.8	Operation of Simplified BESS	58
Fig 3.9	Dual Boost Converter Topology	59
Fig 3.10	DC Bus Measurements	60
Fig 3.11	Three Phase Inverter Topology	61
Fig 3.12	SPWM Signal Generation	62
Fig 3.13	IGBT Gate Driver Circuit	62
Fig 3.14	Harmonics in Inverter Output	63
Fig 3.15	LCL Filter Configuration	66
Fig 3.16	Voltage THD of Final GFM Inverter Design	68
Fig 3.17	Low Current THD of Final GFM Inverter Design	69
Fig 3.18	High Current THD of Final GFM Inverter Design	70
Fig 4.1	Droop Controller Architecture	71
Fig 4.2	Power Calculation Block of Droop Controller	72
Fig 4.3	Frequency and Voltage Droop Calculations	73
Fig 4.4	Active Power Eigen Value Trajectory	74
Fig 4.5	Reactive Power Eigen Value Trajectory	74
Fig 4.6	Internal Reference Signal Generation	76
Fig 4.7	Outer Voltage Control Loop	77
Fig 4.8	Inner Current Control Loop	78
Fig 4.9	Current Control – SPWM Interface	79
Fig 4.10	Implemented Droop Control IBR Design	80
Fig 5.1	Microgrid Topology	81
Fig 5.2	IEEE 33 Bus System – Radial Distribution	82
Fig 5.3	Multi-IBR Connection on Radial Network	83
Fig 5.4	IEEE 33 Bus – Single IBR Single Bus Connection	84
Fig 5.5	IEEE 33 Bus – Multiple IBR Single Bus Connection	85

Fig 5.6	IEEE 33 Bus – Multiple IBR Based DER	85
Fig 6.1	HIL Configuration	87
Fig 6.2	Real Time Telemetry Integration	88
Fig 6.3	HIL Setup of Real-time Validation	89
Fig 6.4	Primary Droop Response – Islanded System	90
Fig 6.5	Islanded Droop Response – Voltage and Current Envelope	91
Fig 6.6	Islanded Droop Response – Three Phase Signals	91
Fig 6.7	Steady-State Response of Islanded System	92
Fig 6.8	Transient Response in Islanded System	93
Fig 6.9	Grid Connected Droop Response	94
Fig 6.10	Grid Connected Droop Response – Voltage and Current Envelopes	95
Fig 6.11	Grid Connected Droop Response – Three Phase Signals	96
Fig 6.12	Steady-state Response in Grid-Connected System	97
Fig 6.13	Transient Response in Grid Connected System	98
Fig 6.14	LVRT Capability within the NZ Grid Code No Trip Envelope	99
Fig 6.15	Current Harmonic Analysis for Grid Connect Inverter	100
Fig 6.16	Harmonic Analysis for Grid Connect Inverter	101
Fig 6.17	IEEE 33 Bus System Baseline	103
Fig 6.18	Single GFM IBR on Bus 18	104
Fig 6.19	Twin GFM IBR on Bus 18	104
Fig 6.20	Multiple GFM IBR on IEEE 33 Bus System	105
Fig 7.1	DC Bus Induced Harmonics on Grid Current	107
Fig 7.2	Hunting Oscillations Debugging	110

List of Tables

Table 3.1: Datasheet with Boost Converter Data 55
Table 3.2: LCL Filter Parameters 67
Table 4.1: Droop Gain Coefficients 76
Table 4.2: PI Controller Tuned Parameters 79
Table 6.1 Table of IEEE 519 Harmonics Compliance of GFM Inverter 102

Acronyms

Acronym	Meaning
AC	Alternating Current
BESS	Battery Energy Storage
DC	Direct Current
DER	Distributed Energy Resource
DQ	Direct Quadrature
FACTS	Flexible AC Transmission System
GFL	Grid Following
GFM	Grid Forming
HIL	Hardware-in-the-loop
IBR	Inverter Based Resource
LVRT	Low Voltage Ride Through
MPPT	Maximum Power Point Tracking
P&O Algorithm	Perturb and Observe Algorithm
PCC	Point of Common Connection
PID	Proportional Integral Differential
PV	Photovoltaic
RoCoF	Rate of Change of Frequency
PWM	Pulse Width Modulation
RES	Renewable Energy Sources
SMIB	Single Machine Infinite Bus
SPWM	Sinusoidal Pulse Width Modulation
STATCOM	Static Synchronous Compensator
THD	Total Harmonic Distortion
VSG	Virtual Synchronous Generator

1 Introduction

1.1 The Renewable Energy Shift

The growing demand for energy and the need to meet international carbon emissions targets have led to the widespread adoption of renewable energy sources (RES) into electrical grids. This has accelerated the deployment of inverter-based resources (IBR) such as solar photovoltaic (PV) and wind in conjunction with battery energy storage systems (BESS) [1]. This transition has fundamentally altered the topology of modern power systems, shifting from predominantly centralized generation toward highly distributed architecture composed of numerous small-scale units, including rooftop solar and commercial PV installations. While this paradigm shift supports decarbonization, it also introduces significant challenges to system stability and grid connection [2].

Over the past century, alternating current power systems were governed by a simple physically rotating mechanisms. Synchronous machines like turbines spinning at precisely regulated speeds and as such formed the backbone of grid stability. Their rotating inertia acted as a natural buffer, absorbing sudden mismatches between supply and demand and sustaining grid frequency through transient disturbances [3]. The stability of a power system, at its core, was a consequence of synchronized kinetic energy stored in millions of tonnes of spinning steel. These power systems can utilize renewable sources where geographically possible with the use of hydroelectric or geothermal power generation. However, they are largely fossil fuel based where coal or diesel fuels created the saturated steam required to spin these large synchronous machines.

In order to navigate the geopolitical state of affairs with regards to the availability and consequently the price of fossil fuels and addressing the global climate change concerns with more advent and extreme weather events becoming more frequent. Countries around the world are committing to carbon emissions targets with the goal of reducing carbon emissions for a more sustainable net zero future. Huge investments have been made toward this commitment according to the International Energy Agency IEA and Word Economic Forum report that in 2025 the total Energy Investments are set to rise to $3.3 trillion dollars USD of which around $2.2 trillion USD are for projects in renewable energy sources [1]. Photovoltaic technologies alone are set to increase to $450 USD billion in 2025 alone. This presents unique opportunities for researchers and industries alike to benefit from such investments as we collectively chart a course of a sustainable future [1].

1.2 Technical Challenges

In order to address these challenges modern DC based RES were introduced into the power grid and in order to effectively interface with the existing grid, electronic converters are used to convert the DC source to a grid compatible AC signal. This introduced grid following inverters (GFL) which has been the dominant paradigm over the last two decades. The GFL IBR represents a transitional technology that relied on the power grid for regulation and stability, they were frequently matched using phase locked loop (PLL) to a stiff voltage reference maintained by the grid itself and functioned as a current source injecting power on to the grid. They contribute no inertia, they cannot operate in islanded conditions, and under weak-grid scenarios that are defined by high impedance, low short-circuit ratio, or declining synchronous generation share. In such conditions their PLL dynamics become destabilizing rather than stabilizing and as a consequence GFL sources are designed to trip under fault conditions and wait for the wider grid to stabilize before it can be connected to the grid again. This makes GFLs untenable solution to meet 100% renewable energy targets mandated by countries like New Zealand and Australia.

This highlights the need for ancillary services which are a are a collection of core services that are geared at supporting the reliable and stable operation of the electrical power grid. There are four broad categories of ancillary services:

- Frequency Regulation
- Voltage Regulation
- Operational Reserves
- Black Start Capability

As the grid loses fossil fuel based synchronous generation, it loses with it critical inertia that allows the grid to resist rapid changes in frequency required for grid stability. Synchronous machines also act as a controllable voltage source behind and impedance and regulates voltage through an instantaneous physical response driven by flux conservation, and a continuous active response driven by the excitation system. In this way the synchronous machine governs the frequency by balancing active power and governs voltage by balancing reactive power. Operating reserves are typically achieved by maintaining spinning reserves that are synchronized with the grid but producing a fraction of their full capacity that can rapidly be brought rated power output to meet unexpected demand or react to unexpected loss of generation. Large conventional generation sources can also have the ability to Black Start, which is the capability to self-start the grid without any external excitation power from the grid.

Most small-scale distributed energy resources (DERs) employ grid-following control due to their limited capacity. Consequently, they are unable to provide essential ancillary services, such as frequency and voltage regulation, and lack fault tolerance mechanisms including low-voltage ride-through (LVRT) capability [2]. Historically, these functions were

supplied by large synchronous generators; however, as fossil-fuel plants are retired and renewable penetration increases, DERs now account for a substantial portion of total generation. This shift has driven the development of advanced interconnection standards, such as IEEE 1547-2018, which introduce stricter requirements for voltage support, frequency response, and fault-ride-through capability [4]. Countries such as Australia and New Zealand are actively incorporating these requirements into their regulatory frameworks. These characteristics affect the stable operation of the electrical grid and presents the core challenge with the integration of renewable energy sources to provide both sustained and sustainable energy

To address stability concerns the grid-forming (GFM) inverters have emerged as a key technology for improving stability in IBR-dominated networks, as they can autonomously establish voltage and frequency references and provide synthetic inertia [5]. At utility scale, GFM inverters are often deployed alongside flexible AC transmission system (FACTS) devices, such as static synchronous compensators (STATCOMs), to achieve dynamic voltage regulation and enhance system stability during disturbances [6]. However, the high capital cost and MVAR-scale operating range of FACTS devices make them impractical for microgrids and small-scale DERs, while research into low-capacity static synchronous compensator (STATCOM) alternatives remains ongoing [7].

A summary analysis of market trends and investments in renewable energy suggests that IBRs are broadly categorized in one of two sets [8]. Expensive large-scale plants that use grid forming inverters in conjunction with FACTS devices to achieve regulation, stability and fault tolerance. The cheaper small-scale plants that use grid following inverters to provide power but rely on the grid for regulation and stability and offer minimal fault tolerance characteristics. The proliferation of solar on the grid, has in recent years led to stability issues that have resulted in massive power outages incurring both equipment and economic damage. In Australia the energy regulatory body has sought legal action against suppliers for failing to meet LVRT compliance during the 2016 South Australian System Blackout [9]. Subsequent analysis reports have indicated that the proliferation of low-cost rooftop solar without incorporating sufficient ancillary services poses a major risk to the grid akin to the 2016 South Australian blackout event [10]. The goal of this research is to bridge this gap by addressing core issues around regulation, stability and fault tolerance by implementing and validating the design of a small utility scale smart inverter that has grid forming capabilities.

A preliminary overview of the current GFM IBR literature bifurcates into two broad streams. The first is the comparative and conceptual stream comprising of papers that argue for GFM over GFL, survey control architectures, analyse stability properties theoretically, or benchmark one control method against another. The second is the component depth stream in which papers that go deep on a single technical problem such as current limiting during faults, LCL filter resonance damping, small-signal stability of a specific control topology, or digital control topologies. Both streams produce

valuable knowledge but neither answers the fundamental questions a practising engineer or a commercial developer actually faces, which are how does one to deploy a GFM IBR at utility scale starting from real hardware and what does the complete design look like and how well does it eventually function. The literature has extensively proven the former and largely assumed the efficacy of the latter in idealized simulations at the component level with high-fidelity simulations scoped for future research. This thesis aims to addresses the latter directly moving beyond comparative analysis toward a validated end-to-end design at commercial utility scale with the goal of making grid participation more accessible for small scale DERs and not intended as a replacement for GFL IBRs or FACTS devices. This reflects the future of the grid that is a hybrid solution incorporating all these technologies working together to achieve 100% renewable energy targets.

1.3 Research Aim and Objectives

The aim of this research is the integration of a GFM IBR into a grid with the end-to-end implementation of a utility scale solar PV based energy source. This is achieved with the component level implementation of a PV array interfaced with a maximum power point tracking algorithm-controlled boost converter to from a DC source that interfaces with an IGBT based three-phase inverter that is controlled by a multi-loop droop controller that interfaces with an LCL filter to interface with an infinite bus. The objective is to investigate islanded, and grid connected operational modes for transient and steady state stability.

The key objectives of this thesis are as follows:

1. Development of a droop-controlled GFM PV inverter capable of autonomously regulating frequency and voltage in both islanded and grid-connected operation.
2. Hardware-in-the-loop (HIL) validation of transient and steady state stability with the demonstration of operation within New Zealand grid code specified stable operational limits for frequency and voltage and harmonics.
3. Verification of New Zealand grid compliant low voltage ride through (LVRT) achieved with recovery from three-phase short circuit fault without loadshedding or reliance on FACTS devices.
4. Demonstrate autonomous communication less power sharing with multiple GFM inverters integrated with a radial distribution network and the voltage profile improvement associated with power injection on the tail ends of radial networks.

1.4 Thesis Structure

This thesis is structured into eight chapters systematically scaling the investigation from discrete power electronic component physics up to macroscale utility grid dynamics:

Chapter 2: Literature Review

This chapter reviews the literature to explore the limitations of GFL technologies and the use of ancillary services to establish regulation. The chapter then establishes the mathematical frameworks governing grid-forming (GFM) control topologies. Finally, it critically evaluates current academic literature, explicitly identifying the research disconnect between localized power electronic models and macro-level grid integration studies, thereby defining the technical boundary conditions for this work.

Chapter 3: GFM IBR Design

Component level design and baseline validation establishes the core system utilized in this research. Details the end-to-end mathematical modelling and design of the 100kW hybrid PV-BESS IBR asset. It walks through the discrete IGBT switching parameters, Sinusoidal Pulse-Width Modulation (SPWM) schemes, and the tuning of the LCL filter stage to satisfy strict total harmonic distortion (THD) constraints. This establishes a high-fidelity physical baseline for subsequent controller and network designs.

Chapter 4: Droop Controller Design

Develops the control intelligence layer for the modelled plant. It first establishes an industry-standard baseline by designing and validating an active grid-forming (GFM) droop control framework, defining the internal voltage, current, and outer power loops required for autonomous voltage and frequency regulation.

Chapter 5: Grid Integration of GFM IBR

Establishes the multi-tiered grid testing environments used to validate the dual-loop control topologies. This chapter details the design of a localized microgrid to evaluate autonomous frequency and voltage regulation across both islanded and grid-connected configurations. It further establishes a worst-case 140ms symmetrical short-circuit fault scenario to analyse transient resilience and models the macroscale IEEE 33-bus radial distribution network to evaluate the improved voltage stability margin at the weak busses with the integration of the implemented GFM IBR at weak terminal nodes.

Chapter 6: Simulation Results and HIL Validation

Executes the simulation frameworks designed in Chapter 5 and provides the core empirical findings of this thesis. It analyses the dynamic real and reactive power waveforms, the voltage and frequency waveforms and the LVRT compliance. The results that have been validated via peer-reviewed publication in an ACPEE 2026 IEEE-associated conference. Additionally, it presents the multi-unit network profiles and the

macroscale IEEE 33-bus terminal voltage distributions, establishing a verified, data-driven foundation for subsequent critical analysis.

Chapter 7: Discussion and Critical Analysis

This chapter systematically interrogates the empirical findings of Chapter 6 against potential technical challenges and industry counter arguments. It critically analyses core design assumptions, model simplifications, outlines the operational boundaries and inherent limitations of the implemented system, in order to establish a framework for improvements to this research.

Chapter 8: Conclusions and Future Research

This chapter summarizes the fulfilment of research objectives and the empirical contributions and its industrial significance along with recommendations for future research in this domain.

2 Literature Review

2.1 Power System Transition

The current climate policies around the globe and the mandated decarbonisation targets have established the need for renewable sources of energy for electricity generation. This has directly led to the simultaneous phasing out of fossil fuels based synchronous machines and the introduction of power electronic converter-based generation. The high penetration of IBR as a result of residential and commercial rooftop solar and installation of larger scale renewable generation plants like wind and solar when coupled with decommissioning of coal fire power plant and diesel electric generators create the unique set of circumstances that represent the current transition phase of power grid around the world.

Global electricity generation is undergoing a structural transition of unprecedented scale and speed. Installed renewable energy capacity reached approximately 4442 GW globally by 2024, with solar PV and wind together accounting for over 96.6% of net generation capacity additions in that year [11]. In parallel, coal-fired generation capacity retirements are accelerating across major electricity markets, with over 280 GW of coal capacity retired globally between 2016 and 2023 [12]. In New Zealand, the government's target of 100% renewable electricity generation by 2030 is driving simultaneous investment in utility-scale wind and solar and the progressive phase out of fossil fuel-based plants like Huntly station in Waikato region [13].

This transition is not simply a change in fuel source, rather it represents a fundamental change in the physical character of power generation. Synchronous generators, which have formed the basis of alternating current power systems since the late nineteenth century, provide three critical grid support properties passively through their rotating electromagnetic structure. First, the kinetic energy stored in their rotating mass provides inertial resistance to frequency deviations, a property quantified through the swing equation and expressed as the inertia constant. Second, their direct electromagnetic coupling to the grid voltage provides inherent voltage stiffness, maintaining bus voltage against disturbances through the excitation system and synchronous reactance. Third, their low internal impedance allows them to contribute fault current several times their rated value, enabling protection relays to detect and clear faults rapidly. Inverter-based resources operating in conventional grid-following mode provide none of these properties inherently. They operate as controlled current sources that require a measurable grid voltage for phase-locked loop synchronisation, contribute fault current due to semiconductor device constraints, and have no rotating mass and therefore no natural inertial response.

The practical consequences of this transition are already observable in operating power systems. The September 2016 South Australia black system event demonstrated how high IBR penetration combined with low system strength can produce cascading protection system failures that a synchronous-machine-dominated system would have resisted [10]. The August 2019 Great Britain frequency event, triggered by a lightning strike that disconnected both a gas turbine and an offshore wind farm simultaneously, showed frequency declining at a rate of 0.125 Hz per second which was significantly faster than historical norms, reflecting the reduced inertia of the modern UK grid [14]. The North American Electric Reliability Corporation (NERC) technical reports on bulk power system reliability have consistently identified low short circuit ratio conditions at IBR connection points as an emerging reliability risk as synchronous capacity retires [15]. In New Zealand, Transpower has documented declining system inertia on the South Island as hydro generation increasingly operates at reduced output during periods of high renewable generation from wind [16].

While the inertia and system strength debate has predominantly focused on transmission-level dynamics, the transition presents an equally significant challenge at distribution network level which is the context directly relevant to this thesis. Traditional radial distribution networks were designed for unidirectional power flow from substation to load, with voltage regulation achieved through transformer tap changers and the assumption of a stiff voltage source at the feeder head. The proliferation of distributed IBR with the wide adoption residential and commercial rooftop solar, small wind installations, and utility-scale distributed generation from the 100kW to low-megawatt range, introduces bidirectional power flows, weakens the feeder head voltage reference that GFL IBRs depend on for synchronisation, and creates voltage profile conditions along radial feeders that conventional regulation strategies cannot adequately manage [17]. The voltage profile on radial distribution networks with and without high IBR penetration as investigated in the IEEE 33-bus studies presented in Chapter 5 of this thesis is a direct consequence of this distribution-level manifestation of the broader transition. However, in order for IBR to meaningfully contribute to stability and power quality they need to be sufficiently fault tolerant to remain connected to the grid during grid disturbances.

2.2 GFL IBR Limitations

The major limitation of grid following inverter base resources is that since they rely on the grid for reference and stability any disturbances in the grid typically leads to GFL IBRs tripping off in order to not contribute to the instability of grid and requires that the grid is stabilized before reconnecting to provide power. Motivated by the integration of IBR into the electric grid discussed in the previous section it is easy to see that an electric grid dominated by GFL IBRs quickly lose stability leading to the rapid collapse of the entire

grid or large sections of the power grid as evidenced by the major black out events discussed.

A GFL IBR operates as a controlled current source. It measures the grid voltage at its point of common coupling, uses a phase-locked loop (PLL) to extract the voltage angle and frequency, and injects a current that is controlled to deliver a specified real and reactive power based on that measured angle. The PLL is the synchronisation mechanism, it continuously tracks the grid voltage angle and provides the reference frame for the current controller [18] [19]. The inner current control loop, typically implemented in the synchronous DQ reference frame, regulates the injected current to follow the reference set by the outer power control loop.

This architecture is effective in strong grids where the voltage at the point of common connection (PCC) is stiff, meaning it is dominated by the upstream synchronous generation and network and is not materially affected by the IBR's own current injection. In those conditions the PLL tracks a stable, well-defined voltage angle and the current controller delivers accurate power tracking with fast dynamic response [20]. The architecture is adequately mature, well understood, and is the basis for the vast majority of commercially deployed grid feeding inverter systems today.

A grid-connected inverter must inject current that is synchronised with the grid voltage, meaning the injected current must have the correct phase angle relative to the voltage at the PCC in order to deliver real and reactive power at the specified amounts. If the current is in phase with the voltage, the inverter delivers real power. If it leads or lags by ninety degrees, it delivers reactive power. Given any arbitrary power setpoint the inverter needs to know the instantaneous angle of the grid voltage at every moment in order to compute the correct current reference which is provided by the PLL angle measurement.

It is a feedback control system that continuously estimates the grid voltage angle by operating in a rotating reference frame i.e. the synchronous DQ frame and driving the measured Q-axis voltage component to zero. When the q-axis voltage is zero the d-axis voltage equals the full voltage magnitude and the reference frame angle matches the grid voltage angle exactly [18] [19] [20]. The PLL output is this angle estimate, which the current controller uses as its reference frame for all subsequent calculations.

This is an elegant and practical solution in the context for which it was designed such as a grid connected inverter connected to a strong, stiff grid dominated by large synchronous machines. In that context the grid voltage angle is externally determined, stable, and largely unaffected by anything the inverter does [21]. The PLL is simply a measurement device extracting a well-defined signal.

The assumption that the grid voltage angle is externally determined and unaffected by the inverter begins to break down when the IBR are connected to weak grids with impedance between the source and load on the network.

The PLL assumption can be stated precisely as the voltage at the point of common coupling is determined entirely by the upstream grid, and the inverter's current injection has negligible effect on that voltage. This assumption holds when the grid is strong relative to the inverter. When the short circuit capacity of the grid at the connection point is large compared to the rated power of the inverter, expressed as a high short circuit ratio (SCR).

The **SCR** is a power system metric used to measure grid strength, expressed as a ratio of apparent power delivered to short circuit node on the grid to the grid's rated real power. A **Strong Grid** has a high SCR relative to the connected generation capacity and functions like a rigid infinite bus with low source impedance. It has the ability to maintain stable voltages and absorb power fluctuations without significant spikes or drops [21]. A grid with SCR of 3.0 or greater is generally considered strong as per IEEE Standard 2800 -2022. A **Weak Grid** has a low SCR relative to the connected generation capacity. It has a high source impedance, and it is sensitive to power fluctuations leading to significant spikes and drops [21] [22]. A grid with SCR of less than 3.0 generally considered a weak grid.

When the SCR is high the grid impedance between the inverter and the nearest synchronous voltage source is low. A current injection by the inverter produces only a small voltage drop across that impedance and therefore causes only a small perturbation to the PCC voltage [22]. The PLL sees a voltage that is overwhelmingly determined by the upstream grid, and its measurement is accurate and stable.

The SCR decreases as synchronous machines retire and the grid impedance at the connection point increases and the inverter's current injection produces a progressively larger voltage at the PCC. At low SCR the PCC voltage is a significant function of the inverter's own current injection [23]. The inverter is no longer measuring an externally determined signal as it is partially measuring the consequence of its own output.

This creates a feedback loop within the PLL that does not exist in the strong grid case. The inverter injects a current based on the angle estimated by the PLL. That current injection perturbs the PCC voltage angle. The PLL measures the perturbed angle and updates its estimate. The updated estimate changes the current injection. The changed current injection further perturbs the voltage. Whether this feedback loop is stable, oscillatory, or divergent depends on the relationship between the PLL bandwidth, the grid impedance magnitude and angle, and the inverter's power output level.

In a strong grid this negative admittance contribution is small relative to the grid's positive admittance and the net system is stable. As fossil fuel based synchronous machines are retired the grid impedance increases and the grid's positive admittance decreases, the grid effectively weakens. In weak grids replacing lost generation capacity with GFL IBRs will cause the negative admittance contribution of the PLL to eventually dominate and destabilize the whole network. The instability manifests as growing oscillations in the

inverter current and the PCC voltage, typically in the sub-synchronous or low-frequency range of a few hertz to a few tens of hertz depending on the PLL bandwidth and grid parameters [23]. The short circuit ratio at a bus is defined as the short circuit capacity at that bus divided by the rated power of the IBR connected at that node. The short circuit capacity is inversely proportional to the Thevenin equivalent impedance so as the Thevenin impedance increases as fossil fuel based synchronous machine are decommissioned, the short circuit capacity decreases and the SCR decrease proportionally. This means that in a weak grid with high penetration of GFL IBRs will have a very low SCR that is highly susceptible to the collapse of the grid even under minor disturbances on that grid. A grid with high penetration of GFL IBRs is architecturally self-undermining as each additional GFL installation reduces the SCR that all existing GFL installations depend on for stable operation. This will create a compounding vulnerability for voltage collapse that cannot be resolved through incremental improvements to GFL control and that demands a fundamentally different converter architecture capable of providing ancillary services like frequency and voltage regulation without which external means of ancillary services will become a necessity for a grid dominated by inverter-based resources.

2.3 Ancillary Services Problem

Ancillary services are grid support functions that system operators procure separately from energy to maintain system security. In the context of high IBR penetration, the relevant ancillary services are those that compensate for the loss of synchronous machine properties. These include frequency regulation, inertial response, voltage regulation, reactive power provision, system strength, and black start capability [24].

2.3.1 Frequency Regulation

Frequency Regulation requires inertia to limit the rate of change of frequency immediately following a disturbance, fast primary response to arrest the frequency nadir and prevent collapse. Frequency nadir is the lowest point that system frequency reaches following a sudden generation-load imbalance before primary frequency response arrests the decline and frequency begins to recover. It is the most critical metric in frequency stability assessment because it defines the worst-case frequency excursion the system experiences and determines whether under-frequency load shedding or generator protection trips are activated.

Secondary frequency regulation restores system frequency to its nominal value following a disturbance by centrally coordinating the output of multiple generators through automatic generation control AGC. The AGC continuously monitors the area control error, which is a signal that combines the frequency deviation from nominal and the deviation of actual power interchange from scheduled interchange across

interconnection boundaries. The area control error is the fundamental input signal that tells AGC how much correction is needed and in which direction.

The primary and secondary responses operate on a progressively longer timescale and each being systematically degraded by the retirement of synchronous machines and their replacement with GFL IBRs. Traditionally these services were provided automatically and freely by synchronous machines as a byproduct of their physical operation. A synchronous machine connected to the grid provided inertia, reactive support, and fault current without any additional control action or market incentive. These were inherent properties of the rotating electromagnetic machine and as synchronous machines retire the system operator must procure these properties explicitly from alternative providers at market cost.

Fast frequency response services involve the procurement of generators and load that respond rapidly to frequency deviations. These are the most widely deployed ancillary service response to inertia loss. In Australia, the Australian Energy Markey Operator (AEMO) introduced a mandatory fast frequency response requirement following the South Australia 2016 event [9]. In the year 2020, the UK the National Energy System Operator (NESO) has introduced a dynamic containment service which require providers to respond within seconds to frequency deviations and are procured by competitive tender [25]. In New Zealand the grid code aims to maintain {-1.5% pu < 1.0 pu < +1.5% pu} as per schedule 8 of the country's grid and is discussed in greater detail in chapter 6.

Synthetic inertia services go further, requiring providers to respond within the first few hundred milliseconds of a frequency event. This is the period when natural inertia from synchronous machines would normally arrest the rate of change of frequency. Battery energy storage systems (BESS), demand response, and some wind turbines with modified control can provide synthetic inertia. However, the literature documents important limitations like synthetic inertia from GFL IBRs requires PLL-based frequency measurement which introduces detection latency, the energy available from DC link capacitors is limited in duration, and the response is not as smooth or as physically predictable as natural inertia from rotating mass [26].

2.3.2 Voltage Regulation

Voltage Regulation and reactive power control services maintain bus voltages within acceptable limits across the network by controlling the reactive power balance at each node. Unlike frequency which is a system-wide single value, voltage is a local quantity that varies at every bus and must be managed at multiple points simultaneously.

Synchronous machines regulated bus voltage through their excitation systems. The automatic voltage regulator controlled the field current in the rotor winding to adjust the machine's internal EMF and therefore its reactive power output. When the terminal voltage fell below the setpoint the AVR increased field current, increasing the internal

EMF, causing the machine to inject reactive power into the network and raise the voltage back toward the setpoint. When terminal voltage rose above the setpoint the AVR reduced field current, causing the machine to absorb reactive power and pull the voltage down.

This voltage regulation was continuous, fast, and local as each synchronous machine regulated its own terminal voltage independently without requiring communication with other machines or a central controller. The aggregate effect of multiple machines each regulating their own terminal voltage produced a well-supported voltage profile across the network. The machines also provided short-circuit reactive current during faults with their low synchronous reactance which allowed them to inject large reactive currents that supported voltage at nearby buses during voltage depressions, which is critical for fault ride-through and voltage recovery.

Static VAR compensators, STATCOMs, synchronous condensers, and capacitor banks can provide reactive power support that partially compensates for the loss of synchronous machine excitation systems. Synchronous condensers in particular have attracted renewed interest because they provide rotating inertia and fault current in addition to reactive power [27]. These can effectively restore some synchronous machine properties without the carbon emissions of a fossil fuel prime mover.

The limitation of these solutions is that they are point solutions which improve conditions at their connection bus and in their electrical vicinity but do not address the distributed nature of the problem. A radial distribution network with low SCR at multiple tail-end buses cannot be adequately strengthened by a single synchronous condenser at the substation. The reactive power it provides must travel through the full feeder impedance to reach the tail-end buses, producing voltage drops that partially offset the reactive support benefit. In New Zealand the grid code aims to maintain {0.95 pu < 1.0 pu < 1.2 pu} of grid voltage as per schedule 8 of the grid code and is discussed in greater detail in chapter 6.

2.3.3 Inertia

Inertia in power grids function as the inherent, instantaneous exchange of kinetic energy stored within rotating synchronous masses that fundamentally bounds the initial Rate of Change of Frequency (RoCoF) during power imbalances, thereby providing the vital temporal buffer necessary to preserve grid synchronism and safeguard the frequency nadir before active primary control mechanisms deploy. A network with high penetration of GFL IBR will reduce system inertia with the physical decoupling of the power system from its energy source and the displacement of legacy synchronous generation. A GFL inverter operates strictly as a grid-dependent current source and since it relies on PLL to track the voltage vector of the host grid, extracting the grid angle to inject its programmed active and reactive current in perfect phase alignment. When a frequency disturbance

occurs, the PLL acts as a tracking filter. It simply updates its internal mathematical angle to follow the new grid frequency. This means the inverter does do anything to resist this disturbance on the grid, rather it actively rides along with the disturbance. The Australian AEMO for example has introduce inertia requirements for IBR sources effective as of 2025 specifically designed to address these issues [28].

2.3.4 Black Start

Black Start refers to the ability to energise a power grid after a complete network wide loss of power i.e. a blackout event. The established GFL IBR limitation here as well are unable to start the grid following a blackout as they lack a voltage reference required to connect to the grid. The February 2021 blackout event in Texas, USA illustrated this condition where the Electric Reliability Council of Texas found in its investigation that the GFL IBR had limited serviceable and unable to perform black start due to the limitations discussed in this literature review [29]. A Black Start universally represents a system transition from 0.0 pu voltage and frequency to 1.0 pu baseline to set the grid reference for or synchronize to the wider grid.

A review of how ancillary service are applied for the current power system transition to a fully renewable sourced grid highlights the three major macroscopic challenges. Firstly, the cost and complexity of implementing external sources for regulation, inertial and black start capabilities. Secondly ancillary services address the observable symptoms of a grid with high penetration of GFL such as declining RoCoF performance, deep frequency nadirs, reduced system strength, and voltage profile degradation as discussed in this section, it does not address the root cause, which is the architectural incompatibility between current-source GFL converters and the weak-grid conditions that wide adoption and deployment of GFL IBRs itself creates. Lastly due to the cost and complexity most ancillary services are designed to be transmission connected resources to provide transmission level system security, the ability of transmission level solutions to be rolled out on the distribution level is limited. At the same time current trends for renewable energy integration into the power grid are largely represented by distributed energy resources (DER). The natural topological placement of DERs in power systems is represented by a large number of smaller utility scale inverter that connecting on radial distribution networks as opposed to fewer larger, gigawatt scale renewable generation units.

Ancillary services represent the current operational response to the grid support deficit created by high GFL IBR penetration. They are necessary in the near term and will remain part of the solution set. However, they are costly, address symptoms rather than causes, scale poorly with penetration, and cannot address the distributed nature of the problem on radial distribution networks. A different converter design is required to address the root cause directly by changing the converter's relationship to the grid from voltage-tracking current source to voltage-forming voltage source, providing inertia, system

strength contribution, and voltage regulation as inherent properties of the control architecture rather than as separately procured services.

2.4 GFM Control Architectures

Grid Forming Inverter Based Resources (GFM IBRs) represent a fundamental paradigm shift in power electronic control topologies, engineered specifically to mitigate the systemic regulation and low-inertia vulnerabilities outlined previously. The GFM architecture typically comprising a primary energy source coupled to a three-phase voltage source inverter (VSI) diverge entirely at the control layer when compared to GFL systems. Rather than acting as grid-dependent current sources, GFM IBRs are synthesized to function as autonomous voltage sources behind a virtual internal impedance. This architecture enables the independent generation and precise regulation of localized voltage magnitude and frequency without requiring a pre-existing grid reference. Consequently, GFM topologies inherently possess the capacity to provision critical ancillary services, including virtual inertia, dynamic operating reserves, and robust fault-ride-through (FRT) capabilities. Furthermore, when deployed within hybrid configurations alongside Battery Energy Storage Systems (BESS), GFM IBRs provide the requisite energetic and control baseline to execute autonomous black-start procedures, serving as a foundational asset for grid restoration. The cumulative effect of these technical attributes makes GFM IBR key pillars for resilient networks with high penetration renewable energy sources. In order to establish a rigorous theoretical baseline for the subsequent control design, this section delineates the mechanistic attributes and operational constraints of dominant GFM control paradigms, providing a systematic comparative analysis of their operational efficacies and systemic vulnerabilities under adverse grid conditions. Accordingly, this section outlines the operational constraints of two prominent control paradigms in development today. Together they represent the two architectures with the most direct analytical relationship to each other in the literature, rendering them uniquely suited for an equitable, structurally aligned comparative analysis.

2.4.1 Droop Control

The conventional Droop Control represents an architecture directly adapted from the governing systems of synchronous generators. The key strength of this method is that it is backed by mature analytical framework that has been rigorously tested to evaluate its performance and establish extensive field validation in parallel machine operations. However, a primary limitation of the conventional droop paradigm when applied to modern voltage source inverters is its inability to inherently provision virtual inertia. Since conventional droop mimics the steady state algebraic speed-droop characteristics of a physical governor, leaving behind the natural kinetic energy storage of a physical rotor mass, the control loop exhibits a purely static response unless explicitly augmented by power measurement filtering or virtual mass dynamics [30]. Historically, this lack of

synthetic inertial response was of minor consequence in legacy grids where large-scale rotating synchronous assets naturally guaranteed a robust system inertia baseline, a condition that no longer holds true in low inertia, inverter dominated distribution networks.

Droop control implements grid-forming behaviour by directly emulating the steady-state governor and automatic voltage regulator characteristics of parallel-connected synchronous generators. The frequency droop law relates the converter's output angular frequency $\omega$to its measured active power output P through (2.1):

$$\omega = \omega_0 - m_p(P - P_0) \tag{2.1}$$

where ω_0 and $P_0$are the nominal frequency and active power setpoint, and $m_p$is the frequency droop coefficient. Analogously, the voltage droop law relates the converter's output voltage magnitude $E$to its measured reactive power output Q through (2.2):

$$E = E_0 - m_q(Q - Q_0) \tag{2.2}$$

where $E_0$and $Q_0$are the nominal voltage magnitude and reactive power setpoint, and $m_q$is the voltage droop coefficient. Integrating the frequency obtained from the first relation yields the instantaneous phase angle $\theta$of the converter's internal voltage reference, while the second relation directly sets its magnitude, together defining the reference phasor $E\angle\theta$ [30] [31].

This reference is applied to a cascaded voltage and current control structure: an outer voltage loop regulates the filter capacitor voltage to track $E\angle\theta$, typically implemented in the synchronous dqreference frame using proportional-integral compensators, while an inner current loop regulates the filter inductor current to provide fast dynamic tracking of the voltage loop's output and to enforce current limiting during overcurrent conditions. The output of the inner loop generates the PWM modulating signals applied to the converter switches.

As each converter adjusts its frequency and voltage references autonomously based only on its own locally measured power output, droop control achieves decentralised power sharing among multiple parallel-connected converters without requiring inter-unit communication: converters operating with steeper droop slopes reduce their power output more for a given frequency or voltage deviation, and the resulting steady state operating point distributes load in inverse proportion to the droop coefficients, mirroring the proportional load-sharing behaviour of synchronous generators with governor droop [32]. The droop coefficients $m_p$and $m_q$are the primary design parameters, selected according to the converter's rated power and the maximum permissible frequency and voltage deviations specified by the applicable grid code, establishing a direct and traceable link between the control design and regulatory operating limits.

Unlike virtual synchronous generator implementations, conventional droop control as expressed above produces a static, algebraic relationship between power and frequency rather than a dynamic, second order one so the frequency reference responds instantaneously to the measured power signal without an explicit inertial term, with the converter's transient dynamics determined instead by the bandwidth of the cascaded voltage and current control loops [32]. The cascaded voltage and current control structure provides inherent current limiting capability. When the converter current exceeds the current limit the inner current loop saturates, limiting the current to the hardware rating while the outer voltage loop attempts to maintain voltage regulation. This behaviour of providing limited but controlled fault current rather than immediate disconnection during a fault event is more compatible with grid protection systems than GFL current source behaviour [33].

2.4.2 Key Strengths of Droop Control

While contemporary research frequently emphasizes its performance limits under non-ideal grid conditions, classical decoupled droop control $(P - \omega \ / \ Q - V)$ remains the benchmark primary control architecture for grid-forming (GFM) inverter-based resources (IBRs). Its sustained prominence in peer-reviewed literature and commercial deployments is underpinned by four fundamental technical merits:

1. Communication-Independent, Autonomous Power Sharing

The foremost advantage of conventional droop control is its completely decentralized execution. By utilizing localized voltage and current measurements to calculate instantaneous active and reactive power, the control loop adjusts the inverter's frequency and internal voltage magnitude references without requiring high-speed, low-latency inter-unit communication infrastructure. This communication-independent architecture eliminates a critical single point of failure, drastically increasing system reliability and instantiating true "plug-and-play" scalability for large-scale multi-inverter networks and parallel-redundant microgrids.

2. Analytical Maturity and Small-Signal Traceability

Unlike highly non-linear or heuristic control paradigms (e.g. model predictive control or machine-learning-driven variants), conventional droop boasts decades of analytical verification derived from classic power system governor dynamics. Its linear design permits the derivation of explicit, structurally sound small-signal state-space models. This mathematical tractability allows power systems engineers to apply standard eigenvalue analysis, root-locus techniques, and Lyapunov stability criteria to rigorously predict system behaviour, optimize control loops, and define guaranteed stability margins within standard industry simulation platforms (such as PSCAD, DIgSILENT Power Factory, and MATLAB/Simulink).

3. Low Computational Overhead and Parametric Parsimony

The mathematical formulation of conventional droop relies on simple, low-order algebraic expressions coupled with standard first-order low-pass filters. This structural simplicity avoids the need for heavy computational architectures, high-order matrix inversions, or complex online state estimators at the primary control layer. Consequently, the control law can be easily executed on standard industrial microcontrollers or digital signal processors (DSPs) at high sampling rates without causing timing overruns, freeing up computational headroom for inner loop protection algorithms, active damping, or secondary optimization layers.

4. Intrinsic Voltage-Source Behaviour and Weak Grid Support

By establishing a well-defined internal voltage vector behind a series impedance, conventional droop enforces an inherent voltage-source characteristic. Under sudden load changes or grid phase jumps, the inverter provides instantaneous active and reactive power balancing driven strictly by the natural electrical dynamics of the power network, before any active control loop even processes the disturbance. This natural power-angle defence mechanism enables the asset to provide robust voltage and frequency support in weak, low-inertia systems, enhance local power quality, and maintain self-sustained operation during black-start or islanded scenarios.

2.4.3 Primary Limitations of Droop Control

Despite these documented operational merits, conventional droop control exhibits inherent technical limitations that necessitate careful consideration. Classical decoupled droop control $(P-\omega\ /\ Q-V)$ exhibits critical structural and operational vulnerabilities when deployed in modern power systems. These limitations are primarily categorized into four systemic challenges:

1. Sensitivity to Network R/X Ratios and Control Cross-Coupling

The fundamental operational premise of conventional droop relies on a strictly inductive network interface $(X \gg R)$, which decouples active power sensitivities to the power angle and reactive power to voltage magnitude. However, in low-voltage distribution feeders, weak microgrids, or radial lines characterized by high R/Xratios, this decoupling assumption collapses. The resulting non-negligible line resistance introduces severe cross-coupling between the $(P-\omega)$ and $(Q-V)$ control loops. This coupling manifests as localized power hunting, sustained voltage oscillations, and a degraded transient response, frequently necessitating complex virtual impedance augmentations to artificially restore inductive characteristics.

2. The Inertia-Stability Margin Trade-Off

Since the classical droop equation is purely algebraic, an inherent virtual inertial response is only instantiated via the time constant $(\tau = 1/\omega_c)$ of the low-pass filters

(LPFs) embedded within the power measurement stage. Attempting to augment the system's virtual inertia constant (H_{eq}) requires either reducing the droop gain (R_p) or decreasing the filter cutoff frequency (ω_c). However, lowering ω_c introduces non-negligible phase lag into the primary frequency-tracking loop. In weak electrical grid configurations or low SCR conditions, this control latency drives low-frequency small-signal eigenvalues toward the right half-plane (RHP), inducing oscillatory instability and narrowing the system's overall robust stability margins.

3. Transient Instability Under Current-Limiting Constraints

Under severe symmetrical or asymmetrical grid faults, a grid-forming inverter operating under conventional droop behaves naturally as a stiff voltage source, inherently driving massive instantaneous overcurrent that threaten the physical thermal thresholds of the semiconductor switching valves (IGBTs/SiC). To prevent catastrophic hardware failure, current-limiting algorithms (such as virtual impedance scaling or hard current saturation) must rapidly override the voltage-source characteristic. This forced transition to a current-source topology alters the power transfer dynamics, causing the internal voltage angle reference calculated by the droop loop to rapidly drift away from the host grid vector, frequently resulting in transient instability, phase-tripping, or a failure to achieve post-fault ride-through synchronization.

4. Inherent Steady-State Regulation Deviations

By definition, conventional droop is a proportional control paradigm that relies on a structural steady-state error Δf and ΔV to autonomously command changes in active and reactive power injection. Consequently, under high penetration levels or severe load-generation imbalances, the collective droop action drives the system away from nominal frequency and voltage baselines. Correcting these systemic offsets requires the overlaying of secondary centralized or distributed control loops, which escalates communication dependencies, computation latencies, and overall power system control complexity.

2.4.4 Virtual Synchronous Generator

A virtual synchronous generator (VSG) is a control strategy that endows a grid-connected power converter with the dynamic electromechanical characteristics of a conventional synchronous generator. The core of the VSG control law is a digital implementation of the synchronous machine swing equation depicted by (2.3),

$$J\frac{d\omega}{dt} = \frac{P_m - P_e}{\omega} - D(\omega - \omega_0) \tag{2.3}$$

where J is a virtual moment of inertia, ω and ω_0 are the instantaneous and nominal angular frequencies, P_m is a virtual mechanical power input set by the active power reference, P_e is the measured electrical power output, and D is a virtual damping coefficient. Integrating

the resulting angular acceleration yields a virtual rotor angle θ, which defines the phase of the converter's internal voltage reference [34]. This embedded second-order dynamic produces an inertial response: following a step change in load or generation, the converter's frequency deviates gradually rather than instantaneously, with the rate of change of frequency inversely proportional to $J$and the post-disturbance damping governed by D.

A complementary virtual excitation loop emulates the automatic voltage regulator of a synchronous machine, adjusting the magnitude of the internal voltage reference Ein response to reactive power or terminal voltage deviations, typically through a proportional or proportional-integral law analogous to AVR droop [35]. The internal EMF $E\angle\theta$is then applied as the reference to an inner voltage and current control loop, which generates the PWM switching signals through the converter's LCL or LC output filter.

Since the VSG synchronises through the dynamics of the swing equation rather than through the PLL measurement of the grid voltage, it presents an internal voltage source behind a virtual synchronous reactance which is analogous to the transient reactance X'_d of a physical machine. This voltage source behaviour allows the converter to participate in power-angle synchronisation with the grid and with other VSG or synchronous units through natural power flow dynamics, to contribute fault current determined by its virtual impedance rather than by current limited PLL tracking, and to operate stably in islanded conditions without requiring an external frequency or voltage reference [36].

The principal design trade-off lies in the joint selection of $J$and D increasing J improves RoCoF limitation but reduces the damping ratio of the resulting swing-mode oscillation for a fixed D, requiring $D$to be co-tuned to maintain adequate transient damping. Unlike droop control, which produces a static power-frequency relationship, the VSG's swing dynamics introduce a genuinely dynamic response i.e. it has a second order response that more closely replicates the electromechanical behaviour of synchronous generation, at the cost of requiring a dispatchable energy source capable of sustaining the transient power exchange that inertial emulation demands.

2.4.5 Key Strengths of VSG

Mathematically emulating the classical swing equation of traditional rotating machinery, VSG control frameworks provide IBRs with an autonomous mechanism to inject true virtual inertia and dynamic damping into low-inertia networks and can be characterized by the following advantages:

1. Explicit, parameterizable inertial response without measurement latency.

The VSG's inertial response arises intrinsically from the embedded swing dynamics and acts from the instant a power imbalance is reflected in the measured electrical power

output. This avoids the PLL frequency-derivative estimation stage that introduces tens of milliseconds of detection latency in measurement based synthetic inertia approaches.

2. Physically interpretable, grid-code-compatible parameters.

The virtual inertia constant J and damping coefficient D have direct analogues to the inertia constant H and damping coefficient of a synchronous machine. This allows VSG controlled converters to be assigned inertial contributions that meet specific grid code requirements and to be represented in conventional power system dynamic studies using established synchronous machine modelling frameworks, without requiring new analytical methods.

3. PLL free synchronisation and weak grid robustness.

Synchronisation is achieved through the swing dynamics rather than voltage-angle tracking, eliminating the PLL and the weak-grid instability mechanisms associated with it. As the VSG presents an internal voltage source behind a virtual impedance, it does not require a pre-existing stiff voltage reference to establish its operating point, enabling stable operation across a wide range of short-circuit ratios, including islanded conditions where no external reference exists at all.

4. Protection compatible fault response with retained current limiting.

The converter's fault current contribution is determined by its internal EMF and virtual impedance rather than a hard current-source saturation limit, producing a fault response that more closely resembles, and is more readily coordinated with protection systems designed around synchronous machine fault characteristics, while the cascaded voltage and current control structure still permits current limiting for device protection.

5. Backward compatible power sharing with forward compatible dynamics.

The equivalence between VSG and droop-controlled steady-state characteristics means VSG control retains the decentralised power sharing properties of droop such that multiple units synchronise and share load proportionally, while adding a genuinely dynamic transient response that more closely replicates the electromechanical behaviour the grid was designed around, aligning with grid codes that increasingly specify inertia-based performance requirements explicitly.

2.4.6 Primary Limitations of VSG

1. Coupled inertia-damping parameter design with an inherent trade-off.

The virtual inertia constant J and damping coefficient D cannot be selected independently. Increasing J to improve RoCoF limitation reduces the damping ratio of the resulting swing-mode oscillation for a fixed D, requiring D to be co-tuned to maintain adequate transient damping. This joint design problem has no equivalent in droop control, which has no explicit inertia term to tune.

2. Dependence on a dispatchable energy source for credible inertial response.

The inertial response embedded in the swing equation corresponds to a real transient exchange of active power with the network. A synchronous machine sources this from rotor kinetic energy. A converter has only its DC link capacitor, whose stored energy is typically two to three orders of magnitude smaller than the kinetic energy equivalent implied by a representative inertia constant. A PV source operating at its maximum power point has no headroom to supply this transient demand and cannot absorb a transient surplus, creating a control conflict between the MPPT loop and the VSG inertia loop unless a bidirectional storage element is present on the DC bus.

3. Parameter sensitivity to network operating conditions.

The small-signal stability margins associated with a given J-D pair are not invariant as they depend on the grid impedance, the operating point, and the presence of other VSG or droop-controlled units on the same network. A parameter set that provides adequate damping under one network condition may produce poorly damped or oscillatory behaviour under a different short-circuit ratio or loading condition, requiring either conservative fixed parameters or adaptive retuning schemes.

4. Limited large signal stability guarantees.

VSG stability analysis is predominantly conducted through small signal linearisation around a defined operating point. Unlike matching control, which admits global Lyapunov-based stability guarantees through its port-Hamiltonian formulation, VSG control lacks comparable large signal stability results, leaving its behaviour under large disturbances less analytically characterised. System behaviour sudden faults, large load steps, or significant deviations from the linearisation point are not well understood.

5. Potential for oscillatory interaction in multi-converter systems.

When multiple VSG units operate on the same network, their coupled swing dynamics can produce inter-unit oscillation modes analogous to the inter-area and local oscillation modes of multi-machine synchronous systems. The damping of these modes depends on the combined J-D parameters of all participating units and the network impedance connecting them and ensuring adequate damping across all relevant modes in a multi-VSG system is a more complex design problem than in a single-unit analysis.

2.4.7 Other GFM Architectures

Beyond droop and VSG, the GFM landscape also includes matching control, dispatchable virtual oscillator control, and power synchronisation control, each offering distinct theoretical advantages. The matching control and dVOC provide stronger large-signal stability guarantees through port-Hamiltonian and nonlinear oscillator formulations respectively, while PSC was developed primarily for weak-grid HVDC connections [37] [38] [39]. These architectures are not treated in detailed comparison in

this review. Matching control's reliance on the DC link voltage as a direct synchronisation signal introduces an interface complexity with MPPT-controlled PV sources that exemplifies the integration questions this thesis is concerned with, dispatchable VOC's oscillator-based parameters lack the direct physical interpretability needed for grid code anchored design, and PSC addresses a transmission-connected context distinct from the distribution-scale application considered in this research.

2.5 Power Sharing and Coordination

The two main architectures examined in detail, droop control and the virtual synchronous generator converge to the same steady state power-frequency and voltage-reactive-power characteristics, differing principally in the presence of the swing equation's second-order inertial dynamics. The inertial capabilities present a significant advantage of VSG over droop control, but droop control has specific characteristics that outweigh the advantages of VSG and all other discussed control topologies in DER configurations.

The deployment of utility scale GFM IBRs on a distribution network that represents the current trend with the adoption of renewable sources would require additional communications layer for inter-inverter coordination of power sharing on the grid. Off all the GFM architectures reviewed in this research droop control poses a clear advantage over all of them with its inherent communication less power sharing and coordination based on droop characteristics. This represents the principal reason for selecting droop control over for end-to-end implementation the other discussed control topologies.

2.5.1 Justification of Scope Boundaries

In practice a hybrid solar PV plus BESS source with a well-designed BESS controller can remain fully compatible with the explicit and grid-code-parameterizable inertia emulation, which is the defining advantage of VSG architectures. The BESS provides exactly the dispatchable, bidirectional energy reservoir that credible inertial response requires but realising it would introduce a further coupling between the VSG's swing-driven transient power demands and the BESS converter's DC link voltage regulation loop, a co-design problem that sits beyond the integration boundary this thesis scope.

Droop control's static power-frequency and voltage-reactive-power laws, by contrast, couple directly and transparently to the cascaded voltage and current control structure without this additional interaction, its parameters translate directly from New Zealand grid code frequency and voltage deviation limits, its decentralised power-sharing properties suit the multi-IBR configuration. This ability for autonomous power sharing between multiple droop-controlled inverters without the need for any additional layer of communication for coordination. This makes it far more advantageous for multi-IBR network topologies that characterise the current trend with a multitude of vendor agnostic inverter designs being deployed at the smaller scale with the adoption of commercial roof top solar PV systems.

The droop control topology is therefore adopted as the grid-forming control architecture implemented and validated in this thesis, with the absence of explicit inertia emulation accepted as a deliberate scope boundary for a 100kW distribution-connected unit, and with the hybrid PV plus BESS architecture established here providing the foundation from which a VSG implementation and the DC-link co-design problem it would introduce represents a well-motivated direction for future work.

2.5.2 Stability Analysis or Droop Control

Given the selected GFM control architecture for this research is conventional droop control this section looks at droop specific converter level and network level stability characteristics including the analytical methods used to derive them. This will then be used as a framework to interpret the results of the end-to-end simulation of the conventional droop controller and the extent of its GFM capabilities and its small signal, transient and steady state stability when applied to a microgrid. The full details of the methods of implementation, the expected and achieved results, the limitations and the wider implications will be discussed in the later chapters accordingly.

The typical component level design of a conventional droop controller in the literature consists of a DC source that is connected to a three-phase inverter that feeds and LCL network that is connected to the power grid modelled via an infinite bus where a load can draw the required power. The standard topology of the conventional droop controller is shown in Fig. 2.1.

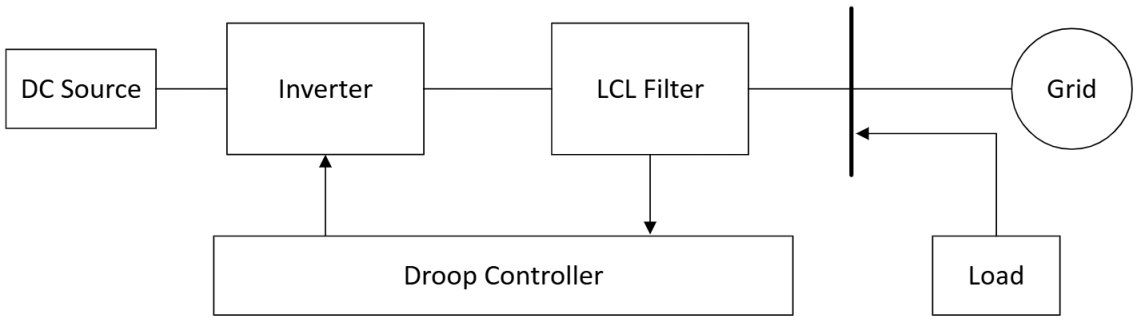


Fig. 2.1: Architecture of Conventional Droop Controller

The droop gains are applied to voltage and frequency in order to control the maximum allowable deviations in active power and reactive power. An inverter with zero droop control will supply the load with 1.0 per unit (pu) in terms of voltage and frequency.

Eigen Value Analysis

The converter level small signal stability and dynamic system response of droop control is determined by the eigen value analysis of the controller. Eigen values determine if and how fast a controller will be able to return the system to steady state. The real axis

determines the damping speed. A more negative real part means the system will return to steady state faster. The imaginary axis determines the frequency of oscillations and the dominant eigen values are closest to the imaginary axis and will dominate the systems transient behaviour to small signal disturbances [40]. The graphical illustration of how eigen values are interpreted can be seen in Fig. 2.2.

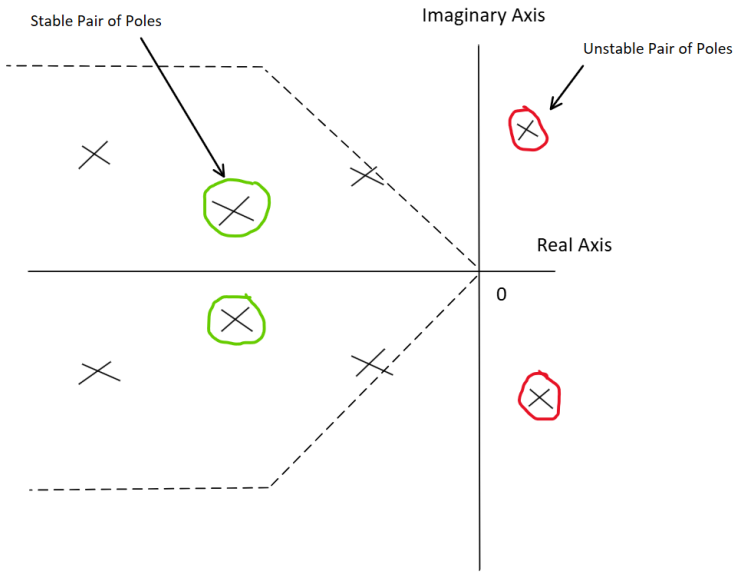


Fig. 2.2: Illustrates Eigen Value Interpretation

The droop gain parameters affect the eigen values in the following ways [40]:

Increasing frequency droop gain $m_p$typically pulls the low-frequency, active power-sharing eigenvalues further into the negative real-plane. However, excessively high active droop gain can cause the system to become poorly damped, leading to long, sustained active power oscillations.

Increasing voltage droop gain m_q generally shifts the reactive power-sharing eigenvalues leftward, improving stability but can pull down the voltage stability margin, leading to sluggish voltage recovery and potential instability at very high gains.

The droop controller's internal power calculation filter introduces eigenvalues directly related to its cutoff frequency. Slower filters have lower cutoff frequency and as such improve system robustness against high-frequency noise but can cause the multi-IBR power sharing modes to drift dangerously close to the imaginary axis causing instability.

Eigen Values are determined by the systematic linearization of the inherently no linear set of equations governing the system, these equations are as follows:

The Droop Equations for angular frequency (2.4) and voltage (2.5) depicted below:

$$\omega = \omega_0 - m_p P \tag{2.4}$$

$$V = V_0 - n_q Q \tag{2.5}$$

The Differential Equations of measurement via the LPF is depicted by (2.6) and (2.7):

$$\frac{dP}{dt} = -\omega_c P + \omega_c p \tag{2.6}$$

$$\frac{dQ}{dt} = -\omega_c Q + \omega_c q \tag{2.7}$$

The linearized operating point that gives the small signal perturbations (2.8) and (2.9):

$$\frac{d\Delta P}{dt} = -\omega_c \Delta P + \omega_c \left(\frac{\partial p}{\partial \delta}\Delta\delta + \frac{\partial p}{\partial V}\Delta V\right) \tag{2.8}$$

$$\frac{d\Delta Q}{dt} = -\omega_c \Delta Q + \omega_c \left(\frac{\partial q}{\partial \delta}\Delta\delta + \frac{\partial q}{\partial V}\Delta V\right) \tag{2.9}$$

Gathering your small-signal state variables into a vector, $\mathbf{x} = [\Delta\delta, \Delta P, \Delta Q]^T$ that yields the state space matrix depicted by (2.10):

$$\dot{\mathbf{x}} = A\mathbf{x}$$

$$\begin{bmatrix} \frac{d\Delta\delta}{dt} \\ \frac{d\Delta P}{dt} \\ \frac{d\Delta Q}{dt} \end{bmatrix} = \begin{bmatrix} 0 & -m_p & 0 \\ \omega_c \frac{\partial p}{\partial \delta} & -\omega_c & \omega_c \frac{\partial p}{\partial V} \\ \omega_c \frac{\partial q}{\partial \delta} & 0 & -\omega_c \end{bmatrix} \begin{bmatrix} \Delta\delta \\ \Delta P \\ \Delta Q \end{bmatrix} \tag{2.10}$$

Computing the determinant for the simplified 3x3 matrix, yield a third order polynomial. The coefficients of this polynomial are the algebraic combination of the droop gains and the system parameters. Solving this third order polynomial for λ yield three district eigen values depicted by (2.11) that dictate the system stability of the droop controller.

$$a_3\lambda^3 + a_2\lambda^2 + a_1\lambda + a_0 = 0 \tag{2.11}$$

This simplified 3x3 matrix shows the analytical derivations it misses to capture some of the critical nuances of a physical inverter. Using the simpler model relies on time-scale separation. The rapid electrical states such as those in the LCL filters and inner current loops settle down much faster than the slower power-sharing states. In mathematical analysis, this reduction is formalized via singular perturbation theory [41]. Although the simpler 3x3 matrix is useful to analytically derive symbolic closed from equations for eigen values, the practical inverter applications typically use a more complete 13x13 model or higher matrix to compute a more realistic set of eigen value that accurately models the inverter behaviour.

These eigen value are computed numerically with using MATLAB or other numerical solvers and is the approach that will be adopted for this research and detailed in the subsequent chapters. The eigen values can be evaluated for the following:

- Selection of Droop Gains
- Single Inverter Small Signal Stability
- Multi Inverter Small Signal Stability
- General Steady State Stability of the IBR in a Microgrid Network

Component Level stability of the IBR internal components relies on the parameter selection such as transistor switching, measurement sampling rates, resonant frequencies, damping methods and host of smaller design level constraints such as tuning of internal controllers and design topology that will be discussed in detail in the revenant chapters, eigen values represent the core method for determining the overall small signal stability of the designed system. This can be tested in a single machine connected to a variable load.

Network Level stability in a micro grid consists of the dynamic interactions of the IBRs, the physical distribution line parameters and the collective load on the system. The stability on a network determines whether multiple independent energy sources can maintain synchronism without large power swings or system wide voltage collapse. The ability for power sharing between multiple IBRs or power sharing with the wider grid in a grid connected topology determines stability at the network level. This consists of both single machine test setup and multi machine test setup that will be used to evaluate the network level stability in this research.

2.5.3 Grid Integration Constraints

The power grid can be abstracted as multi machine network consisting of generation sources connected via transmissions line impedances to collective load impedances. The generation source is modelled as either a voltage or current source behind and RL impedance connected to a lump summed model of a RLC impedance that represents the transmission lines that is connected to a collective RLC impedance that represents the load with power flowing from generation to via transmission lines for distribution. The traditional power grids with centralized generation architecture are still the most prevalent grid topology that exists today.

Although large Gigawatt scale renewable generations sources have been modelled to connect to the grid and supply the required power, this does not reflect the reality of the current trend with wide adoption of smaller distributed generation resource (DER). These sources will typically connect to a radial distribution network supplying power to its local micro grid that is connected to the wider grid, the surplus power is then supplied upstream to other nodes for distribution in the network such is the case for commercial rooftop solar generation and small-scale distributed renewable plants. This makes it

crucial for these DERs to be able to successfully regulate frequency, voltage and have fault tolerant characteristics such as LVRT that will be investigate in this research in the appropriate chapters. A typical centralized power network architecture can be seen in Fig. 2.3. The real challenge for integration of smaller utility scale DERs is to connect directly to the distribution network while maintaining a robust and stable power system.

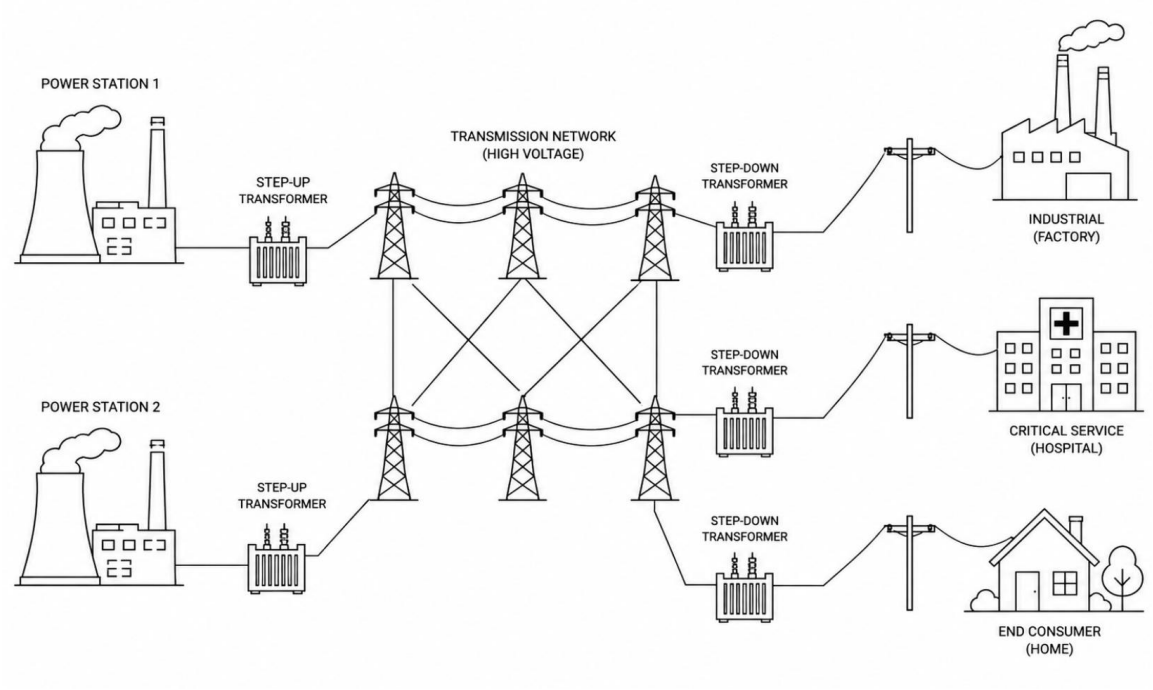


Fig. 2.3: A Typical Centralized Grid Architecture

This research will develop methods for IBR connection to radial distribution network and investigate the steady state stability of such systems. A typical radial distribution network can be seen in Fig 2.4.

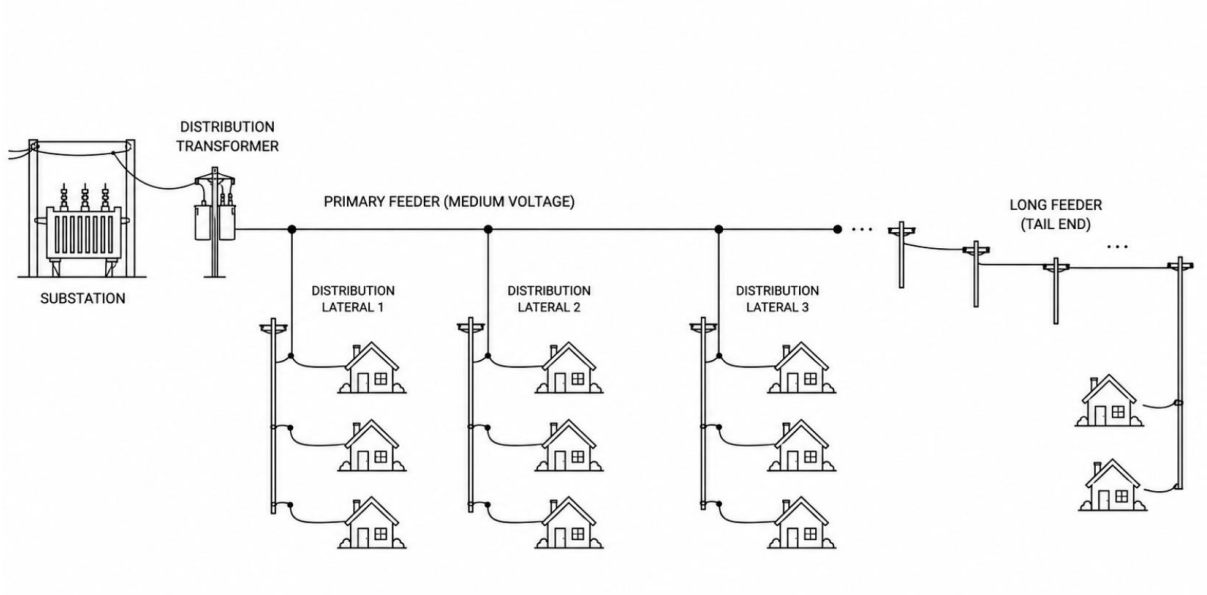


Fig. 2.4: A Typical Radial Distribution Network

The IEEE test bus standards are standardized power network models used by engineers and researchers to benchmark, test, and validate power system analysis algorithms. They are not physical hardware design rules, but rather standardized datasets containing bus, line, generator, and load data used to evaluate power flow, voltage stability, economic dispatch, and system optimization. The IEEE 33 Bus System has been adopted by IEEE organisation a standard for radial distribution networks [42].

The 33-bus system was developed in 1989 by Baran & Wu [43] to study the impact of reconfiguration in distribution systems on power losses reduction and load balancing has widely been used to study the different problems in traditional distribution networks. The recent development in smart power system associated with the integration of renewable energy to the power grid and the demand side management mechanisms require systems to be modelled and tested before grid integration is approved [44]. This research will integrate the developed system to IEEE 33 Bus System in order to investigate steady state stability and voltage profile across the network while detailed transient studies remains beyond the scope of core aims of this research. This will be done in order to analyse limits of the designed system and reflect real world constraints faced by grid operators as they transition towards a renewable energy future.

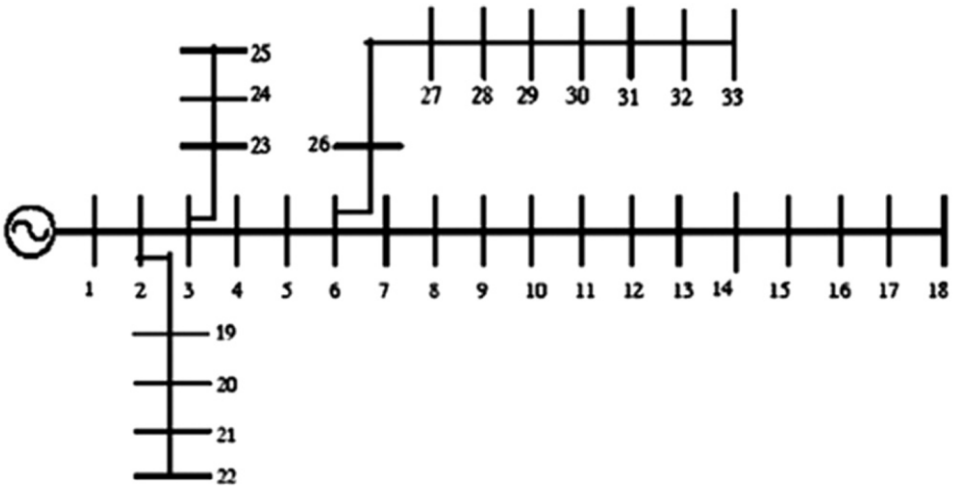


Fig. 2.5: The IEEE 33 Bus System [45]

The Australian AEMO modelling requirements the R1 and R2 validation [46]. Originally introduced in 1998 under schedule 5 for the Australian National Electricity Code (NEC) which establish the National Energy Market (NEM) rules, the R1 and R2 validation. The R1 modelling is the pre-commissioning validation requirement that establishes the component level stability benchmarks, and R2 modelling is the post-commissioning that validates the as built dynamic and steady state stability. Any model and real plant discrepancies are then catalogued, and plant and models are appropriately updated to reflect the as designed and as built systems are compatible. This literature as of today lacks such high-fidelity modelling which compounds the challenge for novel methods to

translate into real world applicability relegating valuable research to a purely academic domain for much longer than necessary which is one of the core motivations of this behind this research.

Other Regulatory frameworks, such as IEEE 1547-2018 and the more recent IEEE 2800 standards, are pivotal in guiding this transition and have been adopted by countries around the globe particularly in both Australia and New Zealand. The IEEE 2800, in particular, extends and improves specifications for IBRs at sub-transmission and transmission levels, explicitly requiring grid-forming behavior. These standards mandate advanced ride-through capabilities for abnormal voltage and frequency, along with other grid support functions [47] [48] [49].

2.6 Research Gaps, Synthesis and Thesis Position

A review of the literature suggests that most validation of contributions are simulation heavy and conduct deep analysis and synthesis on individual component level which through valuable leaves a gaps when it comes to systems level implementation and integration in real power systems. Alternatively, the literature focuses on broad system level comparative analysis that lacks sufficiently detailed treatment of the nuances involved at the component level. This research does not aim to replicate their findings but build upon existing knowledge to produce an end-to-end simulation validated with HIL testing to establish a GFM architecture that adopts and incorporates elements of industry practices such as the R1 and R2 modelling and validation discussed in the previous sections in order to present a meaningful results that demonstrates grid compliant characteristics.

Despite the advancement made this a comprehensive literature review has identified the following gaps that this thesis addresses:

- Lack of detailed end-to-end validation of GFM IBR topologies to established frequency and voltage regulation.
- Large Signal Transient Response characterised by major grid disturbances away from normal operating point such as three phase short circuit fault, followed by the GFM IBR ability to provide LVRT response without the use of FACTS devices.
- Multi-IBR power sharing and stability as multiple IBRs connect to a radial distribution network and maintain stability under steady state conditions.
- Modelling of power grid compliant systems and HIL validation of end-to-end systems

This thesis presents a validated, end-to-end design and implementation of a 100kW commercial-scale grid-forming inverter-based resource, modelled from the PV array and MPPT-controlled boost converter, IGBT-based three-phase inverter, and LCL filter, to droop-based grid-forming control validated in both islanded and grid-connected

microgrid configurations and confirmed through HIL testing against New Zealand grid code LVRT requirements.

Extending this validated unit to a four-IBR deployment on the IEEE 33-bus radial distribution network demonstrates that distributed grid-forming placement at this scale produces measurable voltage profile improvement at tail-end buses where a single unit does not, and reveals an inter-inverter instability limitation arising from the impedance characteristics of multiple parallel inverter connection at the 400V to 12.66kV step-up interconnection, a multi-converter interaction mode characterised in the literature but remains largely unresolved for parallel IBRs at commercial distribution scale. Together these results address a structural gap in the literature, which has extensively established the theoretical case for grid-forming control and the design of individual components and control loops, but has not produced validated end-to-end design methodology at the scale and network topology where commercial grid-forming IBRs are most likely to be deployed.

3 GFM IBR Design

This chapter outlines the methodology used to implement the core components required to design and validate the GFM controller implementation with the droop controller itself discussed in a dedicated chapter that follows. It covers the overarching system structure, the underlying mathematical modelling, the simulation of the core components used in the system design and all interim results that validate the component models required to implement the droop controller discussed in chapter 4.

A principled approach to view the goal of is to take a DC source and invert is polarity relative to the zero reference. This is achieved with the use of semiconductor devices that electrically switch the polarity of the DC source at the desired rate by introducing switching harmonics into the system. Three parallel switching circuits are timed such that three sets of switched DC signal are generated where the phase difference is determined by the switch delay between circuits. A filter is then needed to filter out the high frequency components leaving the three filtered AC signals. This is signal processing stages with which the inverter is able to generate the three phases of the required AC signals. However, connecting the resulting three phases of the generated AC signals to a power grid introduces additional complexity of grid synchronization.

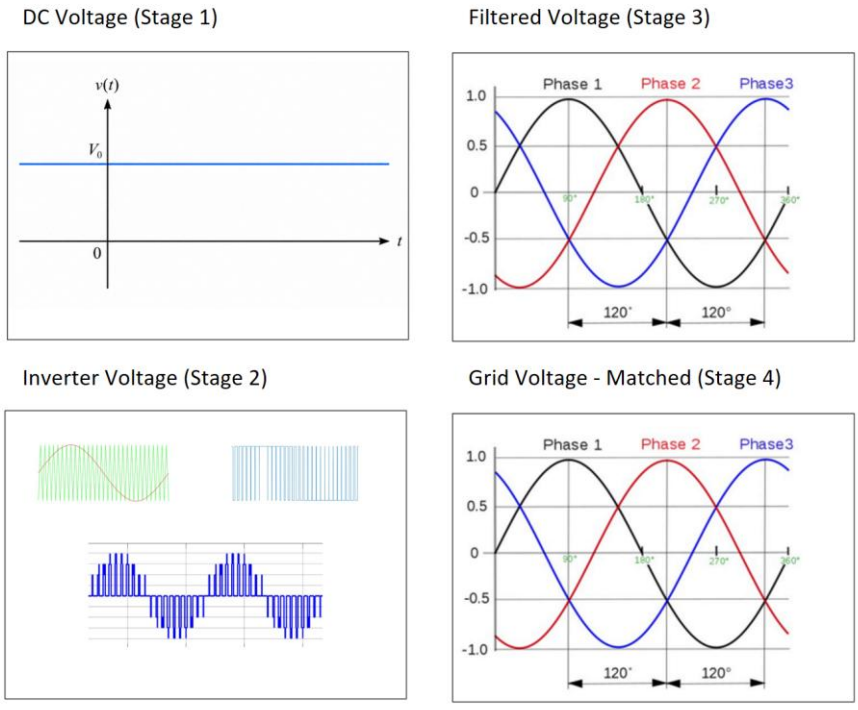


Fig. 3.1: The Signal Processing Model

A graphical representation of the signal processing model required to connect a DC energy source like solar PV to, and AC power grid is shown in Fig. 3.1 above.

Grid synchronization requires that each of the three phases generated by the inverter must share the same time domain reference as each of the phases of the power grid. In simplified terms when Phase A of the grid signal reaches an amplitude of zero, then Phase A of the inverter must reach an amplitude of zero, when grid amplitude reaches peak for any of the phases, the inverter amplitude of corresponding phase must also reach its peak. The grid and inverter phases must be maintained such that there is no difference in the grid phase and the corresponding inverter phase at all times (t) for the system to remain synchronised.

3.1 Mathematical Modelling of Critical Signals

Grid synchronization can be expressed mathematically by equations (3.1), (3.2) and (3.3):

$$V_{ibrA}\sin(\omega t + \theta_{ibr}) = V_{gridA}\sin\left(\omega t + \theta_{grid}\right) \tag{3.1}$$

$$V_{ibrB}\sin(\omega t + \theta_{ibr}) = V_{gridB}\sin\left(\omega t + \theta_{grid}\right) \tag{3.2}$$

$$V_{ibrC}\sin(\omega t + \theta_{ibr}) = V_{gridC}\sin\left(\omega t + \theta_{grid}\right) \tag{3.3}$$

Such that the following relationship given by (3.4) is always maintained:

$$\theta_{grid} - \theta_{ibr} = 0 \tag{3.4}$$

The grid synchronization equations described above is the outcome that the inverter controller needs to achieve. In a GFL IBR the controller must use a phase locked loop to measure the grid frequency and use it as a reference to up-regulate or down-regulate its own internal frequency to match the grid. In a GFM IBR the controller must maintain its own internal reference by calculating the frequency based on its active power balance or P/ω relationship. Therefore, first the P/ω and V/Q and relationship are modelled mathematically.

The underlying mathematical model takes the three-phase AC power signal represented by equation (3.5):

$$S(t) = A\sin(\omega t + \theta) \tag{3.5}$$

The three phase equations representing each phase given by (3.6), (3.7) and (3.8):

$$V_a(t) = V_{pk}\sin(\omega t + 0) \tag{3.6}$$

$$V_b(t) = V_{pk}\sin\left(\omega t - \frac{2\pi}{3}\right) \tag{3.7}$$

$$V_c(t) = V_{pk}\sin\left(\omega t + \frac{2\pi}{3}\right) \tag{3.8}$$

Physical controllers and simulations required discretized signals so that in can be numerically evaluated using compute modules in a controller or the computer CPU in the simulation case. This is fundamentally achieved by Direct Quadrature dq

transformations that turn AC signals into stationary DC quantities that enable precise, decoupled linear control and simplified system analysis. In the MATLAB environment the Clarke transform, and Park transform are used to produce the dq transformation.

The power invariant Clarke transform used in electrical systems takes the A, B and C phases of the measured signal and converts it into an equivalent two-phase stationary reference frame. The equation (3.9) below shows the power invariant Clarke transform:

$$\begin{bmatrix} x_\alpha \\ x_\beta \\ x_0 \end{bmatrix} = \sqrt{\frac{2}{3}} \begin{bmatrix} 1 & -\frac{1}{2} & -\frac{1}{2} \\ 0 & \frac{\sqrt{3}}{2} & -\frac{\sqrt{3}}{2} \\ \frac{1}{\sqrt{2}} & \frac{1}{\sqrt{2}} & \frac{1}{\sqrt{2}} \end{bmatrix} \begin{bmatrix} x_a \\ x_b \\ x_c \end{bmatrix} \tag{3.9}$$

This produces the $\alpha\beta$-zero signal that is then further processed with the Park Transform which produces the dq-zero signal. The Park Transform is a mathematical operation that converts time-varying, alternating current (AC) variables from a stationary three-phase reference frame into constant, direct current (DC) variables in a rotating two-phase reference frame. The equation (3.10) below shows the Park transform:

$$\begin{bmatrix} x_d \\ x_q \\ x_0 \end{bmatrix} = \begin{bmatrix} \cos\theta & \sin\theta & 0 \\ -\sin\theta & \cos\theta & 0 \\ 0 & 0 & 1 \end{bmatrix} \begin{bmatrix} x_\alpha \\ x_\beta \\ x_0 \end{bmatrix} \tag{3.10}$$

Direct Quadrature Transformation (dq)

The combined Clarke-Park matrix can be mathematically expressed as equation (3.11):

$$\begin{bmatrix} x_d \\ x_q \\ x_0 \end{bmatrix} = \frac{2}{3} \begin{bmatrix} \cos\theta & \cos\left(\theta - \frac{2\pi}{3}\right) & \cos\left(\theta + \frac{2\pi}{3}\right) \\ -\sin\theta & -\sin\left(\theta - \frac{2\pi}{3}\right) & -\sin\left(\theta + \frac{2\pi}{3}\right) \\ \frac{1}{2} & \frac{1}{2} & \frac{1}{2} \end{bmatrix} \begin{bmatrix} x_a \\ x_b \\ x_c \end{bmatrix} \tag{3.11}$$

The discrete time Clarke-Park matrix where $[k]$denotes a time step base on the sampling frequency depicted in (3.12) below:

$$\begin{bmatrix} x_d[k] \\ x_q[k] \\ x_0[k] \end{bmatrix} = \frac{2}{3} \begin{bmatrix} \cos(\theta[k]) & \cos\left(\theta[k] - \frac{2\pi}{3}\right) & \cos\left(\theta[k] + \frac{2\pi}{3}\right) \\ -\sin(\theta[k]) & -\sin\left(\theta[k] - \frac{2\pi}{3}\right) & -\sin\left(\theta[k] + \frac{2\pi}{3}\right) \\ \frac{1}{2} & \frac{1}{2} & \frac{1}{2} \end{bmatrix} \begin{bmatrix} x_a[k] \\ x_b[k] \\ x_c[k] \end{bmatrix} \tag{3.12}$$

The discrete time matrix is actually how the system will numerically be evaluated in simulations and is given above for completeness. However, the continuous time matrix is mathematically easier to follow.

The three-phase voltage signals can be substituted into the Clarke-Park matrix (3.13) to compute the dq components with substitutions the following:

$$\begin{bmatrix} v_d \\ v_q \\ v_0 \end{bmatrix} = \frac{2}{3} T_{dq} \begin{bmatrix} v_a \\ v_b \\ v_c \end{bmatrix} \tag{3.13}$$

The three-phase current signals can be substituted into the Clarke-Park matrix (3.14) to compute the dq components with substitutions the following:

$$\begin{bmatrix} i_d \\ i_q \\ i_0 \end{bmatrix} = \frac{2}{3} T_{dq} \begin{bmatrix} i_a \\ i_b \\ i_c \end{bmatrix} \tag{3.14}$$

The Power Calculation

The T_{dq} represents the Clarke-Park matrix described above. The resulting dqvoltages and currents, denoted v_d, v_q, i_d, i_q, are used to calculate active (3.15) and reactive power (3.16):

$$P = \frac{3}{2}\left(v_d i_d + v_q i_q\right) \tag{3.15}$$

$$Q = \frac{3}{2}\left(v_q i_d - v_d i_q\right) \tag{3.16}$$

where, v_d and v_q are the d- and q-axis components of the inverter output voltage, and $i_d$and i_q are the corresponding d- and q-axis components of the output current obtained through the synchronous reference frame transformation.

Real and Reactive power from the general power flow equation are given by (3.17) and (3.18):

$$P = \frac{V}{R^2+X^2}\left[R\left(V - V_g \cos\delta\right) + XV_g \sin\delta\right] \tag{3.17}$$

$$Q = \frac{V}{R^2+X^2}\left[X\left(V - V_g \cos\delta\right) - RV_g \sin\delta\right] \tag{3.18}$$

Applying negligible resistances, the equations (3.19) and (3.20) depict the reduced form:

$$P = \frac{VV_g}{X}\sin\delta \tag{3.19}$$

$$Q = \frac{V}{X}\left(V - V_g \cos\delta\right) \tag{3.20}$$

The equations rearranged after applying small angle approximation yields equations (3.21) and (3.22) below:

$$\delta \approx \left(\frac{X}{VV_g}\right) P \tag{3.21}$$

$$Q \approx \frac{V}{X}\left(V - V_g\right) \tag{3.22}$$

The Frequency Droop

By definition, electrical frequency (ω) is the time derivative of the phase angle $\omega = \frac{d\theta}{dt}$. The power angle δ (3.23) and (3.24) represents the differential and integral form of the phase deviation relative to the grid frequency ω^*.

$$\frac{d\delta}{dt} = \omega - \omega^* \tag{3.23}$$

$$\delta = \int (\omega - \omega^*)\, dt \tag{3.24}$$

Substituting in the small angle approximations gives a linear dependency (3.25):

$$\omega - \omega^* = \frac{d\delta}{dt} \propto -\Delta P \tag{3.25}$$

If this linear dependency is enforced via a controller active load can be shared without physical communication. This introduces the negative droop coefficient (m) to force the frequency to drop linearly as active power rises (3.26):

$$\omega = \omega^* - m(P - P^*) \tag{3.26}$$

The Voltage Droop

Rearranging the small angle approximated reactive power equation gives (3.27):

$$V - V_g \approx \left(\frac{X}{V}\right) Q \tag{3.27}$$

If this linear dependency is enforced via a controller reactive load can be shared without physical communication. This introduces the negative droop coefficient (n) to force the voltage to drop, and reactive power rises depicted by (3.28).

$$V = V^* - n(Q - Q^*) \tag{3.28}$$

The frequency and voltage droop equations can be rewritten express the nominal operating points real and reactive power, the reference set points frequency and voltage and the calculated magnitudes for frequency and voltage. This simplifies mathematical notations and allows for corresponding simulation variable names that trace back to the equations that derived them.

The droop laws for frequency and voltage modulation are defined as (3.29) and (3.30):

$$\mathrm{f} = f_n - m_p(P - P_o) \tag{3.29}$$

$$\mathrm{V} = V_n - m_q(Q - Q_o) \tag{3.30}$$

Where:

f and V are the frequency and voltage magnitude and $f = \omega/2\pi$;

f_n and V_n are reference setpoints;

P_o and Q_o represent nominal operating power;

m_p and m_q are the active- and reactive-power droop coefficients.

The droop control mechanism is established by the frequency and voltage droop equations derived. The controller architecture an begin to take form. The conventional droop controller uses a multi loop internal architecture which will be mathematically described in this section represents the proportion-integral control (PI) used in the outer voltage control loop and the inner current control loop.

The primary purpose of the outer voltage loop is to regulate the quality and amplitude of the local AC voltage waveform generated by the inverter, ensuring it acts as a stable voltage source for the grid or load. The primary purpose of the inner current loop is to protect the physical power electronics (IGBTs) from destruction while dictating instantaneous power flow by generating the switching targets for the IGBTs of the inverter.

Voltage Control Loop

The outer loop compares the reference dq voltages $\left(v_d^*, v_q^*\right)$ against the measured filter capacitor voltages $\left(v_d, v_q\right)$. It uses PI controllers and decoupling terms to output the reference currents $\left(i_d^*, i_q^*\right)$ for the inner loop. The active tracking of the PI is given by equations (3.31) and (3.32):

$$\tilde{\imath}_d^* = K_{pv}(v_d^* - v_d) + K_{iv} \int (v_d^* - v_d)\, dt \tag{3.31}$$

$$\tilde{\imath}_q^* = K_{pv}\left(v_q^* - v_q\right) + K_{iv} \int \left(v_q^* - v_q\right) dt \tag{3.32}$$

The cross-channel decoupling and feedforward are given by the equations (3.33) and (3.34):

$$i_d^* = \tilde{\imath}_d^* - \omega C v_q + i_{d,grid} \tag{3.33}$$

$$i_q^* = \tilde{\imath}_q^* + \omega C v_d + i_{q,grid} \tag{3.34}$$

Where:

K_{pv} , K_{iv} are the voltage loop proportional and integral gains

ω is the instantaneous virtual grid frequency from the droop calculator

C is the capacitance of the LCL filter

Current Control Loop

The inner current loop acts much faster than the outer voltage loop. It compares the reference currents $\left(i_d^*, i_q^*\right)$ against the measured inverter bridge currents $\left(i_d, i_q\right)$ and outputs the raw command voltages $\left(v_{inv,d}^*, v_{inv,q}^*\right)$ sent to the PWM modulator. The active tracking of the PI is given by equations (3.35) and (3.36):

$$\tilde{v}^*_{inv,d} = K_{pc}(i^*_d - i_d) + K_{ic}\int (i^*_d - i_d)\,dt \tag{3.35}$$

$$\tilde{v}^*_{inv,q} = K_{pc}\left(i^*_q - i_q\right) + K_{ic}\int \left(i^*_q - i_q\right)dt \tag{3.36}$$

The cross-channel decoupling and feedforward are given by (3.37) and (3.38):

$$v^*_{inv,d} = \tilde{v}^*_{inv,d} - \omega L i_q + v_d \tag{3.37}$$

$$v^*_{inv,q} = \tilde{v}^*_{inv,q} + \omega L i_d + v_q \tag{3.38}$$

Where:

K_{pc} , K_{ic} are the current loop proportional and integral gains

L is the inverter side inductor of the LCL filter

PWM Signals

The PWM modulator generates the switching signals for the sequenced control that is applied to the gates of the IGBTs of the inverter. The PWM signal generator performs comparator operation of a low frequency reference signal which 50Hz for this research and high frequency carrier signal which is canonical a piecewise that represents a triangular waveform.

The modulation signal is a control sinusoidal signal that represents the IBR system frequency (50Hz) and given by equation (3.39) below:

$$v_{control}(t) = V_{control}\sin(\omega_m t) \tag{3.39}$$

The carrier signal that represents a triangular waveform is given by piecewise equation (3.40):

$$x(t) = \begin{cases} \frac{4A}{T}t, & 0 \le t < \frac{T}{4}, \\ 2A - \frac{4A}{T}t, & \frac{T}{4} \le t \frac{3T}{4}, \\ \frac{4A}{T}t - 4A, & \frac{3T}{4} \le t < T. \end{cases} \tag{3.40}$$

The carrier signal and reference control signal are modulated with a comparator operation to produce a switch sinusoidal pulse width modulation SPWM output that are used to drive the IGBTs where the width of the pulses corresponds to the reference frequency. It is mathematically expressed as the equation (3.41):

$$v_o(t) = m_a \cdot V_{dc}\sin(\omega_m t) + \sum_{m=1}^{\infty}\sum_{n=-\infty}^{\infty} V_{m,n}\cos\left[\left(m \cdot m_f + n\right)\omega_m t\right] \tag{3.41}$$

Internal Reference Generation

It must also be noted that the instantaneous power and droop calculations are also used to generate the internal reference frequency of the IBR such that it does not rely on the grid frequency for reference. The active power droop equation calculates the instantaneous virtual frequency ω based on the measured active power P. The reference angle θ is then created by integrating this frequency over time.

The reference angle generation is given by frequency (3.42) and phase angle (3.43):

$$\omega(t) = \omega_n - R_p \cdot (P(t) - P_{set}) \tag{3.42}$$

$$\theta(t) = \int \omega\,(t)\,dt = \theta(0) + \int_0^t \omega\,(\tau)\,d\tau \tag{3.43}$$

The reactive power droop equation determines the target voltage magnitude based on the measured reactive power Q. This target magnitude is then mapped onto the dq coordinate system to form the explicit reference vectors $\left(v_d^*, v_q^*\right)$ needed by the outer voltage loop.

The reference voltage generation is given by equation (3.44):

$$V^*(t) = V_n - R_q \cdot (Q(t) - Q_{set}) \tag{3.44}$$

These reference signals can be set to the grid frequency by measuring the grid phase such as with a PLL for the initial pre-synchronisation so that the IBR can safely connect to an existing operational electrical grid. This step is carried out for safety and stability reasons of an already operational grid. The PLL is not required by the GFM IBR once its connected to an operational grid. In the case the GFM IBR is the only operational source on the grid or operating in islanded mode PLL based pre-synchronization is also not required. Simulations inherently mimic perfect black start conditions and as such are also not reliant of this step.

This section mathematically modelled the critical signals required to for the full system loop of the droop controlled GFM IBR. The equations discussed in this section will be implemented in subsequent sections using discrete time form formulations in either MATLAB code or Simulink blocks structures.

3.2 System Design Components

The previous section looked at the system design from a signal processing point of view and analytically defined. This section and subsequent sections will take the same analytical framework and implement the individual components of the system by numerically evaluation using the simulation software packages and the controller hardware in the loop C-HIL packages. The flow from concepts to analytical principles to design principles implemented in this thesis represents the overarching methodological philosophy applied in this research. In order to maintain structural clarity, this

overarching approach will be primarily applied to the core system components. Minor implementation details and granular specifications are reserved for their respective sections, ensuring the foundational narrative remains streamlined and accessible.

The component level design of a multi loop droop controller in the literature consists of a DC source that is connected to a three-phase inverter that feeds and LCL network to filter out the switching and harmonics to generate the three-phase signal that is connected to the power grid modelled via an infinite bus. The exact component level block diagram of a multi loop model can be seen in Fig. 8 below. The block diagram the conventional droop controller shows how the three-phase signal are measured to calculate the power which is feed to a voltage control loop which feeds into the current control loop. The primary purpose of the voltage control loop is to ensure the inverter accurately emulates a physical synchronous voltage source behind a virtual impedance. The current control loop is the high-bandwidth core of the cascade architecture, regulating the current flowing through the inverter-side inductor.

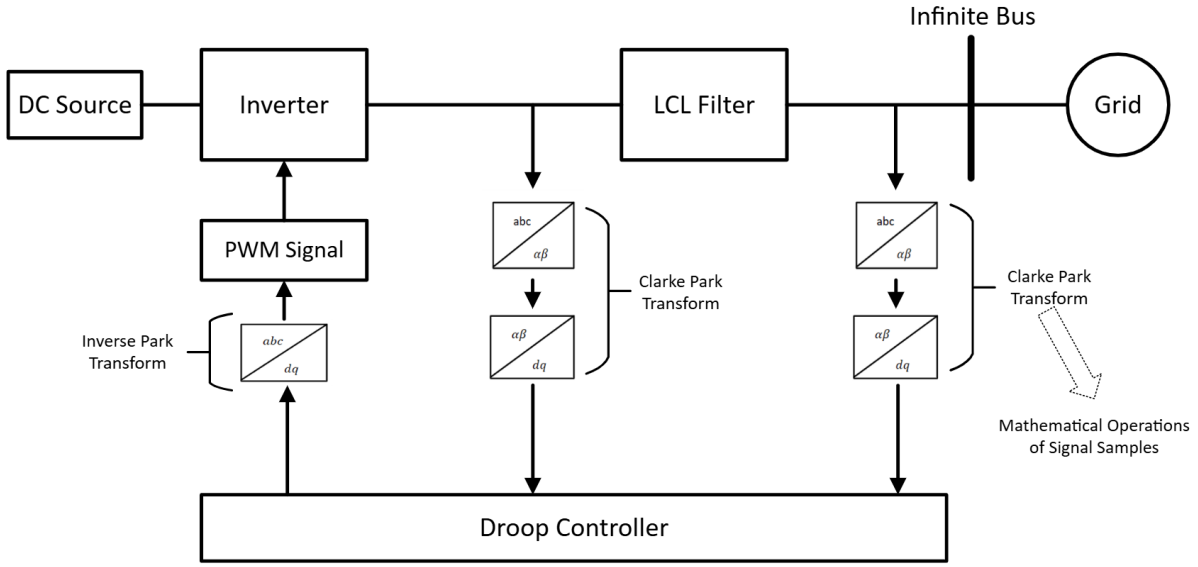


Fig. 3.2: Architecture of Conventional Droop Controller

The power is calculated the Clarke-Park matrix operations represented by the cascaded $abc \rightarrow \alpha\beta$ block and $\alpha\beta \rightarrow dq$ block shown in Fig. 3.2 are the mathematical operations performed on the sampled power signals. The following sections will introduce the design and implementation or each major sub-system that form the core of the IBR topology namely the DC Source, the Inverter and the LCL filter. The Droop Controller which from the critical component of the GFM IBR and the design and implementation of the microgrid and distribution topologies, although part of the research methodology will be introduced in their individual chapters.

3.2 DC Source

The DC Source model is a 100kW Solar PV array that uses MPPT via a Boost Converter to implement a DC Bus that will feed the system inverter. In order to enable modelling of more realistic characteristics than an ideal DC source but retain the additional energy capacity the system uses a slighted oversized DC Link relative to the 100kW rated design of the three-phase inverter so that the GFM IBR is capable of the faults tolerant response that will be discussed in the appropriate section. The results specific to the correct operation of this sub-component of the overall system will be discussed at the end of this section to keep such validations steps separate from core system results.

The 100kW Solar PV installation consists of a PV Array that interfaces with a DC – DC Boost Converter that is controlled via an MPPT controller to manage the maximum power tracking. The output of the boost converter is connected to shared DC Bus common to a Battery for energy storage and the system GFM IBR.

The core components consist of the following:

- The PV Array
- Boost Converter
- MPPT Controller
- Battery Integration (Bi-directional DC-DC Converter)
- DC Bus

DC Source Block Diagram:

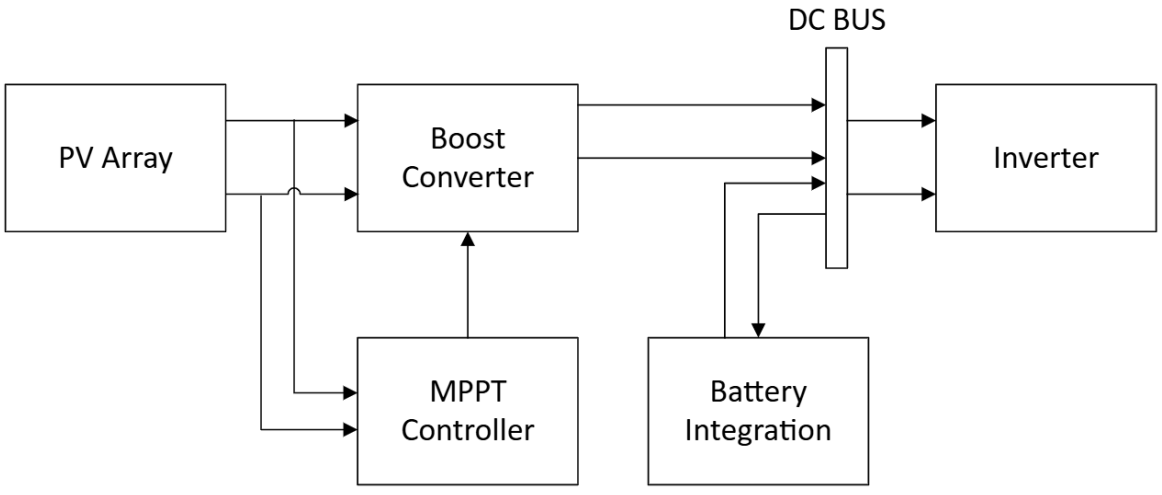


Fig. 3.3: Block Diagram of DC System

The DC Bus is where the IBR will access as its DC Source in the overall system architecture as shown in Fig. 3.3. The specific configuration of will be discussed along with overall system performance at the end of this section.

PV Array

The Photovoltaic Array consists of 470 panels of 214 watts each arranged in a 10 x 47 series parallel grid producing 100kW at 363 V with an MPPT voltage range of 270 V to 300 V. Rather than design this was selected based on the desired system constraints set out for this research. The voltage and current characteristics selected for the PV array implementation can be seen in Fig. 3.4.

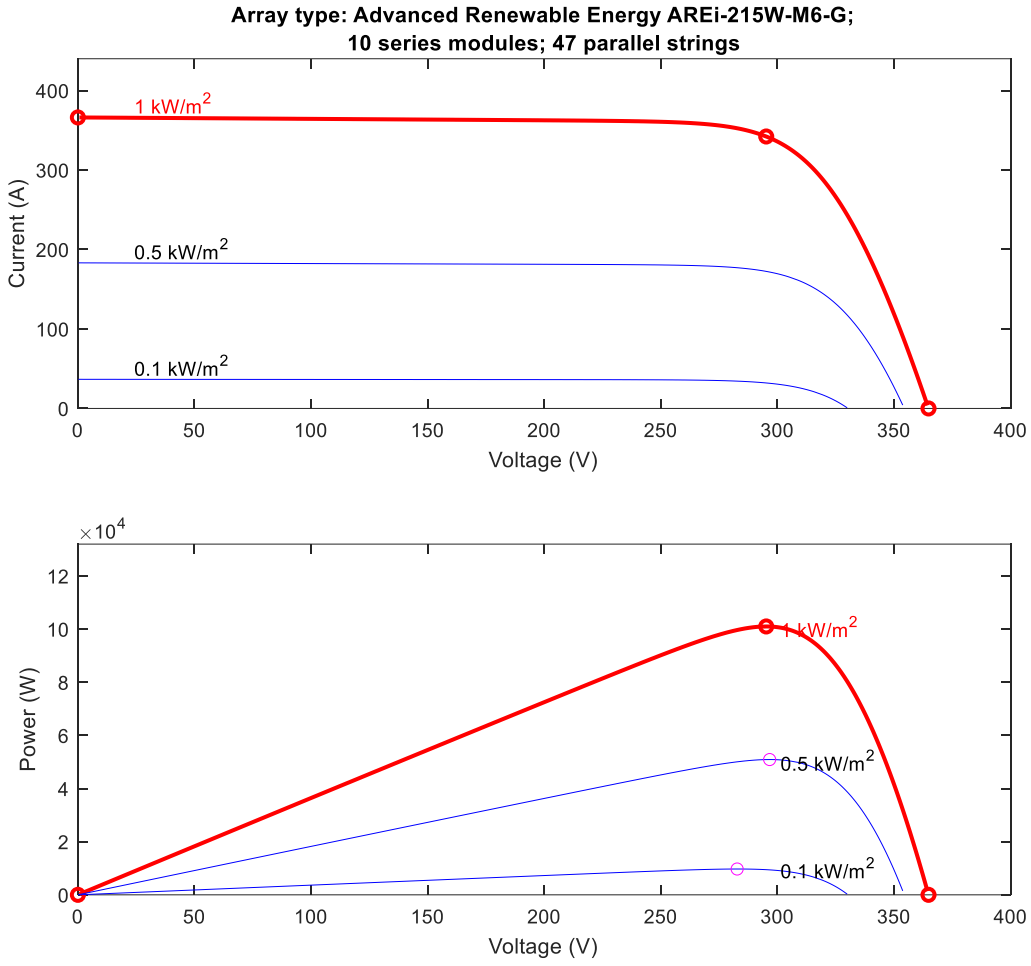


Fig. 3.4: The Power Curves of the PV Array

The maximum power point occurs at 295V at a solar irradiance of 1000 to produce a maximum power out of 100kW at around 342A. This was chosen as it not atypical of commercial rooftop solar or small utility scale distributed generation units and represents scalable distributed adoption across a radial network. The goal is to have multiple 100kW units that are scalable to 1MW without large structural changes to the internal topology which represents current trend in microgrid deployment [50].

Boost Converter Design

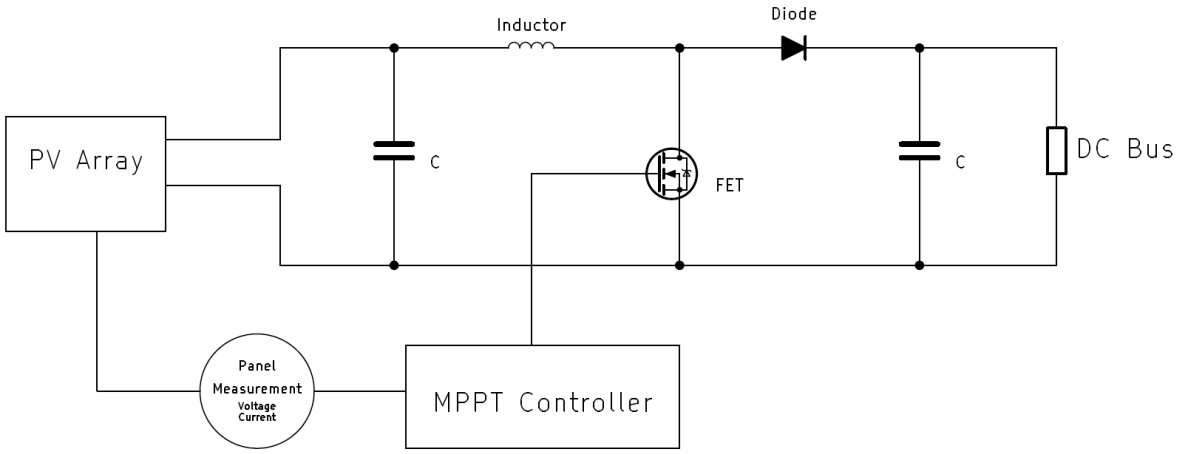


Fig. 3.5: Boost Converter Schematic

The power electronic converter designed for the system is able to boost the boost the array voltage of the PV panels from around 300V to around 600V maximum at the load.

Specifications:

Table 3.1: Datasheet with Boost Converter Data

Design Data Sheet				
Specification	min	nominal	max	unit
Voltage Input	250	300	350	V
Voltage Output	0	450	600	V
Rated Power	-	-	100	kW
Switching Frequency	-	5000	-	Hz
Current Ripple	-	5	-	%
Voltage Ripple	-	1	-	%
PV Side Capacitor		1000		µF
DC Bus Capacitor		3227		µF
Inductor		1.45		mH

The nominal values calculated for the boost converter are provided in Table 3.1 with standard engineering units are used to quantify the provided data.

The MPPT Controller

The MPPT Controller consists of two major components

- The Perturb and Observe (P&O) algorithm
- The PID Controller

The P&O algorithm is implemented in MATLAB software that takes the PV array voltage and current measurements as inputs and outputs a reference voltage to the PID

Controller. The PID controller consists of a reference signal to compare its input and the reference voltage generated by the P&O algorithm. It uses the reference voltage from the P&O to adjust the duty cycle of the pulse width modulation. The variable duty cycle of the PWM is used to regulate the input impedance of the boost converter as seen by the source, the PV array. This decoupling of the source and load allows the MPPT controller to track and extract maximum power. The PWM output is applied to the gate of the IGBT of the boost converter.

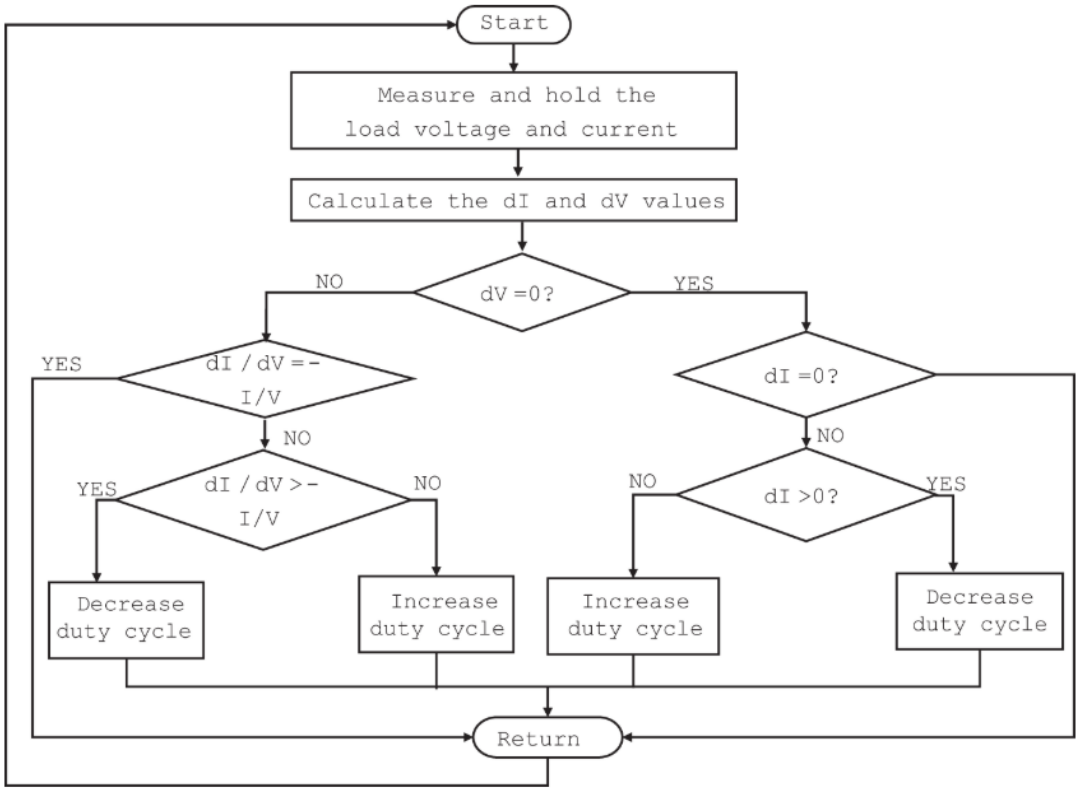


Fig. 3.6: P&O Algorithm for MPPT

The P&O algorithm calculates and holds the PV voltage and current measurements to calculate the starting power. Then it takes a step either up or down based on it sweep. Initially it will sweep down to find the maximum power point so it will take a step down in reference voltage, then it will take the new values of voltage and current and calculate the power at this point. If the new power is lower, then the previous power value it will then take a step up in reference voltage. If the new power value is higher than the previous power value, it will take another step down and take in new values of PV array voltage and current to calculate yet a newer power value. This process incrementally repeats until the maximum power point is reached by the controller. If the power value in each step is higher than the previous power the PID controller will reduce the duty cycle and if the power value is lower, it will increase the duty cycle to get closer and closer to the operating point at which maximum power is extracted from the panels. This makes the P&O algorithm a low cost yet robust controller to achieve maximum efficiency, and the

simple controller design makes it economically competitive [51]. A critical limitation is that this type of tracking will perpetually oscillate around the maximum power point and investigations into better algorithms such as incremental control and hybrid control approaches that combine computational and hardware approaches were investigated to mitigate this issue [52], they remain outside the scope of this thesis.

Battery Integration

The extraction of maximum power from the PV Array via the use of MPPT controlled Boost converter presents significant compatibility challenges at the DC Bus since the droop control IBR behaves as a constant voltage source behind and impedance to provide electrical power and regulation as discussed in the literature, MPPT objective remain to extract maximum power by continuously adjusting the voltage and current around the operating point based on the available solar irradiation [53]. This poses stability issues and risks to the inverter with the potential for extreme voltage spikes on the DC Bus. A reliable way to address this challenge is by integrating and battery to absorb surplus energy or provide surplus energy as and where needed. These BESS systems are becoming the more prevalent in industry though the current CPAEX for BESS integration remains high in the current market [54].

A simplified version of Battery Integration was achieved in this research with the implementation of a battery connected to the DC Bus via a bi-directional DC-DC converter. A full treatment of the practical constraints of BESS such as thermal management controller, battery management and cell load balancing components remains scope for future work.

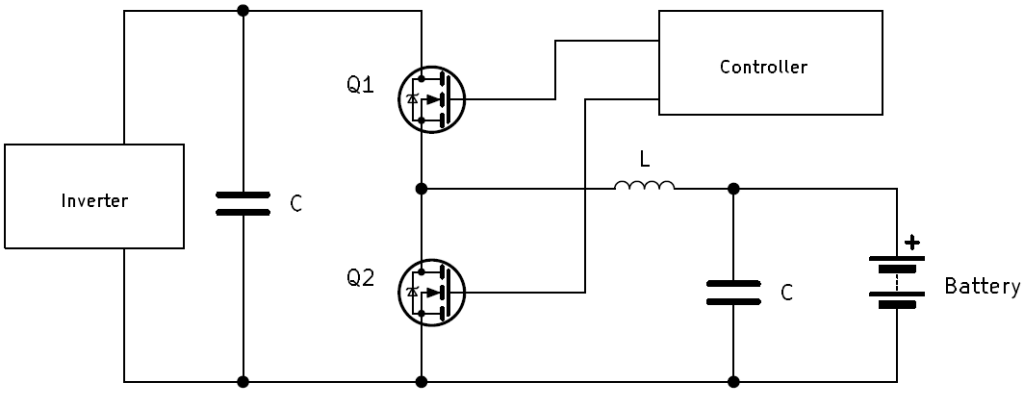


Fig. 3.7: Bi-directional DC-DC Converter

The component level testing to validate the operation of the bi-directional converter to is able to charge and discharge the battery starting with a 50% state of charge (SOC) with changing solar irradiation while maintaining the DC Bus voltage at around nominal operating point designed for this sub-system. The investigation shows that lower levels

of irradiation the converter is able discharge with positive current and when irradiation is high the converter goes back to charging with mode with negative current swing as shown in Fig. 3.8.

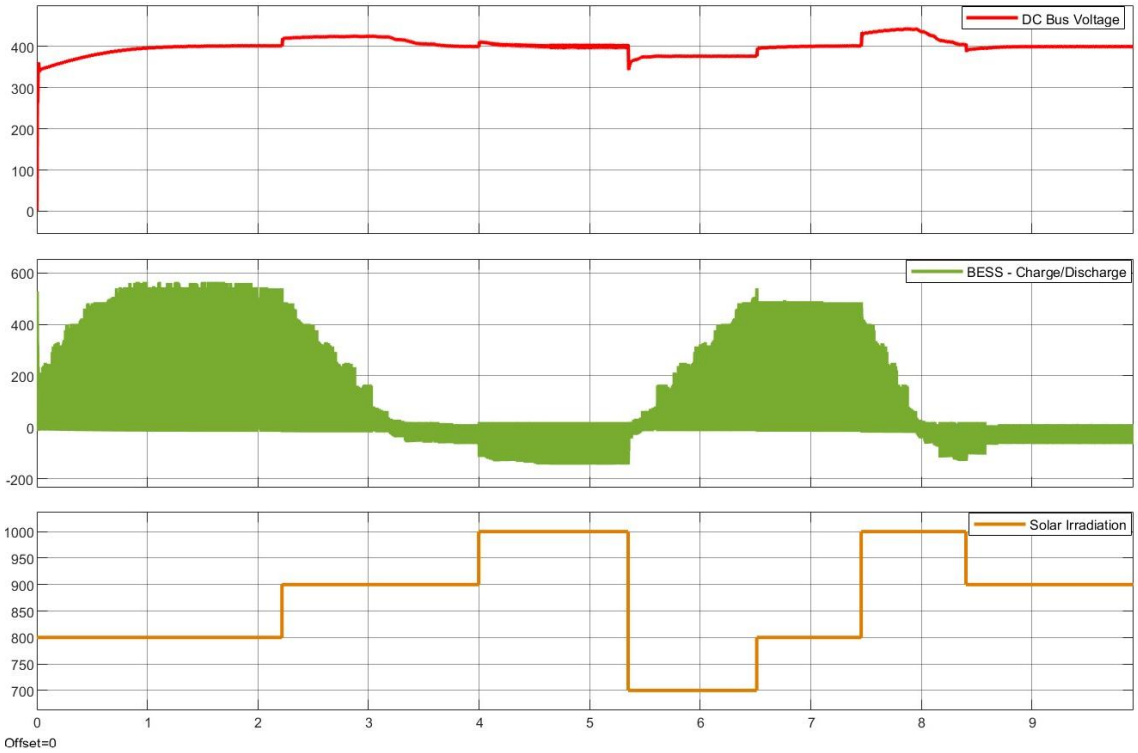


Fig. 3.8: Operation of Simplified BESS

Limitations Encountered with Simplified BESS Implementation.

It was also discovered that due to parasitic inductances the simplified design without snubber circuitry does exhibit ringing behaviors and voltage spikes [55] leading to slight over voltage conditions during increases in irradiation, though the voltage performance remained in the nominal range. The major limitation however is that the simplified BESS only operates in stable state over a very low irradiation range from 700 to 1000, solar irradiation below 700 leads to degraded performance. It was therefore concluded that an additional approach will be required to provide GFM IBR with the headroom required to respond to disturbances on the grid. This leaves two options going forward and both have tradeoffs that are significant to consider. The first is the easy option that most of the literature shows is the most prevalent option that is to model the DC Bus with an ideal DC source with unlimited capacity. This will simplify the modelling of the GFM IBR significantly, but it would also make for a less robust end to end system model that industry is beginning to adopt such as the AEMO R1 and R2 modelling discussed in the literature review, which is now mandatory in Australia [46]. The alternative is to oversize the DC Bus by having additional capacity from a larger PV array to provide extra capacity. Oversizing a PV array is not unsubstantiated in the literature as the 2018 paper by Sangwongwanich et al. investigates the associated reliability concerns for oversizing a

PV array in the context of grid feeding inverters. Furthermore, the noted that the current low-cost market environment for PV panels makes oversizing a considerable cheaper than alternative sources [56]. The economic claims will hold especially true for BESS solutions since they tend to be the more expensive energy solutions in the current market when comparatively analysed by Mohamed et al. in their 2022 paper [57]. However, specific oversizing ratios for GFM IBR are of interest and remain missing in the literature highlighting a gap that this research can contribute towards, although it is still not part of the core objectives of this thesis which are at the system level. This makes design decisions and trade-off analysis a bit more simplified. A PV array oversized by a factor of 2.0 will be implemented the details of which will be outline next.

DC Bus

A design of DC Bus involves replicating the single converter design and connecting the boost converter outputs in series while keeping the sources independent. This design was demonstrated suitable for a distributed photovoltaic topology and a reliable way to increase the DC bus voltage up to medium voltage applications in a 2024 paper by Ning et al. where the authors demonstrated a single stage IIOS converter topology specific for use with PV applications [58].

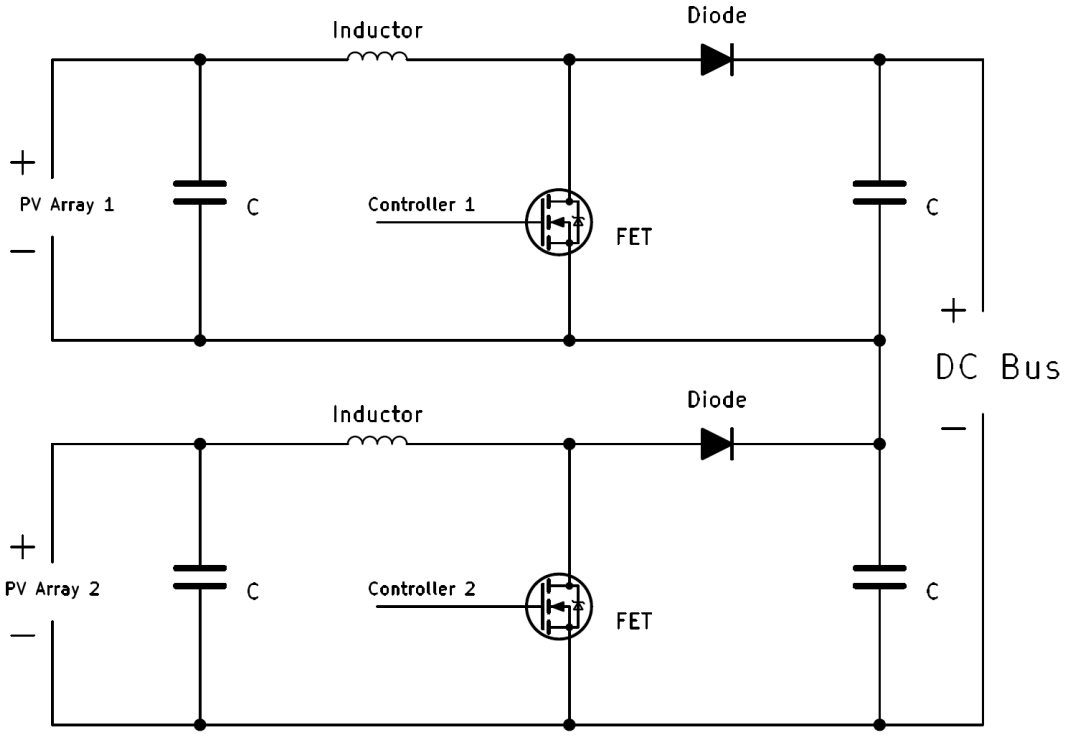


Fig. 3.9: Dual Boost Converter Topology

This design is able to double the voltage and power while the maximum current capacity remains the same. The alternative is to use a IPOS topology where the boost converters are able to increase the power by distributing the current through multiple parallel output

boost converter while keeping voltage the same as demonstrated by the 2022 paper by A. S. Alzahrani [59]. This design allows for a DC Bus with double the current capacity and power while keeping the voltage the same. Although the internal components have less stress the resulting increase in power output by increasing the current and keeping the voltage the same as the single converter setup is susceptible to higher losses the lines and requires higher diameter more expensive cabling making them more suited for electric vehicles applications. In power system applications the IIOS topology is the more sensible choice.

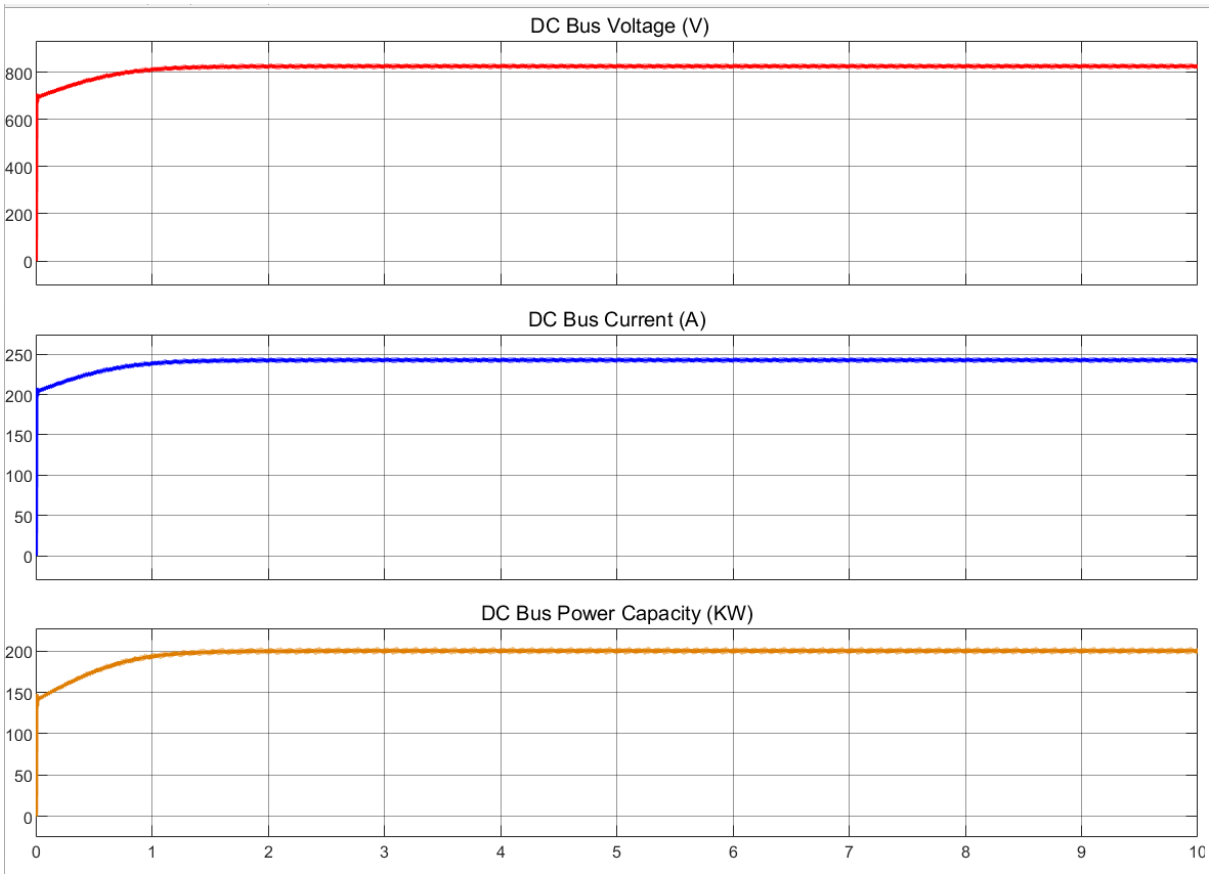


Fig. 3.10: DC Bus Measurements

The results from the DC Bus measurement show that the DC bus is able to supply 800V DC at 250 A, delivering a maximum of 200kW of power if needed. Fig. 3.10 shows the measured DC bus voltage, rated bus current and rated maximum power of the PV source. This provides the IBR with sufficient headroom to respond to grid disturbances. Future research can be carried out evaluating the optimum oversize required to maintain grid constraints while optimizing cost at the same time. In alignment with the goals of this research the DC source component is sufficiently oversized to provide the additional capacity to study the non-ideal characteristics of powering the IBR with a PV source.

3.3 Three Phase Inverter

The design of Three Phase Inverter is an IGBT based halfwave design common in PV systems. The systems consist of six IGBTs switched in pair sequence to change the direction of current flow per phase to produce switched DC output. The inverter takes DC input from the PV Array boost converter output discussed in the previous section and uses a sinusoidal pulse width modulation (SPWM) controller to generate the pulsed DC output of each half cycle of the fundamental frequency. The fundamental frequency for this research is 50 Hz as it the case with the New Zealand power grid. The block diagram of the three-phase inverter topology can be seen on Fig. 3.11.

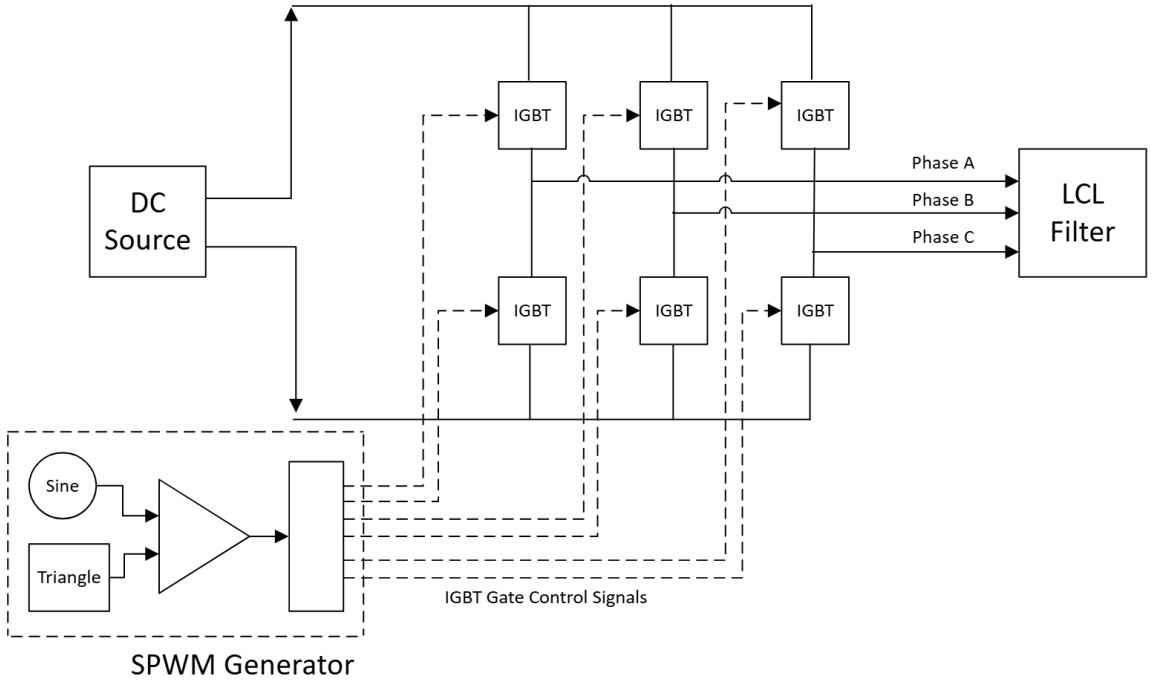


Fig. 3.11: Three Phase Inverter Topology

SPWM Generator

The SPWM controller uses a triangle waveform carrier signal and a unit sample of the modulating fundamental frequency reference signal and performs a sine-triangle comparator operation to produce a pulse width modulated signal where the duty cycle reflects a moving average voltage that follows a sinusoidal waveform of the fundamental frequency as shown in Fig. 3.12. The resulting SPWM signal is feed to a gate driver that boosts the low power control signal to a high power capable of driving the IGBT, this is the final gate driver signal. A typical embedded DSP controller will not be able to provide sufficient current from its typical 3.3V system to drive the gates of the IGBTs that are designed to be operated with a gate driver signal of around 15V in order to correctly switch on the transistor. The gate driver circuit that boosts the SPWM signal can be seen on Fig. 3.13.

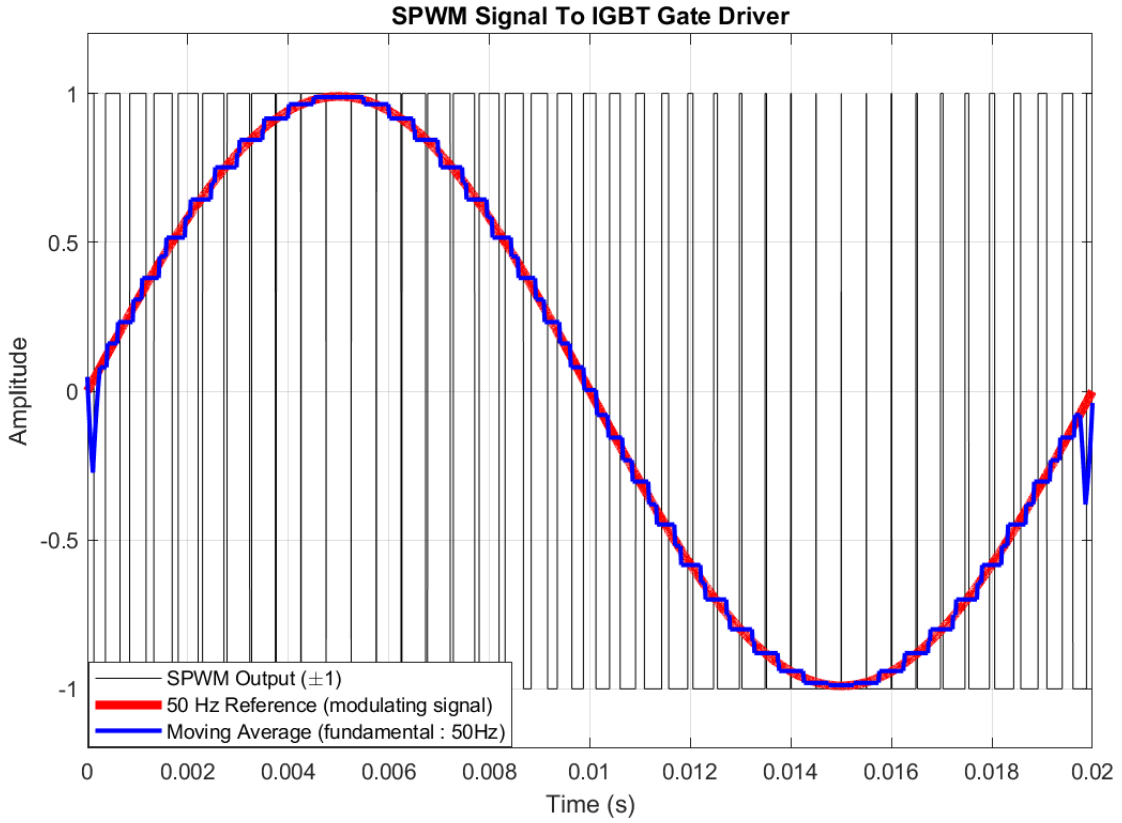


Fig. 3.12: SPWM Signal Generation

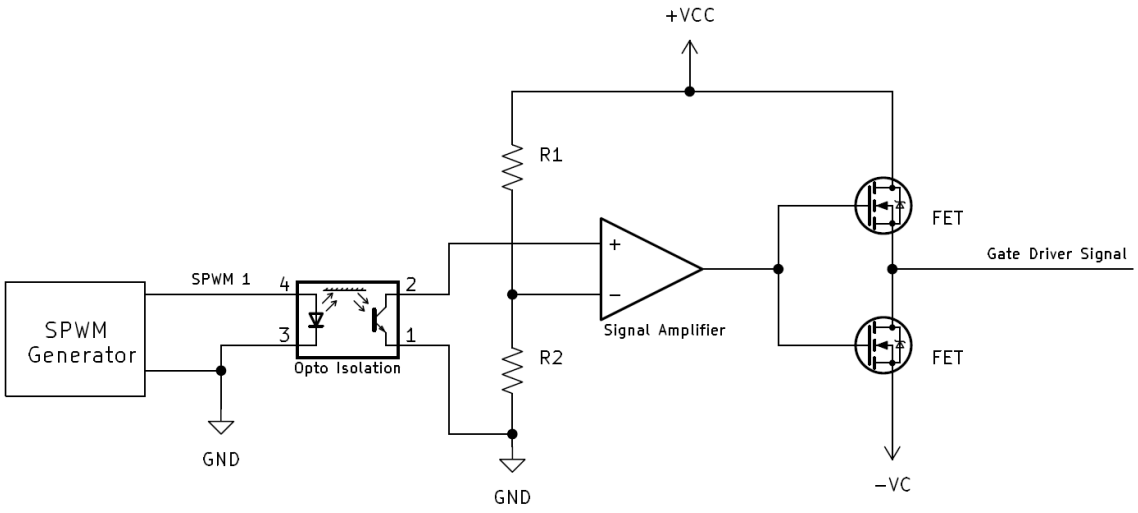


Fig. 3.13: IGBT Gate Driver Circuit

The operation of the IGBT based inverter and the correct signaling of the SPWM were verified but sub-system level testing of the operation. The result of this was three switched DC signals. This signal comprised of the fundamental 50Hz, and the switching harmonics introduced by the modulation steps that need to be filtered out in order to extract the pure sinusoidal signals.

IGBT Bridge

The internal parameters for the IGBT can be determined at the component selection stage, this research uses the generic IGBT models provided by the MATLAB environment to build the inverter component of the system. Although this limitation is noted here, the simulation is still able to benchmark characteristic behavior of IGBTs as it pertains to inverter design. It must be noted that a high-fidelity simulation will need to consider the dead time between switching the IGBT. The FFT analysis of the switched DC output of the inverter shows that the fundamental frequency of 50Hz is present in the output. This is the desired signal, however in this state is not useable on the as the added harmonics from the switching signaling and non-deal characteristics of the IGBT and the DC link.

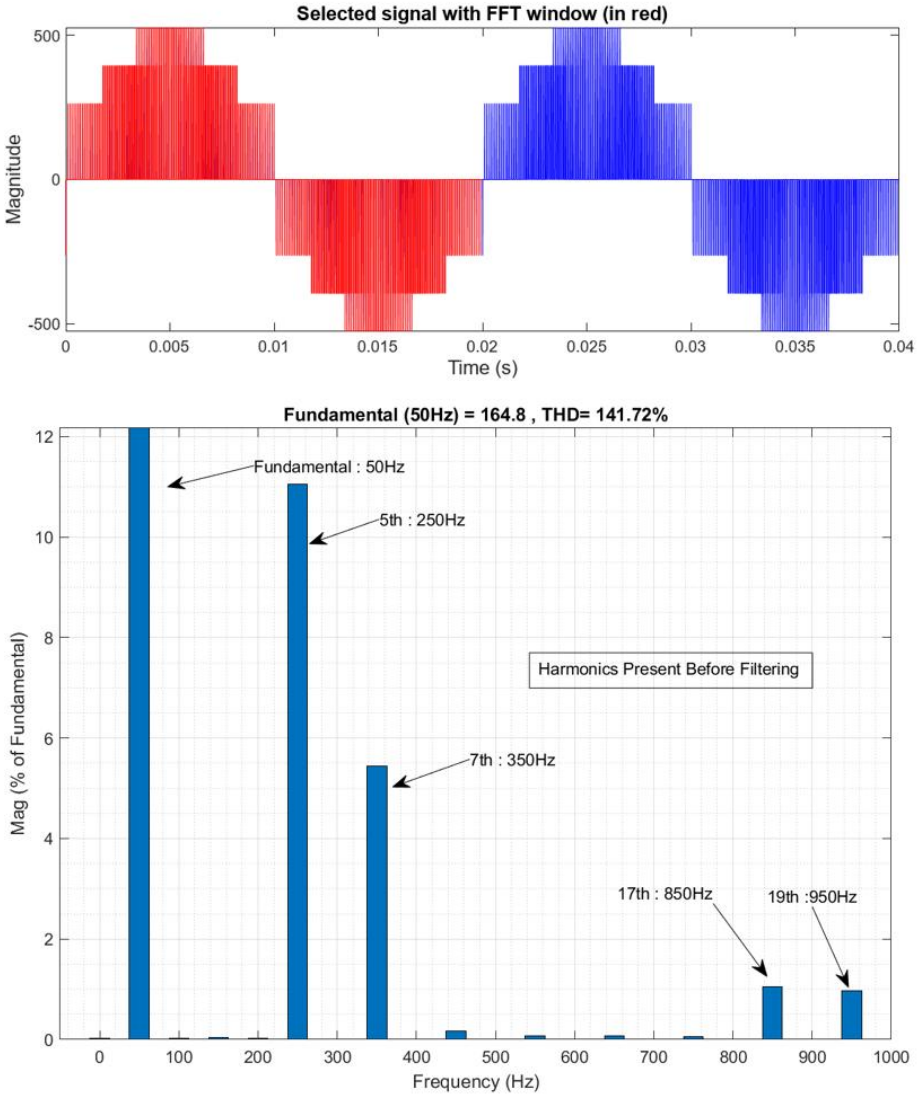


Fig. 3.14: Harmonics in Inverter Output

The low frequency harmonics present in the switched DC output of the inverter can be seen on Fig. 3.14, there will also be high frequency harmonics around 10KHz switching frequency not shown it the figure. Apart from the fundamental frequency Fig. 20 shows

the presence of odd harmonics dominating the distortion of the fundamental signal. This is indicative of the six-step half wave symmetry that approximately satisfies the following equation (3.45) below:

$$v(t) = -v\left(t + \frac{T}{2}\right) \tag{3.45}$$

The odd harmonics correspond to the switching harmonics with the 5th and 7th order harmonics are introduced by non-ideal IGBT characterise and dead time distortions effects. Furthermore, since SPWM uses a pure sine wave reference: $Vref(t) = sin(\omega t)$ the signal modulation naturally inherits symmetry. The absence of a 3rd harmonic in the inverter pole voltage before filtering also indicates that the waveform is largely free of distortions caused by half wave asymmetry such as DC offset, imbalance, or strong dead-time asymmetry. The description up to this point reflects a single phase of the three-phase AC signals required and the process is replicated for two additional signals, each separated in phase by 120 degrees from one another.

The resulting three inverter stage has been implemented as a three-phase, half wave topology comprising three IGBT switches, each connecting a respective output phase to the positive DC bus rail through a common return path. Gate control is achieved via sinusoidal pulse-width modulation, in which a high frequency triangular carrier signal is compared against three sinusoidal reference waveforms mutually displaced by 120°, with the modulation index governing the magnitude of the fundamental output voltage component. The resulting unfiltered phase voltages at nodes A, B, and C consist of unipolar pulse-width modulated waveforms that toggle between the full DC bus voltage and zero, with pulse widths sinusoidally envelope-modulated such that the fundamental frequency component is embedded within the switching pattern. The harmonic spectrum of each unfiltered phase voltage comprises the desired fundamental together with switching-frequency harmonic clusters appearing at integer multiples of the carrier frequency, accompanied by symmetrical sideband pairs at offsets of even multiples of the fundamental frequency, consistent with the theoretical Bessel function decomposition of SPWM waveforms. As the half-wave configuration precludes active driving of the phase output below the negative DC rail reference, the waveform remains strictly unipolar at each phase node, the alternating line-to-line voltage necessary for AC load excitation is therefore recovered differentially across phase pairs, with the DC offset component cancelling in the subtraction. At this stage of the design, prior to output filtering, the inverter successfully synthesises a three-phase SPWM voltage pattern carrying the intended fundamental component, establishing the basis for subsequent harmonic attenuation through the output filter network as shown in Fig. 3.13 above. This signal needs to be filtered before it can be used to supply power to the electrical grid and is discussed in in the next section.

3.4 LCL Filter

Following the characterization of the inverter stage and its voltage pattern established at the output nodes, the focus of the design now shifts to conditioning the inverter output for grid connection. As characterised in the preceding section, the unfiltered phase voltages contain significant harmonic content concentrated at the switching frequency and its sidebands, which must be attenuated to levels compliant with applicable grid interconnection standards before the inverter output can be coupled to the network. The following section details the design of the output filter network, which serves to extract the fundamental frequency component from the switching waveform and present a low-distortion sinusoidal voltage and current to the point of common coupling.

LCL filters are preferred over single inductor L filter or inductor capacitor LC filters in grid-connected three-phase inverter applications primarily due to their superior harmonic attenuation capability for a given total inductance and therefore a more favourable trade-off between filtering performance, physical size, and power loss. A single L filter attenuates switching harmonics at only −20 dB/decade, necessitating a prohibitively large inductance to meet grid harmonic injection standards such as IEEE 519 or IEC 61000-3-2, which increases copper losses, voltage drop, and dynamic response time. An LC filter improves attenuation to −40 dB/decade but introduces a resonance that is difficult to manage without damping, and the capacitor interacts unfavourably with the grid impedance in ways that compromise stability. The LCL topology achieves −60 dB/decade attenuation beyond its resonant frequency, allowing significantly smaller inductors and capacitors to meet the same harmonic standards, reducing both conduction losses and the physical footprint of the filter assembly. The inherent resonance of the LCL filter, while requiring active or passive damping strategies, is well characterised in the literature and manageable through established design methodologies [60] [61] [62]. For these reasons the LCL filter has become the industry and academic standard for grid-connected voltage source inverter output filtering where compliance with harmonic standards must be achieved without sacrificing converter efficiency or bandwidth.

LCL Filter Configuration and Constraints

The LCL filter consists of four primary components which are the following:

- Inverter Side Inductor L_i
- Grid Side Inductor L_g
- Feedback Capacitor C_f
- Damping Resistor R_D

In addition to these, there are two additional small resistance in the circuit namely the series resistor with the inverter side inductor R_i and the series resistor with the grid side inductor R_g and they represent the losses on the line and since, in real systems these

values must be determined by the current rating and thermal limits of the inductors selected, for the purpose of this research will be considered negligible.

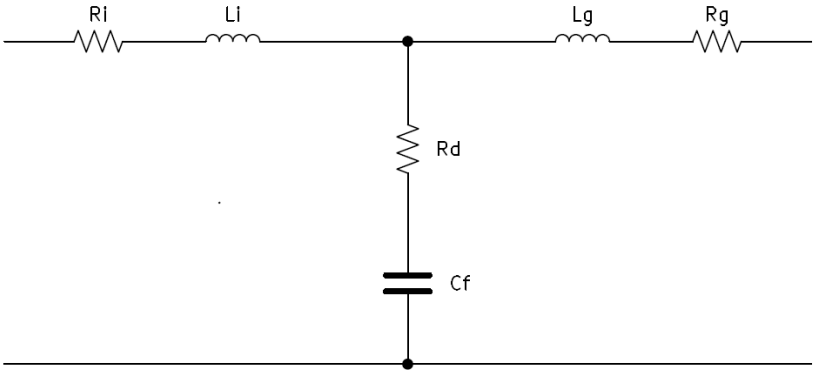


Fig. 3.15: LCL Filter Configuration

The literature describes different methods for calculating the relevant parameters of the LCL filter. However, no single optimum method has been established, instead the current consensus moves away from simple rules and toward a systematic process that balances competing trade-offs. The optimum remains applications specific and is achieved by defining a cost function, usually aiming for minimum size, weight, or power loss and subject to specific operational constraints. In the 2005 paper M. Liserre et al. defined one method of calculating these parameters suitable for an inverter application which defined certain characteristics as follows [60]:

- Establish base impedance and capacitance using inverter rated power and grid voltage
- Capacitor selection typically constrained by reactive power limit to ensure power factor remains within specification, typically 5% of rated power.
- Inverter side inductor is primarily determined by the maximum allowable AC ripple current due to switching, typically 10% to 30% of rated current.
- Grid side inductor is selected based on the harmonic attenuation requirements of grid codes
- Resonant frequency is constrained between ten times the grid frequency and half of the switching frequency $10 \cdot f_g < f_{res} < 0.5 \cdot f_{sw}$ in order to avoid control instability.
- Damping resistance is needed to improve the filter response by suppressing the resonance peak inherent to LCL filters.

The method used to determine the values for LCL filter involved the combination of the methods from M. Liserre et al. [60] and experimental determination such the resulting filter was able to optimize for the reduction of total harmonic distortion (THD). In grid connected applications THD is the most relevant parameter as all other critical

parameters affect the IBR in terms of dynamic response, efficiency and fault tolerance, for example a GFL IBR can disconnect from the due to limited ride through capabilities and a GFM IBR ability to ride through faults will determine its profitability and stability. The grid remains largely isolated from such IBR issues, THD on the other hand directly affects the power quality on the grid and subject to stringent grid codes for connection viability.

Table 3.2: LCL Filter Parameters

Key Parameter	LCL Parameters		
	Description	Value	Units
L_i	LCL inverter side inductor	1.2	mH
L_g	LCL grid side inductor	600	uH
C_f	LCL capacitor	80	uF
R_D	Damping Resistor	1.0	Ω
$R_i = R_g$	Parasitic Resistances	0.001	Ω

Table 3.2 shows the calculated and experimentally determined values for LCL filter used in this research.

Harmonic Distortion and Grid Compliance

In order to determine the THD is grid compliant, the IEEE 519-2022 Standard was applied to the design parameter selection. Most grid codes utilize this standard, and it specifies a maximum of 5% individual harmonic n^{th} order distortion and a THD of 8% for voltages ranging from 0 to 1kV and for voltages ranging from 1kV to 69kV a maximum individual harmonic distortion of 3% and a THD of 5% maximum [63]. In alignment with the goals of this research to enable the designed GFM IBR to power a microgrid network connected to the wider electrical grid on a radial distribution network the voltages involved are 400V AC at the microgrid level and 12.66kV AC on the radial distribution network. This constrains the designed IBR LCL filter to a maximum THD of 5% for overall compatibility at both microgrid and distribution network level.

This was verified at the full system level but not part of the core results presented in this thesis as such the methods and results are discussed in this section. The GFM IBR connected to the micro grid the simulation was run with no load and load step change and the subsequent IBR waveforms were captured to conduct a FFT and THD analysis using the tools in the MATLAB environment. When the signal settled after the small signal response the steady state signals were sample to produce a spectrum of fundamental and the relative amplitudes of the n^{th} order harmonics present in the filtered signal. Whereas Fig. 20 showed the harmonics present in the unfiltered inverter output Fig. 3.16 below shows the filtered output from the LCL filter and verifies that the filter was able to

achieve a THD of 4.93% on voltage signals and the highest individual harmonic distortion of 2% for the 5th order harmonic. The FFT window shown by the voltage signal in red represents the state of the system after the system is switched from no-load to load condition on the microgrid connect to the grid via infinite bus.

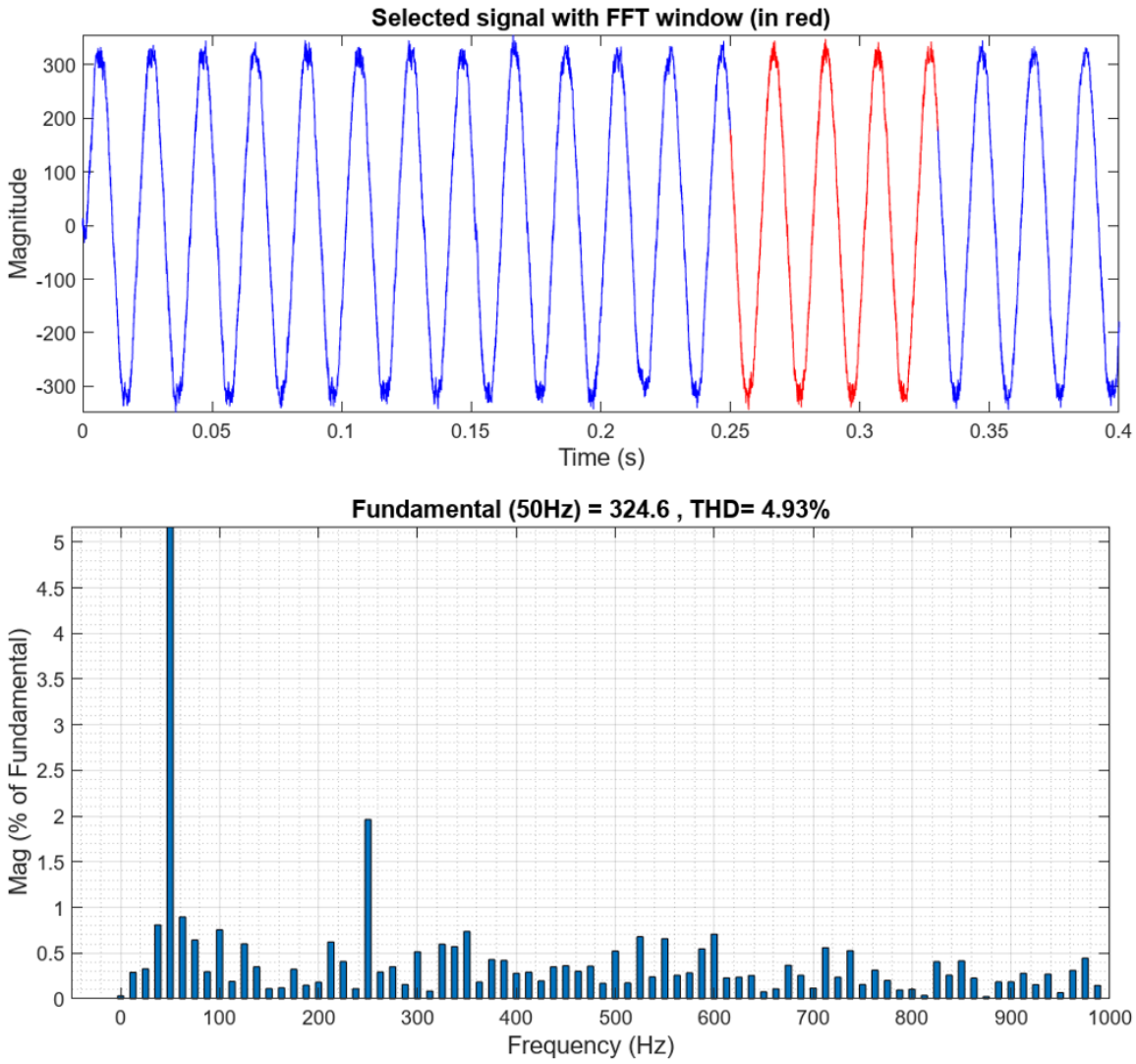


Fig. 3.16: Voltage THD of Final GFM Inverter Design

Similarly, the IEEE 519-2022 Standard defines the maximum individual harmonic distortion and THD for the current supplied by an inverter. However, for the allowable current distortion the rated system power is considered, systems that are rated for to operate at voltages that range from 120V to 69kV, the currents below 50A allow for a maximum THD of 8% and for currents ranging from 100A to 1000A, the maximum allowable THD is set at 15% by the standard [63]. This means that the designed filter must be able to maintain the current distortion between 8% and 15% to be considered grid compliant. The 100kW system is connected to a microgrid supplying a residential environment while connecting to a radial distribution network is expected to supply a currents in the 100A to 1000A range of the standard and a rated full load at a power factor

of 0.9 would draw around 200A of peak current per phase from the IBR. The harmonic analysis results for the implemented system shows on Fig. 3.17 that for low currents below 50A rms the maximum THD is 2.33% within two cycles of a load change.

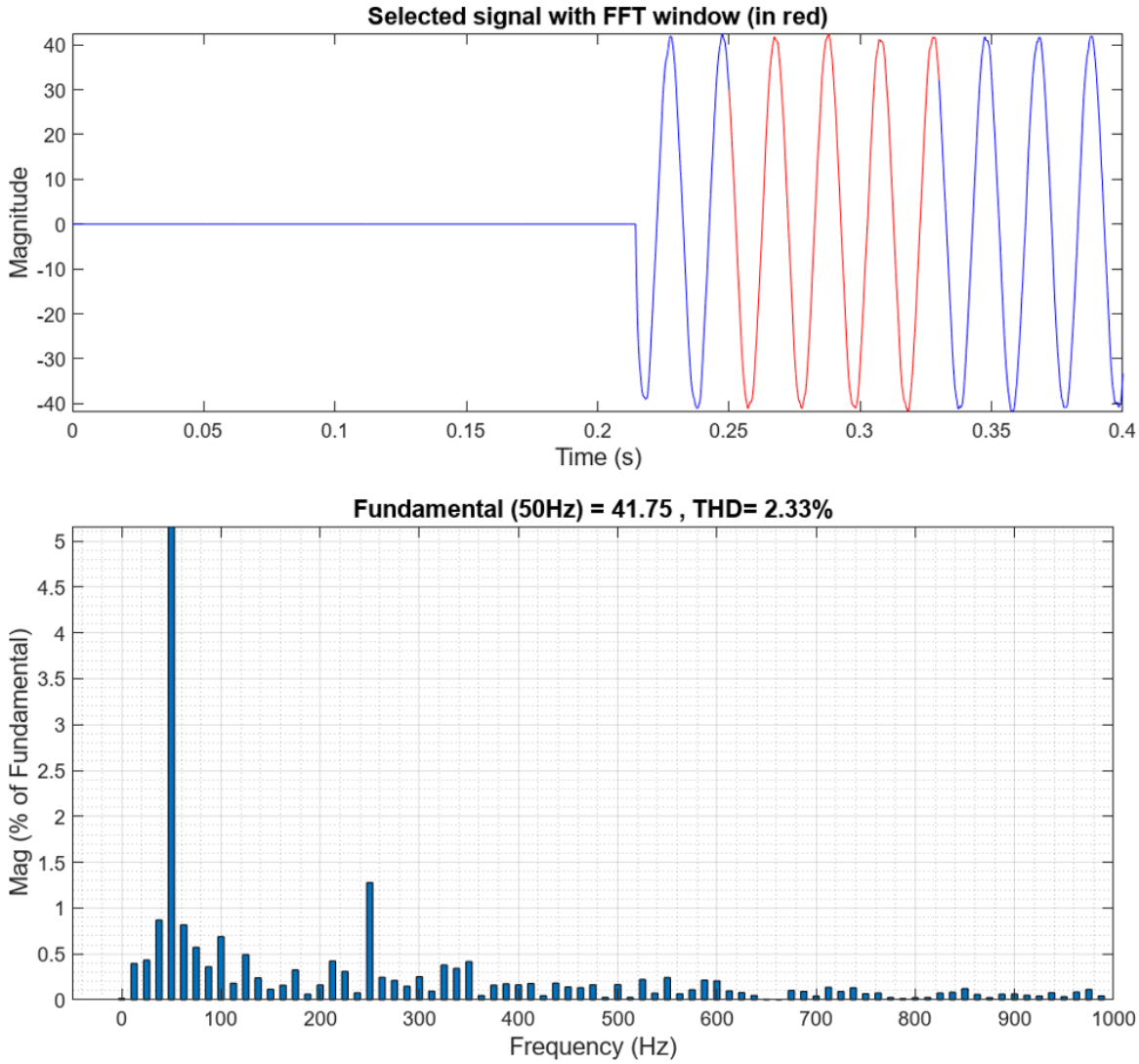


Fig. 3.17: Low Current THD of Final GFM Inverter Design

The harmonic analysis results of with the rated load on the inverter shows on Fig. 3.18, a maximum THD of 6.3% which is much lower than the allowable 15% by the standard and as such can be concluded that for goals of this research this result shows a very fast harmonic response that would be considered high performance in practical grid applications for low currents and would satisfy the grid code requirements. In the grid management of harmonics introduced by the connection for IBRs to the power grid is currently of concern and is actively being consulted on by Transpower in order to revoke dated guidelines and adopt new standards, this process is being carried out as of 2024 and is likely ongoing in development [64] [65]. This research successfully designed and implemented an LCL filter within a complete grid connected inverter model.

The simulation results demonstrated voltage and current harmonic performance that met or exceeded the limits specified by IEEE 519 and the applicable New Zealand grid connection requirements. Furthermore, the methodology developed in this thesis provides a framework for evaluating harmonic performance and filter design in grid connected inverter systems, which may be applicable to future grid forming inverter studies and emerging industry practices.

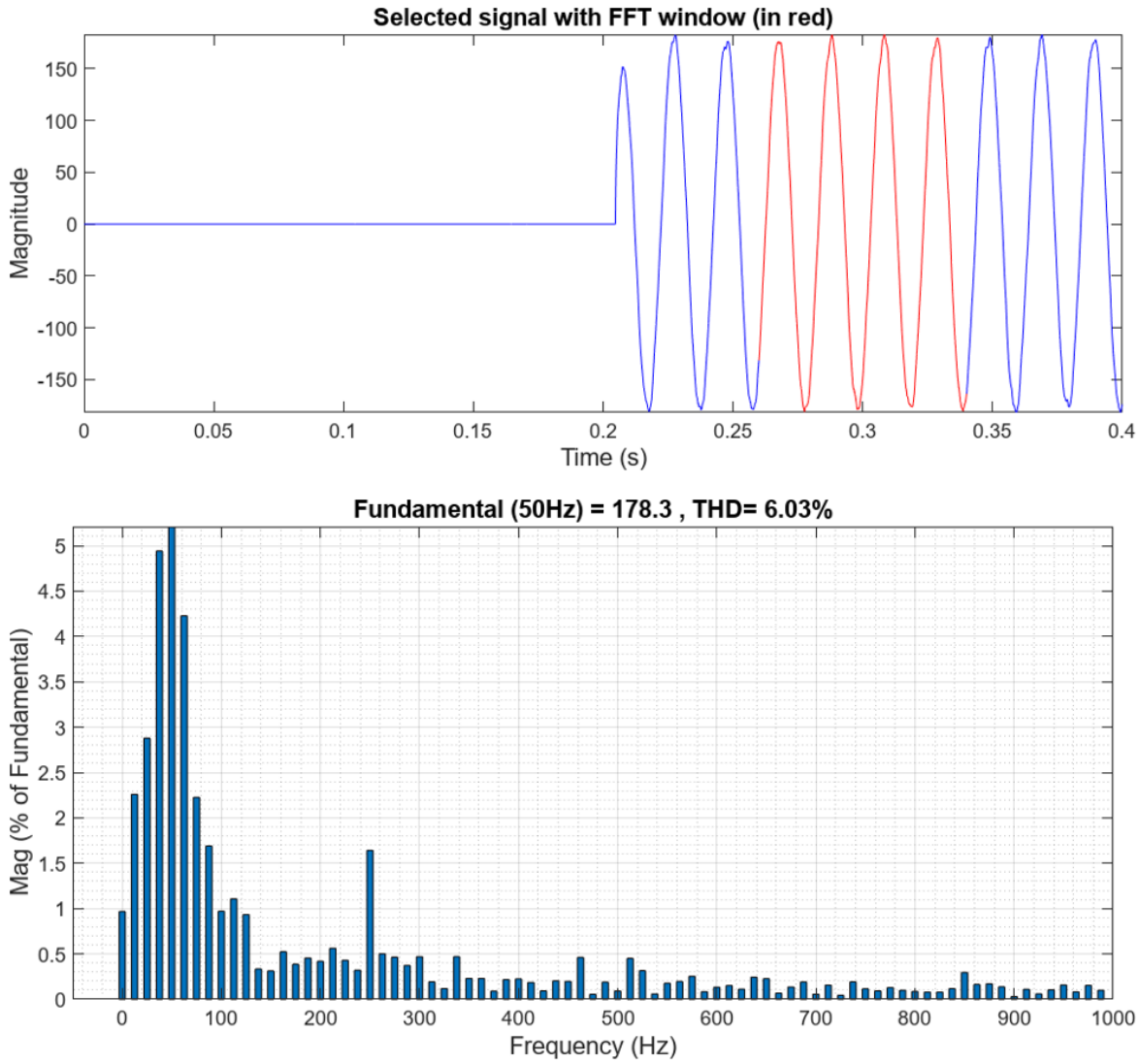


Fig. 3.18: High Current THD of Final GFM Inverter Design

This chapter modelled the core system components required to produce the AC signals that are grid compatible. However, to manage the flow of real and reactive power to the grid requires a control layer to stably interact with a dynamic system. The detail design and implementation of the droop controller used to achieve autonomous power sharing, and system regulation will be introduced in the following chapter.

4 Droop Controller Design

This chapter introduces the detailed design and implementation of the Droop Control used by the inverter to provide the necessary frequency regulation, the voltage regulation and the autonomous power sharing required by an IBR to establish its grid forming characteristics. The subsequent sections of this chapter systematically takes the reader through the power calculation, the application of frequency and real power droop, the voltage and reactive power droop, the internal reference signal generation, the outer voltage control loop and the inner current control loop and that provide the necessary signals required to generate the PWM signals to driver the inverter gate introduced in the pervious chapter. The resulting system provides a regulated GFM IBR that can supply a microgrid and connect to distribution network as a DER.

4.1 Droop Control Architecture

The droop controller implemented for this research is a multi-loop conventional droop controller. The architecture of the controller is shown in Fig. 4.1 shows the breakdown of sub-components and control flow between the components.

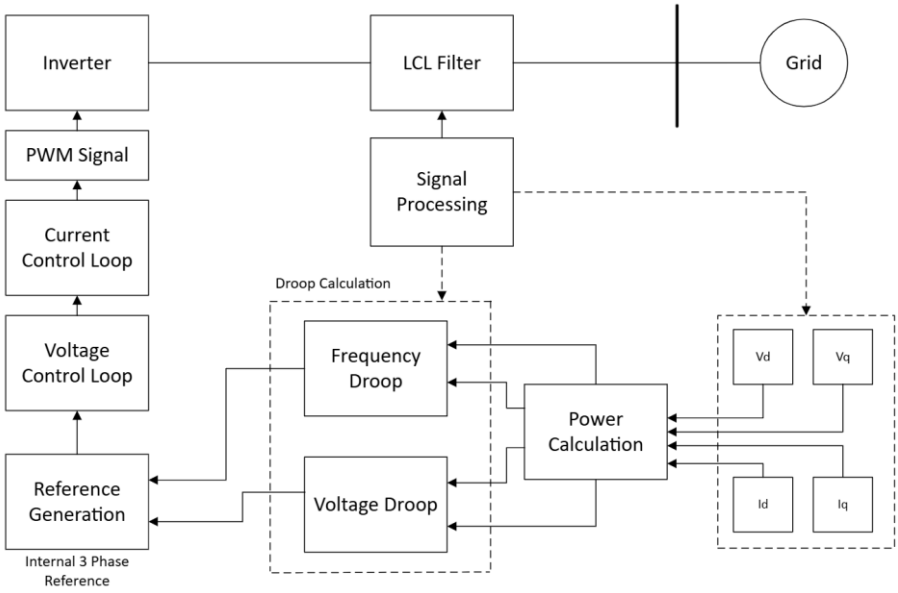


Fig. 4.1: Droop Controller Architecture

The established equations from the mathematical modelling from chapter 3.1 are applied to implement the droop controller for the GFM IBR in this research. The multiple dq transformations that use the Clarke-Park matrix operations that have been established in the mathematical modelling are abstracted to dq components in this chapter for readability of illustrations.

4.2 Power Calculation

The power calculation takes the dq components and computes instantaneous three-phase real power P and reactive power Q from the measured inverter output voltages and currents at the LCL filter output. The instantaneous active and reactive power are computed using the dq-frame voltage and current measurements obtained via Park's transformation applied to the three-phase LCL filter output quantities. This formulation is consistent with the instantaneous power theory and provides DC quantities in steady state, which are amenable to straightforward filtering and control processing. The factor of 3/2 arises from the amplitude-invariant Park's transformation convention.

These are instantaneous quantities and contain double-frequency ripple components at $2\omega_0$ under unbalanced conditions and switching ripple under all conditions and require a filtering. A first order filter is used to filter the instantaneous P and Q measurements to extract the fundamental frequency average values that the droop law should act on, thereby removing switching harmonics and double-frequency components. A low cutoff frequency provides effective attenuation of switching ripple and measurement noise but introduces significant phase lag that slows the droop response to genuine power disturbances. A high cutoff frequency improves dynamic response but passes residual ripple into the droop calculation, causing erroneous frequency and voltage reference modulation.

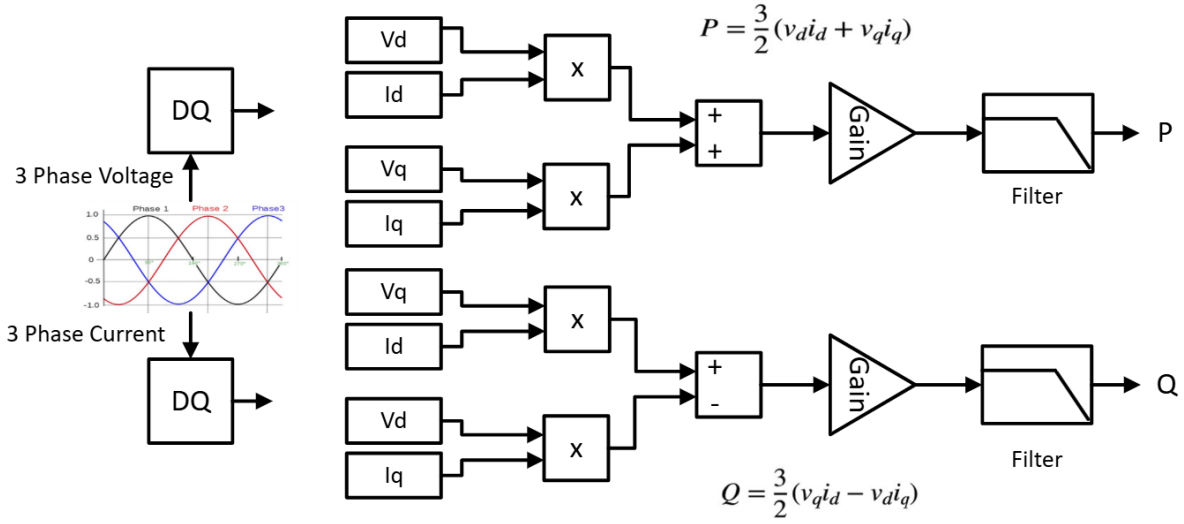


Fig. 4.2: Power Calculation Block of Droop Controller

The power calculation model is shown on Fig. 4.2 implementing the P and Q equations established in mathematical modeling.

4.3 Frequency and Voltage Droop

The droop control law is implemented in MATLAB/Simulink as a purely algebraic signal processing stage operating on the filtered active and reactive power measurements produced by the preceding low-pass filter blocks. As established in the mathematical modelling, the active power droop relationship computes the output frequency reference $f$as a deviation from the nominal frequency f_n, proportional to the error between the filtered active power $P$and the active power setpoint P_o, scaled by the active droop coefficient m_p, in accordance with $f = f_n - m_p(P - P_o)$. In parallel, the reactive power droop computes the terminal voltage magnitude reference Vas a deviation from the nominal voltage V_n, proportional to the error between the filtered reactive power $Q$and the reactive power setpoint Q_o, scaled by the reactive droop coefficient m_q, in accordance with $V = V_n - m_q(Q - Q_o)$. Both relationships are realized in Simulink as static gain and summation blocks, reflecting the proportional steady-state nature of the droop law wherein no dynamic compensation or integral action is present within this stage. Consequently, the transient response characteristics of the droop controller are determined entirely by the bandwidth of the upstream measurement filter and the dynamic response of the downstream voltage and current control loops, rather than by the droop calculation itself. A model diagram of the implemented droop calculation is shown in Fig. 4.3, and the instantaneous values are fed into the internal reference generator stage.

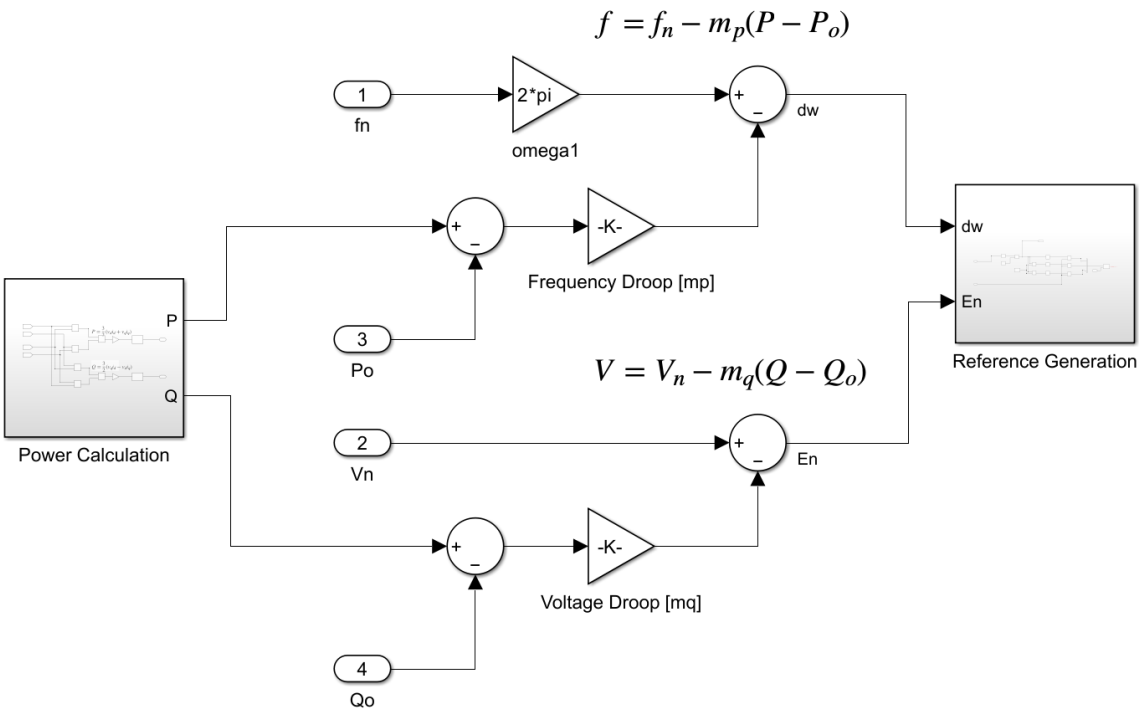


Fig. 4.3: Frequency and Voltage Droop Calculations

The selection of the active and reactive power droop coefficients m_p and m_q was informed by two complementary approaches. Eigen values analysis take carried out to determine the stable operating droop gains or active and reactive power by tracing the eigen trajectory of droop gain sweep from 0.1% to 10% droop gain.

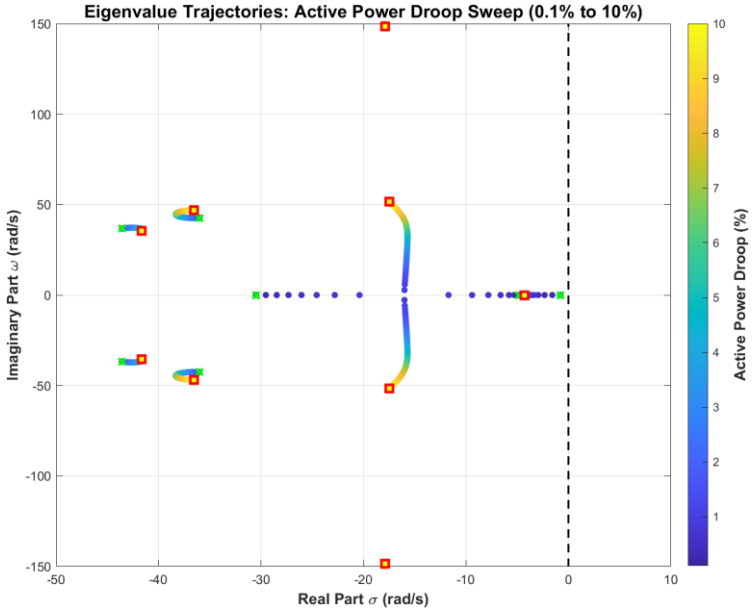


Fig. 4.4: Active Power Eigen Value Trajectory

Fig. 4.4 shows the active power eigen value trace from 0.1% to 10% with relate droop gains shown as a percentage. Fig. 4.5 shows the eigen values sweep for reactive power.

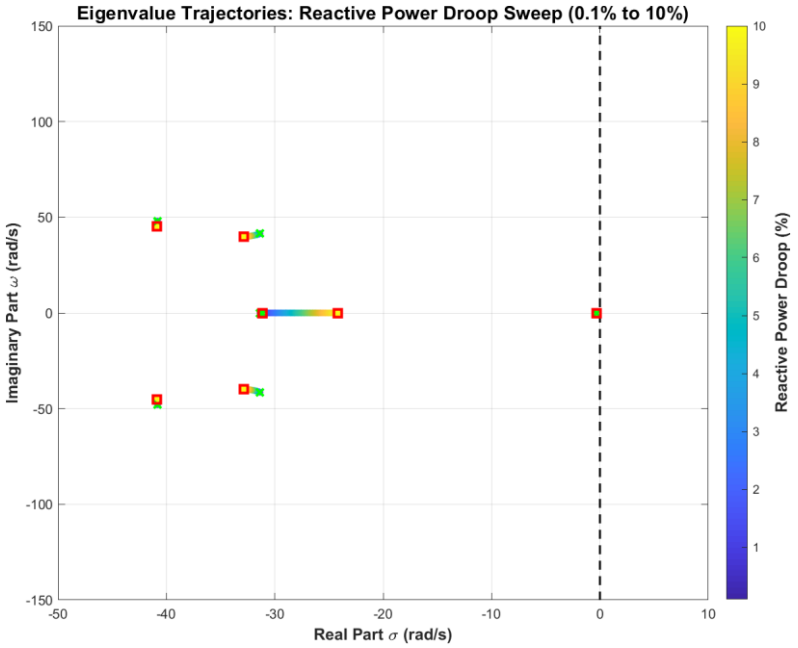


Fig. 4.5: Reactive Power Eigen Value Trajectory

The eigen values sweep analysis was carried out using inverter power, the standard grid operating parameters and the calculated LCL filter values via MATLAB script rather for

speed and accuracy over manual methods. The eigen value analysis shows that the selected droop gains can operate within stability region and combined with standard industry practice [66][67] droop gains of 1% frequency and 5% voltage were implemented in the design, and the selected droop parameters were analyzed for stability.

Active Power Droop — Frequency

$$m_p = \frac{\Delta f_{max}}{P_{rated}} = \frac{f_n \times \%_{droop}}{P_{rated}} \tag{4.1}$$

For a 1% frequency droop at 100 kW rated, 50 Hz nominal applied to (4.1) yields (4.2):

$$m_p = \frac{0.01 \times 50}{100 \times 10^3} = \frac{0.5}{100{,}000} = 5 \times 10^{-6} \text{ Hz/W} \tag{4.2}$$

Converting to rad/s per watt yields the result given by (4.3):

$$m_p = 5 \times 10^{-6} \times 2\pi = 31.416 \times 10^{-6} \text{ rad/s/W} \tag{4.3}$$

Reactive Power Droop — Voltage

For a 5% voltage droop at rated reactive power $Q_{rated} = 43.6$ kVAr (this reactive power value reflects max load at 0.9 power factor), assuming $V_n = 1.0$pu is given by (4.4):

$$m_q = \frac{0.05 \times V_n}{Q_{rated}} = \frac{0.05}{43.6 \times 10^3} = 1.147 \times 10^{-6} \text{ V/VAR} \tag{4.4}$$

The dominant pole pair is given by complex notation (4.5):

$$s = -716.472 \pm j181.876 \tag{4.5}$$

Undamped natural frequency equation (4.6) yields the result (4.7) by using the dominant pole pair result:

$$\omega_n = \sqrt{\sigma^2 + \omega_d^2} = \sqrt{716.472^2 + 181.876^2} \tag{4.6}$$

$$\omega_n = 739.14 \text{ rad/s} \tag{4.7}$$

Damping ratio given by equation (4.8) yields the stability margin given by (4.9):

$$\zeta = \frac{\sigma}{\omega_n} = \frac{716.472}{739.14} = 0.9693 \tag{4.8}$$

$$\text{Stability margin} = \frac{\sigma}{\omega_n} \times 100 = \zeta \times 100 = 96.93\% \tag{4.9}$$

Damped natural frequency is given by the equation (4.10):

$$f_d = \frac{\omega_d}{2\pi} = \frac{181.876}{2\pi} = 28.95 \text{ Hz} \tag{4.10}$$

The system is damped with a high stability margin and will exhibit minimal overshoot in transient response and oscillation components will decay rapidly at 28.95 Hz. The systems will operate inside stability margin.

Table 4.1: Droop Gain Coefficients

Key Parameter	Droop Gain Coefficients		
	Description	Value	Units
m_p	Frequency Droop Gain	1	%
m_q	Voltage Droop Gain	5	%

4.4 Reference Signal Generation

The reference generation block receives two instantaneous signals directly from the droop calculation stage and transforms these into the voltage reference signals required by the downstream voltage control loop. The angular frequency $\omega^*$is integrated with respect to time to produce the instantaneous voltage phase angle $\theta^* = \int \omega^* \, dt$, which defines the rotating dq reference frame for all subsequent inner loop computations. This integration is the mechanism by which the droop-controlled inverter establishes its output voltage phasor autonomously without requiring an external phase reference such as a phase-locked loop, and it is this property that classifies the implementation as a grid-forming control architecture. The resulting references are passed to the voltage control loop, which regulates the LCL filter capacitor voltage to track these references through the cascaded PI control structure described in the following section. Fig. 4.6 show the implementation of three phase signal generated internal references.

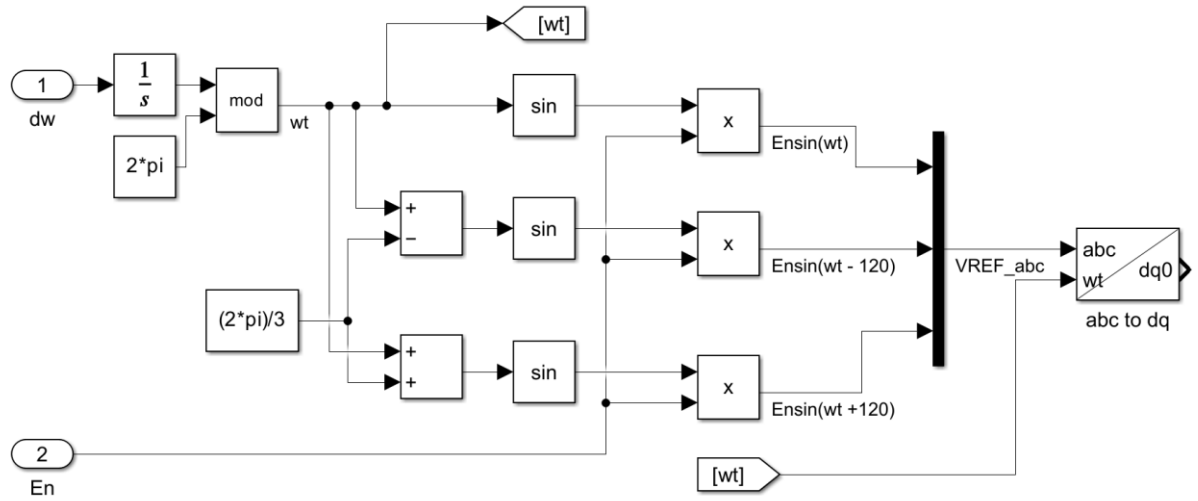


Fig. 4.6: Internal Reference Signal Generation

4.5 Outer Voltage Control Loop

The primary purpose of the voltage control loop is to regulate the inverter's terminal voltage or filter capacitor voltage, ensuring it precisely tracks the reference voltage vector generated by the outer droop and reference generation stages. Operating on a faster time scale than the power loops, it synthesizes the inner current references required to reject local load disturbances, parameter variations, and grid-induced voltage fluctuations. In terms of operation, the loop processes the error between the reference voltage and the measured feedback voltage through a high-bandwidth controller like a Proportional-Integral (PI) controller in a synchronous rotating DQ reference frame. By generating decoupled current commands, this loop dynamically shapes the system's output impedance and maintains voltage waveform fidelity under both balanced and unbalanced load conditions.

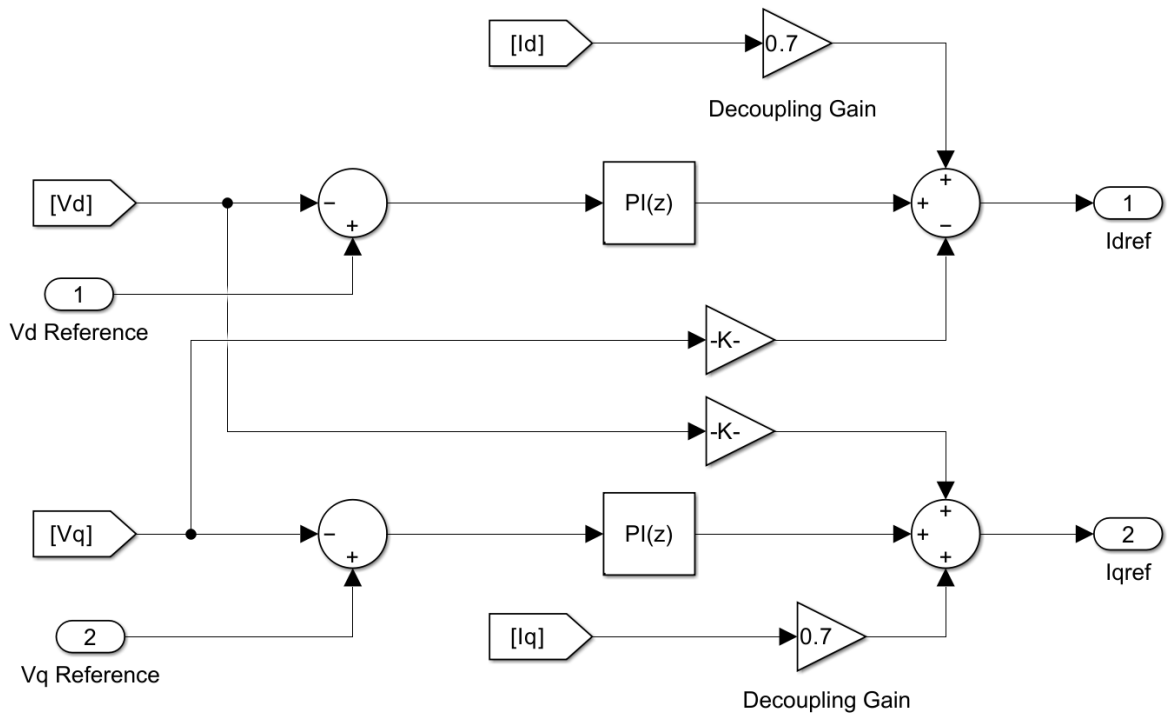


Fig. 4.7: Outer Voltage Control Loop

The outer voltage control loop implemented as shown on Fig. 4.7, takes the calculated instantaneous DQ components of capacitor voltage and the internal reference signal and produces the current reference that will determine to charge or discharge the LCL capacitor. In this method the voltage control loop manages the capacitive reactance of the feedback capacitor to maintain the grid side voltage. The current cross coupling is decoupled with a gain block to simplify the implementation and added as feed forward terms to the output.

4.6 Inner Current Control Loop

The current control loop serves as the innermost cascade of the control architecture, explicitly designed to regulate the actual output or inductor currents and protect the switching power electronics from overcurrent contingencies. It operates at the highest bandwidth of the multi-loop system and is designed to be an order of magnitude faster than the voltage loop. This is done to ensure rapid transient response and robust decoupling of the interconnected physical plant dynamics. Utilizing the current references derived from the outer voltage controller, it minimizes tracking error through high-gain PI while incorporating decoupling feedforward terms to neutralize cross-coupling effects and grid voltage disturbances. The resulting control action yields the precise duty ratios or modulating signals required by the SPWM stage, effectively translating outer loop power demands into physical switching actions while ensuring inherent short-circuit mitigation.

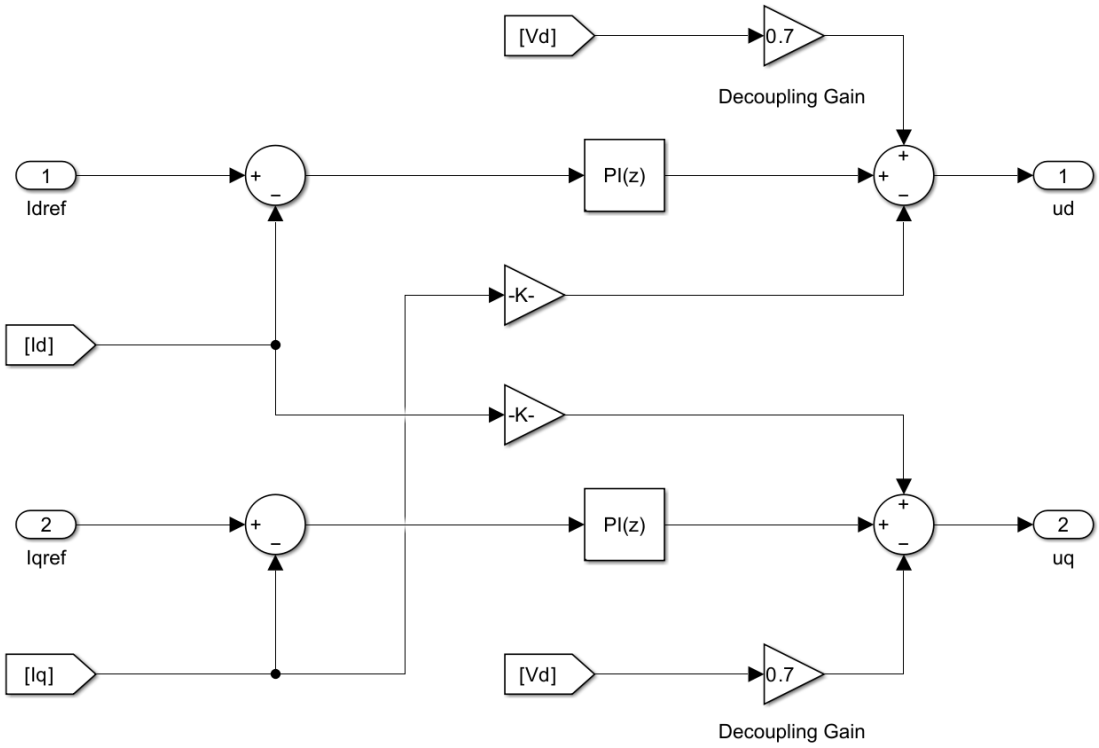


Fig. 4.8: Inner Current Control Loop

PI Controller Tuning

The PI Controllers are tuned using the MATLAB environment using a second order transfer function for the outer voltage control loop and the inner current control loop given by (4.11) and (4.12) below:

$$G_{voltage}(s) = \frac{\frac{K_{pv}}{C}s + \frac{K_{iv}}{C}}{s^2 + \frac{K_{pv}}{C}s + \frac{K_{iv}}{C}} \tag{4.11}$$

$$G_{current}(s) = \frac{\frac{K_{pc}}{L}s + \frac{K_{ic}}{L}}{s^2 + \left(\frac{R+K_{pc}}{L}\right)s + \frac{K_{ic}}{L}} \tag{4.12}$$

The terms L refers to the inductance of the inverter side inductor, and the C term refers to the feedback capacitor in the S-Domain transfer function. The equations show that the voltage control loop manages the capacitive reactance of the capacitor of the LCL filter by measuring the measures the capacitor voltage, compares it to the reference, and calculates exactly how much current is needed to charge or discharge the LCL capacitor to maintain that voltage. The current controller will manage the inductive reactance of the inverter side inductor of the LCL filter by directly controlling the PWM output which generates current flow to the feedback capacitor and out of the LCL filter [68] [69]. The final tuned parameters for voltage and current control loops can be seen in Table. 4.2. The parameters were tuned using MATLAB PID Tuner and the high-speed current loop gain were kept higher than the low-speed voltage loop gains for bandwidth separation.

Table 4.2: PI Controller Tuned Parameters

Key Parameter	Droop Gain Coefficients	
	Description	Value
K_{pv}	Voltage Loop P Gain	0.1
K_{iv}	Voltage Loop I Gain	100
K_{pc}	Current Loop P Gain	30.1
K_{ic}	Current Loop I Gain	300

4.7 IGBT Gate Driver

The current control references, the grid voltage angular frequency are converted back to abc signals and used as input to the IGBT pulse generator as shown in Fig. 4.9, the SPWM discussed in chapter 3.3 is used to generate the gate driver signal for the inverter.

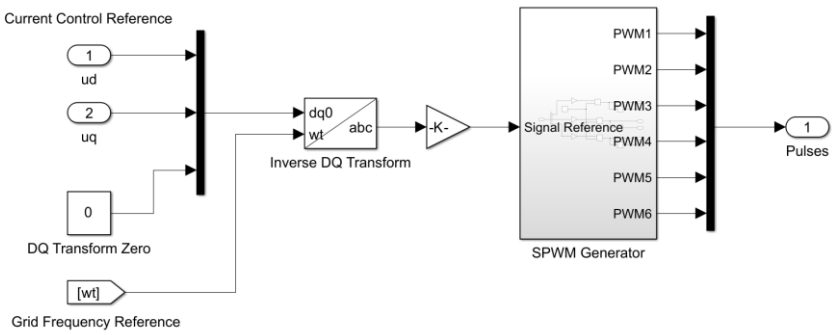


Fig. 4.9: Current Control – SPWM Interface

4.8 Grid Forming Inverter Base Resource

The integration of all the major components discussed in chapter 3 and chapter 4 complete the implemented GFM IBR designed for this research. The architecture of design can be seen in Fig. 4.10, which illustrates the control flow of signal and power through the system.

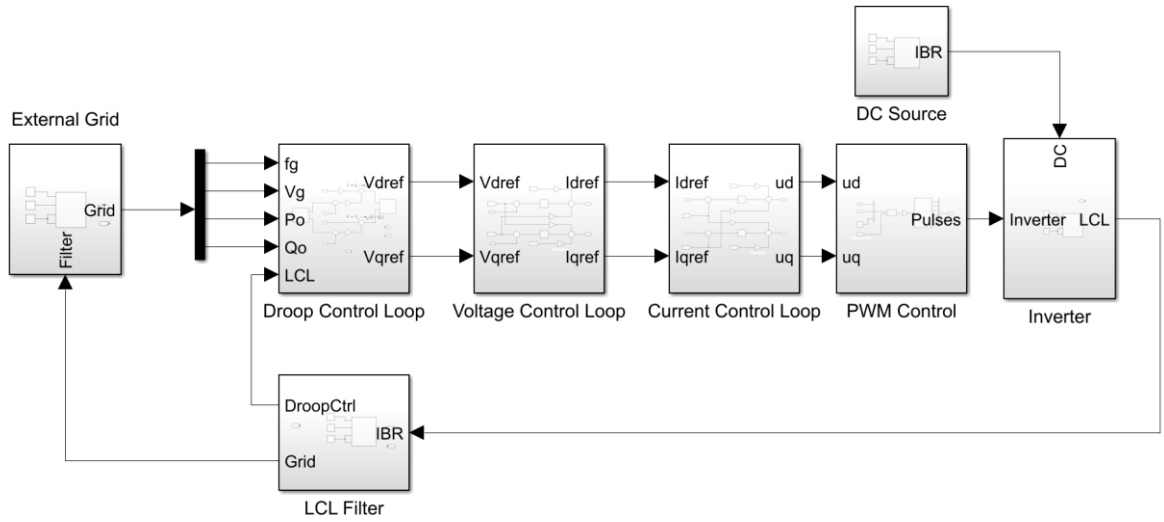


Fig. 4.10: Implemented Droop Control IBR Design

In summary, this chapter has established a comprehensive multi-loop droop control framework for the grid-forming inverter, sequentially integrating the slow-dynamics active and reactive power sharing loops with high-bandwidth, cascaded voltage and current controllers. By systematically parameterizing the internal plant dynamics and decoupling terms, the implemented design theoretically guarantees structural stability and transient voltage fidelity under nominal operating conditions. However, verifying the robustness of these controller parameters against non-linear network dynamics, sudden load variations, and severe grid contingencies requires rigorous empirical or high-fidelity simulation analysis. Consequently, chapter 5 transitions from theoretical synthesis to operational validation, presenting a series of targeted runtime scenarios designed to stress-test the inverter's dynamic response, fault ride-through capabilities, and autonomous power-sharing performance under diverse and adverse grid scenarios.

5 Grid Integration of GFM IBR

This chapter takes the implemented GFM IBR design established in the previous two chapters and connects it to a series of switchable loads and the wider grid in order to demonstrate the system performance in the following chapter. It outlines the microgrid architecture and the loads that connect to it and also integrates fault injection characteristics to the network model in order to define the islanded and grid connected test scenarios for the single IBR configuration. The multi-IBR configurations on a distribution network utilizes the IEEE 33 Bus System to study the effects of distributed placement of IBRs on a radial distribution network and the subsequent voltage profile effects. The trend towards IBRs in general are designed as stand in replacement of fossil fuel synchronous generation, in the network context the terms single machine and multi machine will used interchangeably with synchronous generation on the wider electrical grid, viewing them as energy resources. In the context of placement of GFM IBRs on the distribution networks the term distributed energy resource or DER will be used to refer to either a single machine or multi machine topology.

5.1 SMIB Connected System

The microgrid design consists of the GFM IBR, the wider grid as an ideal grid source and switchable loads as shown in Fig. 5.1, with three phase short circuit fault elements integrated into the Simulink model in a single machine infinite bus (SMIB) connected system.

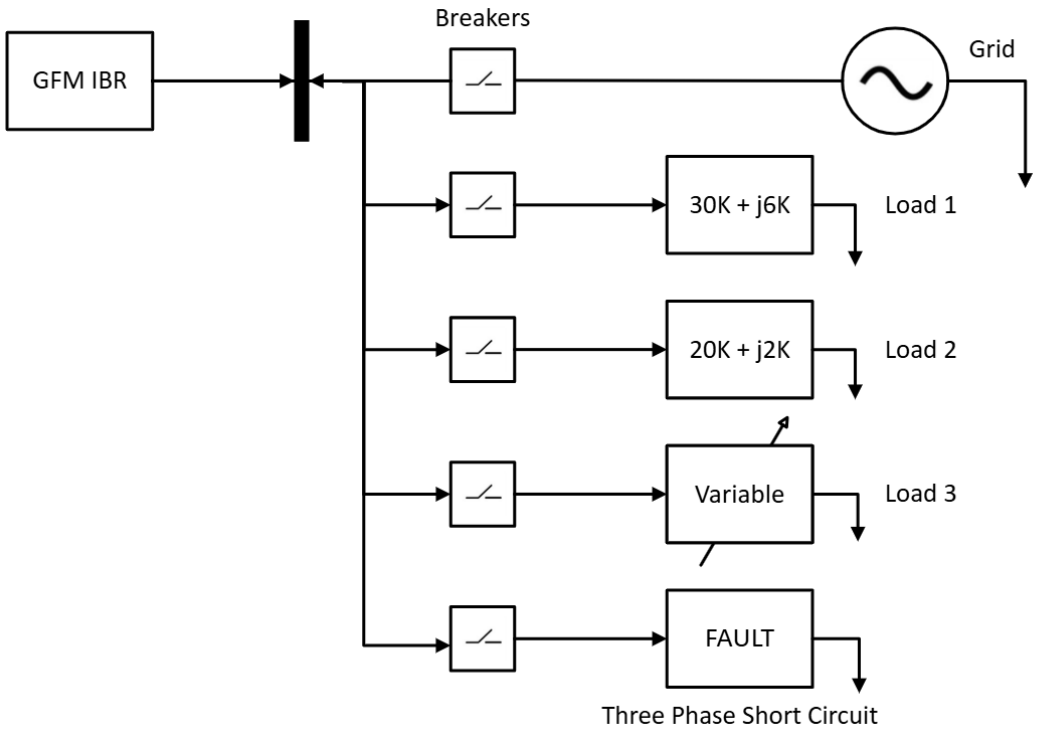


Fig. 5.1: Microgrid Topology

The loads are intended to simulate 20% and 30% of rated inverter power for combined operational load and the variable load is designed to simulate additional switchable load capacity such as inverter rated full load conditions. Fault conditions in this design simulate a three-phase short circuit fault which represents the most extreme case of grid disturbance. This fault integration is designed to simulate voltage ride through capabilities in accordance with the New Zealand grid code [64, Fig. 8.1]

5.2 Radial Distribution Network Connection

The 100kW utility scale GFM IBR represents the category of inverters that would be deployed on a radial distribution network. These networks topologies are characterized by a tree-like architecture where power flows unidirectionally from a centralized substation branching feeder lines to downstream end users. This topology requires the GFM inverter to support the network without assistance of other PV busses as is the case with ring or other topologies and requires greater voltage and frequency support.

The radial distribution network implemented for this research was the IEEE 33 Bus System that allowed for connection of single and multiple machine DER topologies in order to evaluate the multiple IBR interconnect and the ability of the IBRs to improve local system strength at the absolute weakest points of the network such as Bus 18 in the case of the IEEE 33 Bus network.

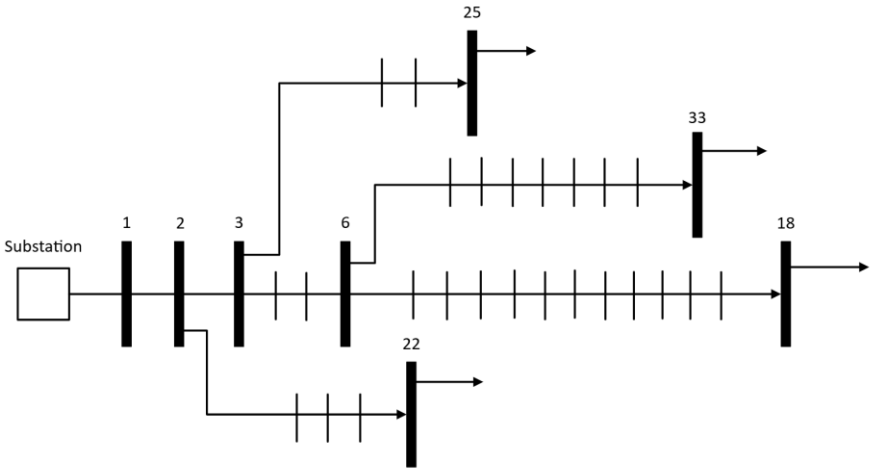


Fig. 5.2: IEEE 33 Bus System – Radial Distribution

The IEEE 33 Bus System as shown on Fig. 5.2 highlights the tail end buses, namely bus 18, bus 33, bus 25 and bus 22 in order increasing cumulative impedance and resistive and reactive power loss along the feeder length.

The voltage profile of a radial distribution network characteristically exhibits a monotonic decline from the substation bus, where voltage is held at or near 1.0 pu, toward the terminal nodes at the far ends of the feeders and laterals. Distribution systems are

becoming large and being stretched too far, leading to higher system losses and poor voltage regulation, and under certain critical loading conditions voltage instability becomes a key concern at downstream nodes. Radial distribution systems are highly susceptible to voltage instability under critical loading conditions, where even minor load increases can trigger voltage collapse, threatening the continuity and quality of power supply.

Placing GFM IBRs at the tail ends of a radial distribution network directly addresses the most severe voltage deficiency points in the system by injecting both active and reactive power at the locations of greatest need. A GFM IBR is expected to operate stably in grids with low system strength and to improve network strength in the region of connection by reducing the sensitivity of voltage to current injection and reducing the rate of change of frequency during an event which for the network as a whole, this translates into a flatter, more uniform voltage profile across all buses leading to a reduced risk of voltage collapse at remote nodes, lower feeder losses, and an increase in the effective short circuit ratio, enhancing both steady-state power quality and dynamic resilience.

The IEEE 33 Bus System provides a useful platform for conducting such studies and was implemented to investigate the effects on steady state voltage profile improvement for the 33 Bus System. A comprehensive study of the full effects of transient dynamics and grid impact will also require modelling of a realistic grid rather than the ideal grid used in this research is beyond the scope of this thesis and is suitable for future research. This research looks at steady state network performance of GFM IBRs in DER configurations to systematically evaluate the viability of the implemented system to provide power to a microgrid and maintain stable connection to the wider electrical grid.

The 100kW system on the other hand was designed to operate at the microgrid 400V system directly providing power to the end consumer. The IEEE 33 Bus system operated at 12.66kV and required modelling of a substation layer to step the voltage up to make the system compatible with the 33 Bus network. This is shown on Fig. 5.3 illustrates how the 400V output of GFM IBR is stepped up to 12.66kV to connect to a bus on the 33 Bus network.

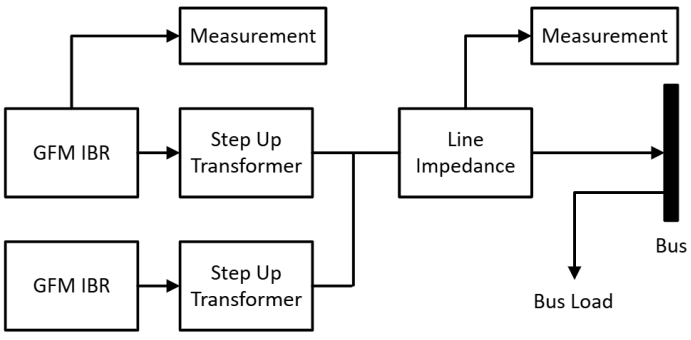


Fig. 5.3: Multi-IBR Connection on Radial Network

5.3 Autonomous Power Sharing

The IBR placement on the IEEE 33 Bus System followed the placement strategy that look at the tail end of the distribution network with Bus 18 identified the furthest bus from the local substation slack bus therefore was selected for testing the capability of the implemented system in this research to be able to connect to the network and improve the network power quality characterized by the voltage profile of the network.

A baseline voltage profile was established for the IEEE 33 Bus System with no inverters connected. Then the droop-controlled inverters were systematically connected to the network such that the combined power capacity and power quality of the network was improved measured against the voltage profile of the network. This extension is not designed as a comprehensive study of the effects of grid side dynamics; it can however serve as the testbed for stress testing the inverter side dynamics of the implemented system with the goal of assessing variability for physical development and deployment on a real power grid. A droop-controlled GFM IBR does not rely on communication layer for coordination and power sharing has been established in the literature so the aim to demonstrate the autonomous power sharing in a distributed system and present and analysis of the associated challenges and limitations addressed in this thesis directly and provide scope for future research.

The GFM IBR Placement Strategy used is described as following:

The 33 Bus network with a single IBR connected to Bus 18 is shown in Fig. 5.4 and this demonstrates the limited ability of a single 100kW utility scale inverter to make a significant impact on the voltage profile.

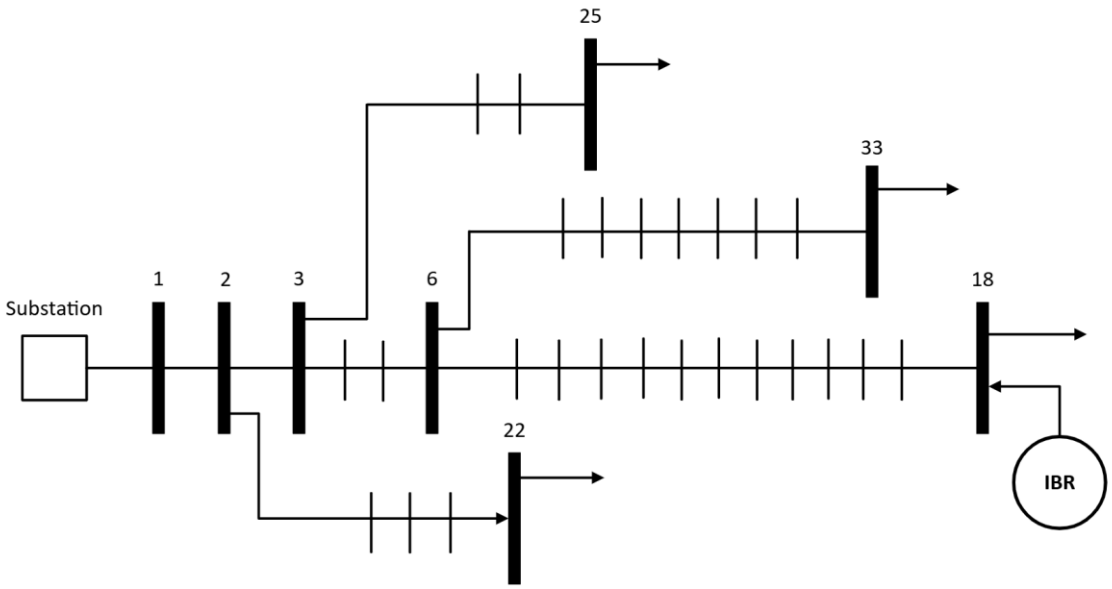


Fig. 5.4: IEEE 33 Bus – Single IBR Single Bus Connection

The 33 Bus network with a multiple interconnected IBR connected to Bus 18 is shown in Fig. 5.5 and this demonstrates the improved ability for multiple inverters to make a significant impact on the voltage profile of a distributed network. This is done to emulate the most probable real word scenarios where multi-inverter commercial rooftop solar configuration connects to a distribution network.

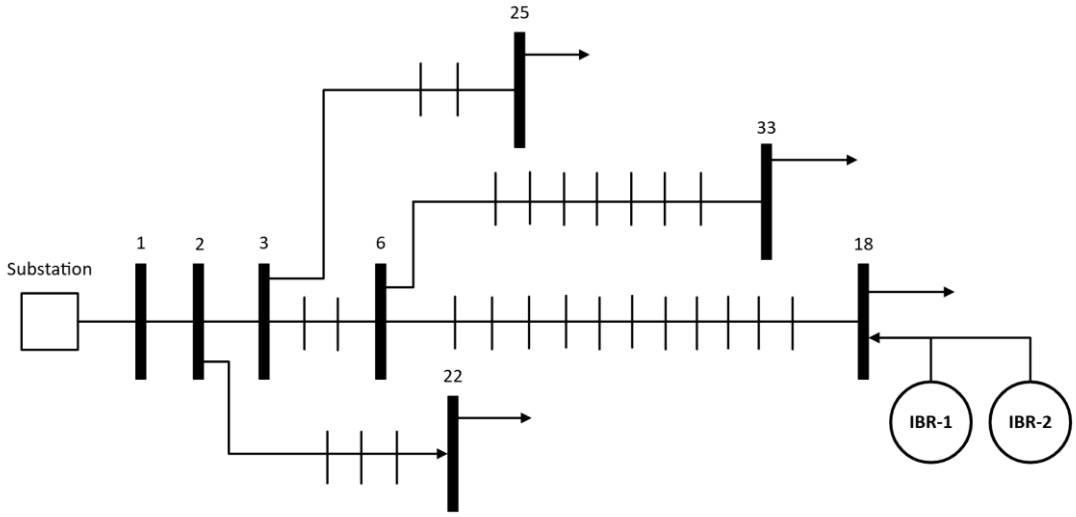


Fig. 5.5: IEEE 33 Bus – Multiple IBR Single Bus Connection

The 33 Bus network with a multiple IBR configuration to form a high penetration of DERs on a radial network. The Fig. 5.6 shows a network of GFM IBRs scaled up to 600kW each connected to the tail end of the 33 Bus network.

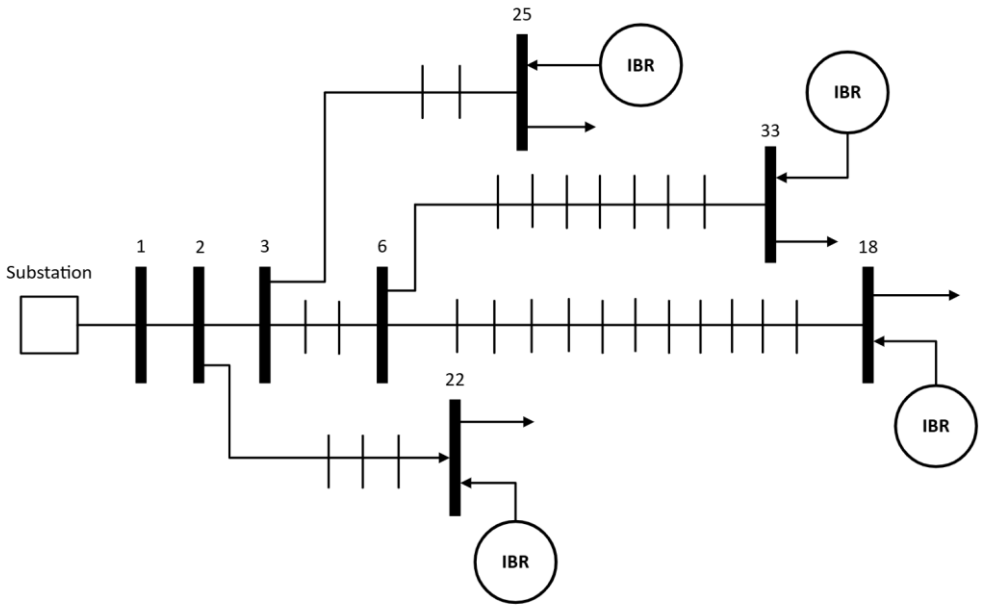


Fig. 5.6: IEEE 33 Bus – Multiple IBR Based DER

5.4 Methodological Summary

This methodology established in chapter 3, 4 and 5 forms the basis for the research outcomes presented in the next chapter where the HIL validation simulation results are presented together with the core implications of the results. In order to validate the operational efficacy and scaling dynamics of the proposed control architecture, a comprehensive end-to-end verification framework was executed across three distinct operational paradigms, utilizing a high-fidelity photovoltaic supplied, BESS backed GFM inverter topology. The core methodology transitions systematically from local asset dynamics to macro-level network coordination.

First, the ability for the implemented droop controlled GFM IBR to provide frequency and voltage regulation under grid load and fault conditions were evaluated under both grid-connected and islanded microgrid transitions to guarantee autonomous frequency and voltage reference generation without reliance on a legacy slack bus.

Second, to bridge the gap between idealized single unit models and physical network realities, the integrated IBR components including the primary PV DC-link dynamics, SPWM modulation, and an optimized LCL harmonic filter. Finally, the localized control topology was scaled and deployed within a modified IEEE 33-bus radial distribution network, where a distributed multi-bus allocation framework was implemented to systematically optimize the feeder's global voltage profile. The quantitative outcomes, transient waveforms, and systemic stability metrics resulting from this multi-tiered implementation and validation are detailed in the following chapter.

6 Simulation Results and HIL Validation

This chapter presents the core empirical findings of this thesis together with the HIL validation protocol applied to the simulation modelling that was developed in the preceding chapters.

6.1 HIL Configuration

The integration of the simulation model components within the HIL platform required adapting the model with the necessary discretized parameters as defined in the OPAL-RT HIL platform manuals [70]. The implemented GFM IBR Simulink model is compiled withing the RT-LAB software environment and the resulting output is used to emulate the inverter synthesized for the FPGA on the OPAL-RT hardware platform. The digital storage oscilloscope (DSO) channels output scaled down signals from the emulated hardware such as voltage and current waveforms. In order to capture these signals correctly the system and avoid saturating of the measurement the Simulink model must be scaled down accordingly since the hardware emulation will not operate at grid voltages and currents gain blocks must be added and termination blocks for the measurement reference. Fig 6.1 shows the HIL configuration and basic flow of signals.

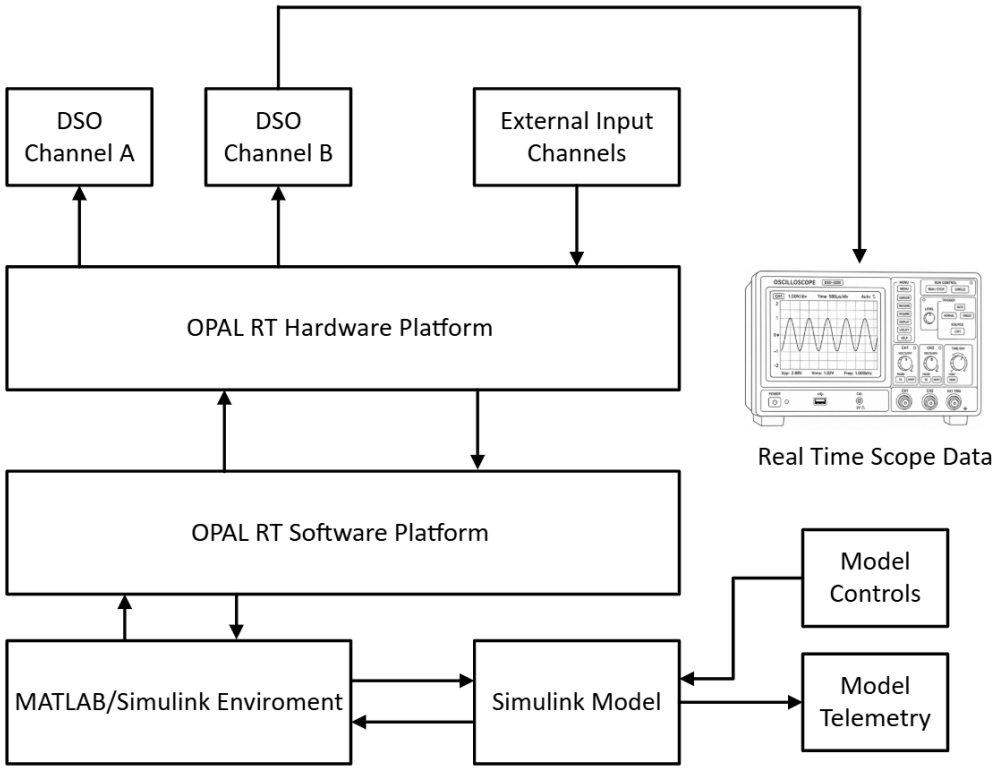


Fig. 6.1: HIL Configuration

The implemented GFM IBR model was modified to add necessary telemetry for runtime controls. Instrumentation was integrated into the final model such that experiments and

case studies could manually be developed before time intervals and event coordination could be achieved. The simulation platform was equipped with interactive, high fidelity instrument interface and although script driven inputs were implemented, solely relying on predetermined inputs proved to be time inefficient as any errors or mistimed even meant stopping a rather large process heavy end-to end simulation only to edit parameters to restart the simulation. This human in the loop (HITL) integrates real time virtual telemetry such as frequency and voltage gauges, active and reactive power monitors alongside manual runtime switches.

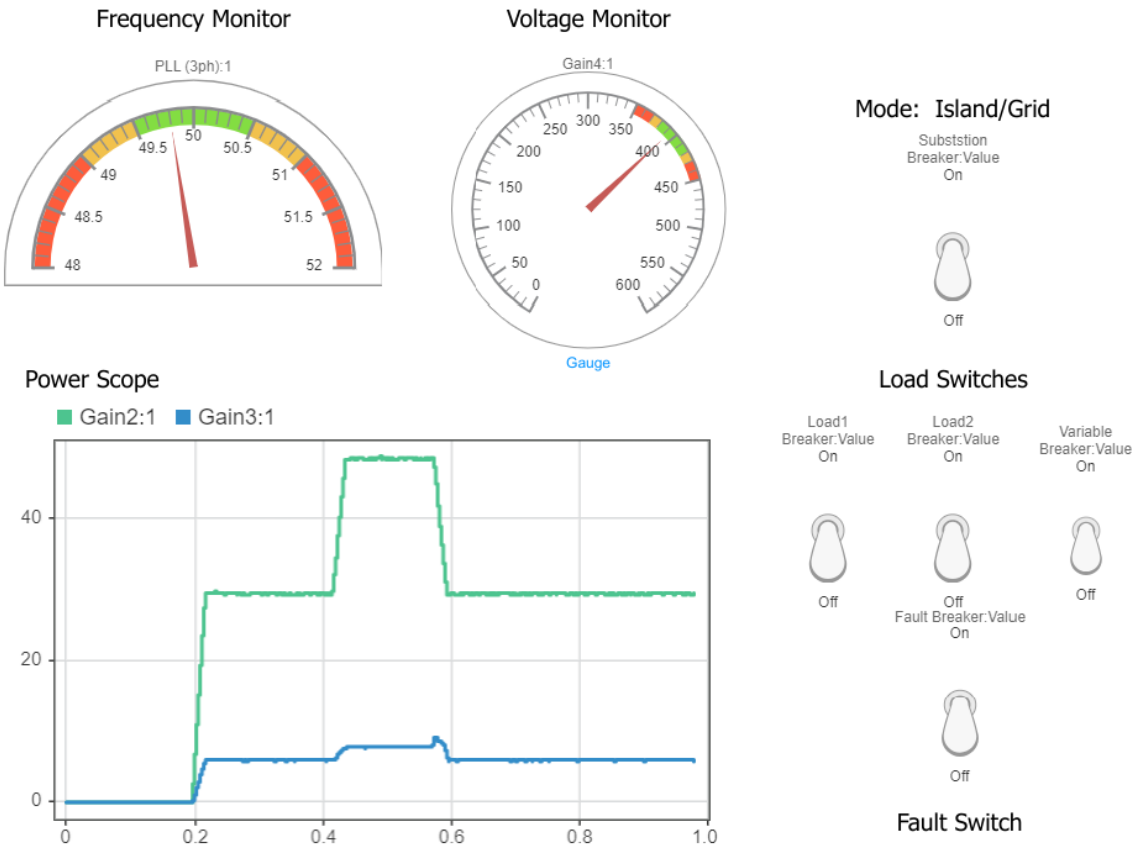


Fig. 6.2: Real Time Telemetry Integration

The real time instrument cluster can be seen on Fig. 6.2. This was used in conjunction with hardware in the loop (HIL) to maximize experimental throughput and fidelity. The HIL platform executed real time emulations of physical power electronics and network dynamics and HITL allowed for the instantaneous runtime execution of operational scenarios without needing prior sequencing in the script. This significantly expanded the achievable test coverage within a fixed development timeline that is useful for optimized use of shared resources such as HIL lab access.

The system developed in this research was designed to capture the practical constraints associated with implementing a full-scale smart inverter for a small-scale PV system. All major subsystems modelled to implement the GFM IBR were adapted to the HIL platform

to allow emulation of power electronics-level fidelity to accurately represent system dynamics.

HIL test was performed using an OPAL-RT OP5700 real-time simulator with the RT-Lab software environment. This real-time execution setup allows closed-loop interaction between the inverter controller and the simulated PV system, enabling high-fidelity evaluation of both steady-state and transient responses without the cost or risk associated with full-scale hardware deployment. Fig. 6.3 illustrates the HIL setup, including the OP5700 simulator, a DSO, and the host machine running RT-Lab software.

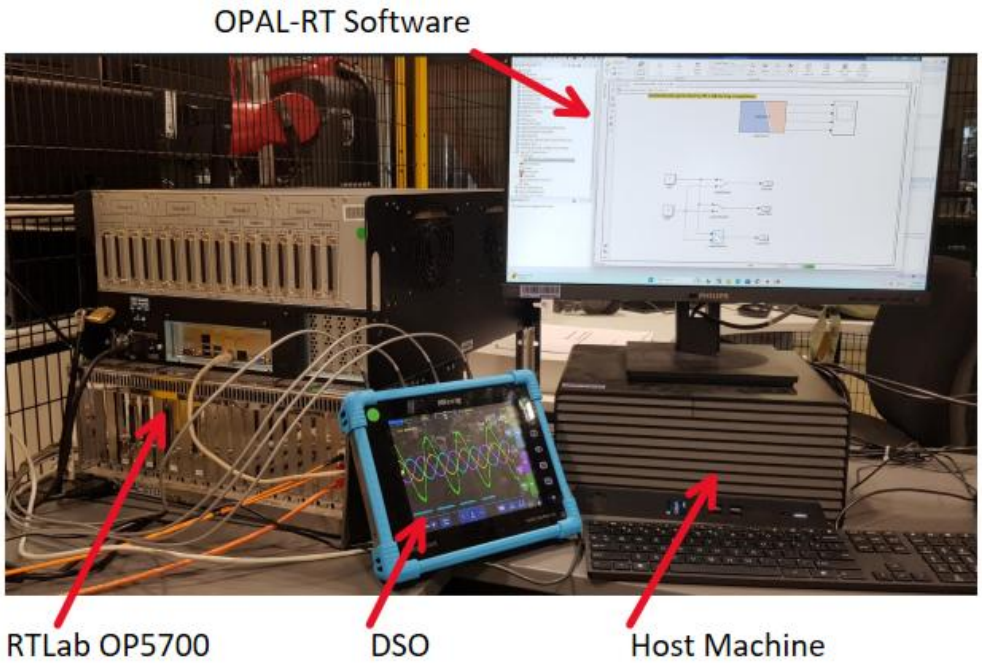


Fig. 6.3: HIL Setup of Real-time Validation

6.2 Peer Reviewed Publication

Together, the HIL validated islanded configurations, and the grid connected studies form the core operational frameworks of this research. The underlying methodology and preliminary outcomes of these configurations have been rigorously peer-reviewed and published in the proceedings of the ACPEE 2026 conference, establishing the academic and technical validity of the models presented herein.

The final case study extended the research with the inclusion of steady state performance on the IEEE 33 Bus System and demonstrated the viability of multiple vendor agnostic GFM IBR in DER configurations to operate on distribution networks with the need for external communication between individual inverter for coordination on the electrical grid. These initial system configurations and baseline dynamics form a key part of this thesis, and their extended transient profiles remain under active analysis for future publication.

6.3 Islanded Mode – HIL Validation

6.3.1 Primary Droop Response – Island Mode

The primary droop response for the captures the droop characteristics of the inverter in islanded configuration. A step change in load is applied at t = 2.0s followed by a load increase at t =4.0s, then a load decrease at t = 6.0s then no load at t = 8.0s. The results show the overall droop performance for the inverter.

Fig 6.4 illustrates a fixed load rated to draw 20kW power and 5kVar of reactive power switched on at t = 2.0s corresponds to a dip in frequency. When the load is doubled to 40 kW real and 10 kVAr reactive power, there is another frequency dip at t = 6.0s. Then when the load is halved again at t = 6.0s, there is a corresponding frequency rise. Then with no load at t = 8.0s there is another frequency rise. The same is true for the voltage characteristics, however the effect is not as pronounced as with the frequency. Further analysis will show that the frequency regulation and voltage regulations are within New Zealand code constraints as per Schedule 8 of the Electricity Participation Code [64].

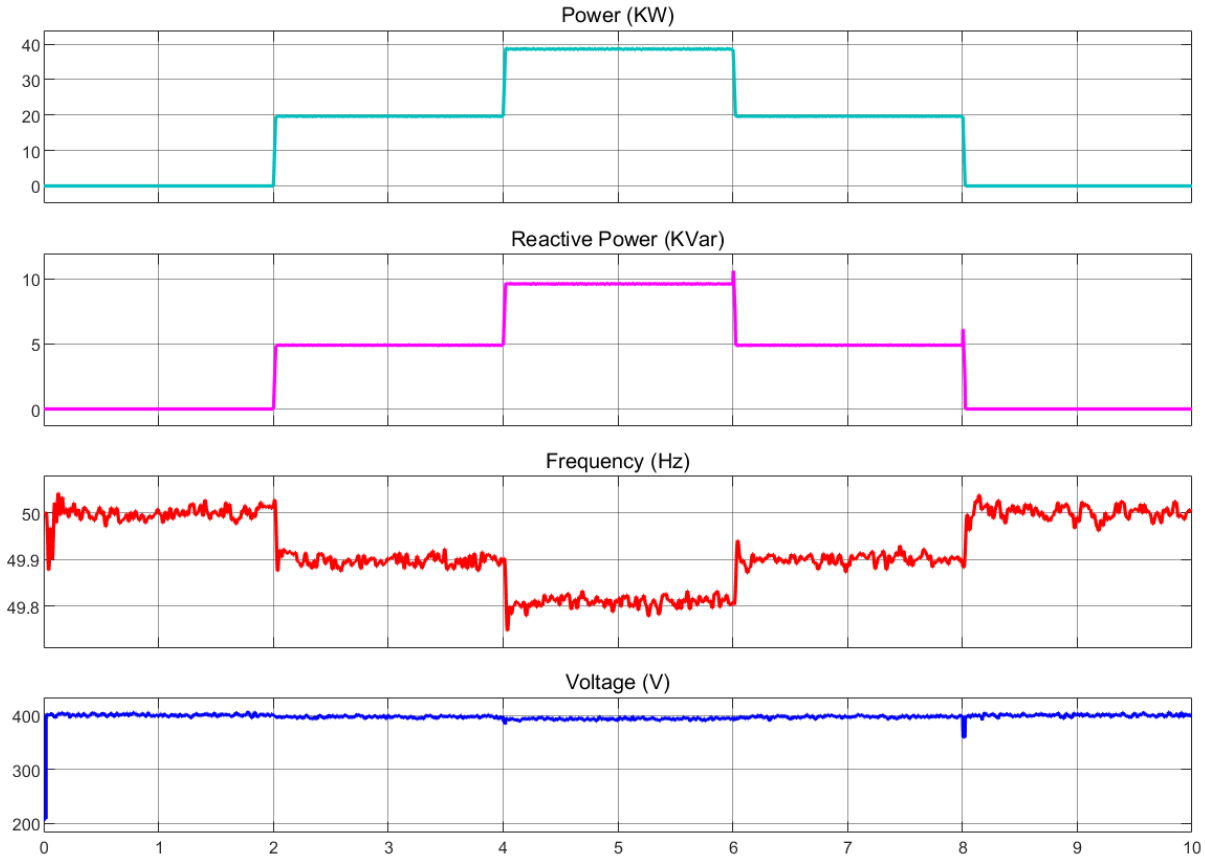


Fig. 6.4: Primary Droop Response – Islanded System

Fig 6.5 illustrates the three-phase voltage and current envelopes corresponding to the load changes that occurred to show the primary droop characteristics of the inverter from the previous figure. Its figure also shows how the droop-controlled inverter behaves as a

constant voltage source behind an impedance as established in the literature and as such load changes are characterized by the step changes in the three-phase current outline that are labelled on the figure.

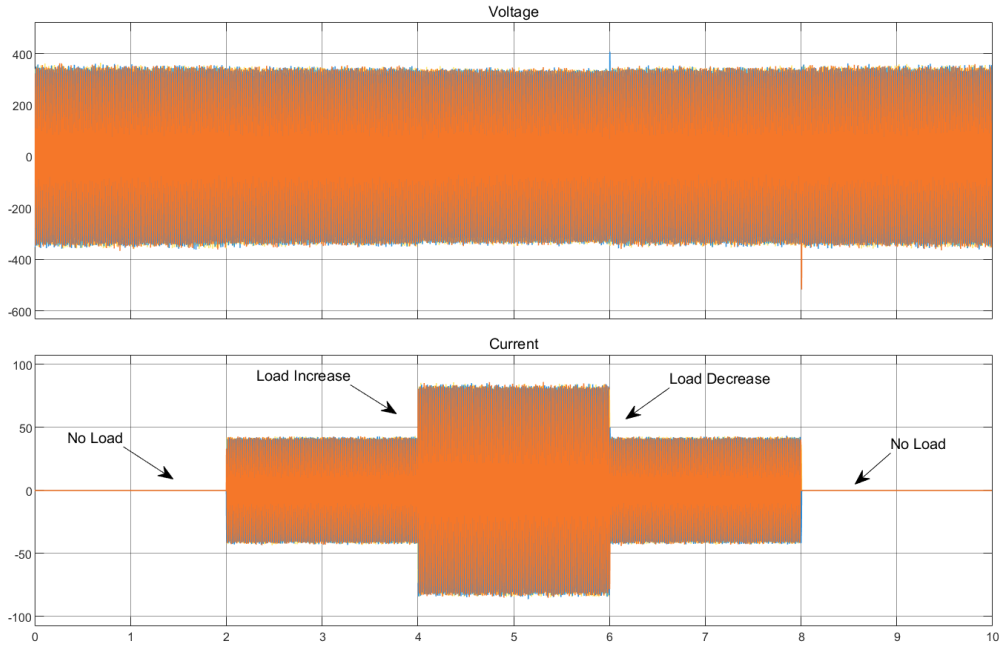


Fig. 6.5: Islanded Droop Response – Voltage and Current Envelope

Fig 6.6 illustrates the three-phase AC signals that correspond to the current envelope in response to load changes. A magnified view of a small steady state time slice is taken at ~4.5s to show the familiar alternating waveforms. The outline of the grid side inverter voltage and current is shown on the left of the figure, a small time slice of the AC signals can be seen on the right of the figure.

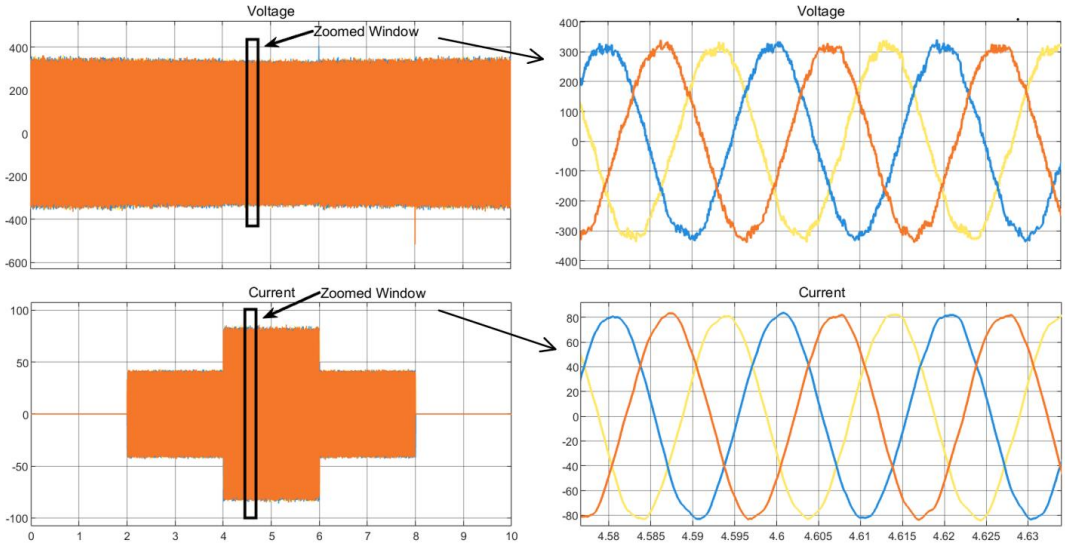


Fig. 6.6: Islanded Droop Response – Three Phase Signals

6.3.2 Steady State Response – Island Mode

In steady-state stability analysis, a step change in load was applied in islanded microgrid configurations at t = 4s. The results have been compared to the frequency and voltage requirements in New Zealand Grid Code.

Fig. 6.7 illustrates the inverter response when a load is switched on at t = 4s during islanded operation. The system exhibits a small frequency drop and a light RMS voltage dip, both characteristics of droop-controlled frequency-voltage regulation. These deviations remain well within the droop-control limits specified for autonomous operation. Following the disturbance, the inverter rapidly restores frequency to within the allowable 49.25 - 50.75 Hz and maintain RMS line voltage within ±5% of 1.0 pu, which are specified in New Zealand Grid Code. Furthermore, active and reactive power outputs rise proportionally to supply the increased load, and little oscillations and overshoot are observed. These results confirm stable frequency-voltage regulation in standalone operation.

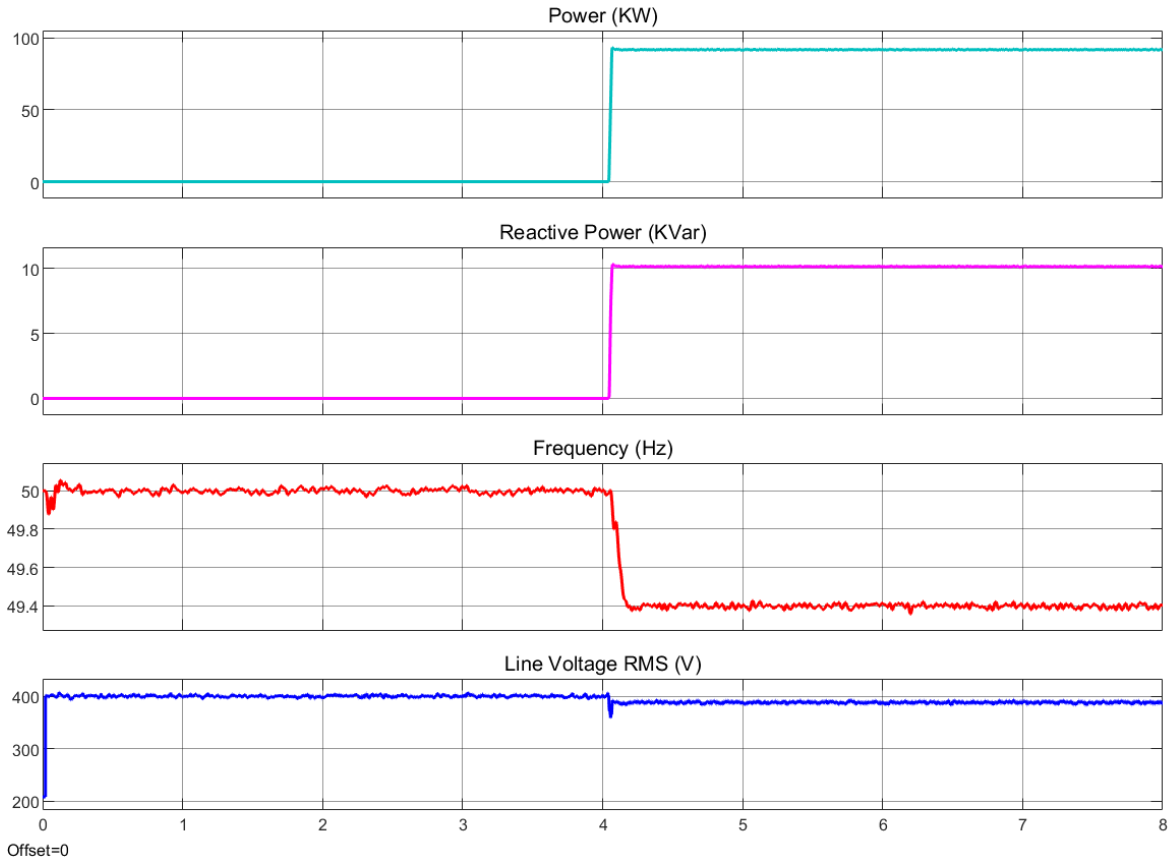


Fig. 6.7: Steady-State Response of Islanded System

6.3.3 Transient State Response – Island Mode

In transient stability analysis, a three-phase short-circuit fault was applied at PCC. The system was tested under islanded configuration. The fault was applied to the systems at t = 6s, and cleared after 0.14s which is used to meet the New Zealand grid code LVRT requirement.

Fig. 6.8 presents the islanded-mode response, showing the frequency trajectory and RMS line voltage waveform during and after the fault. When the fault is initiated, the RMS voltage collapses as expected, and the inverter reduces active power output while providing reactive support. Despite the severe disturbance, the inverter maintains stable frequency control and does not disconnect. Once the fault was cleared after 0.14s, the system exhibited full recovery within 0.5s, returning both frequency and RMS voltage to their nominal values without any load shedding. This confirms that the inverter can sustain stable autonomous opration through severe faults.

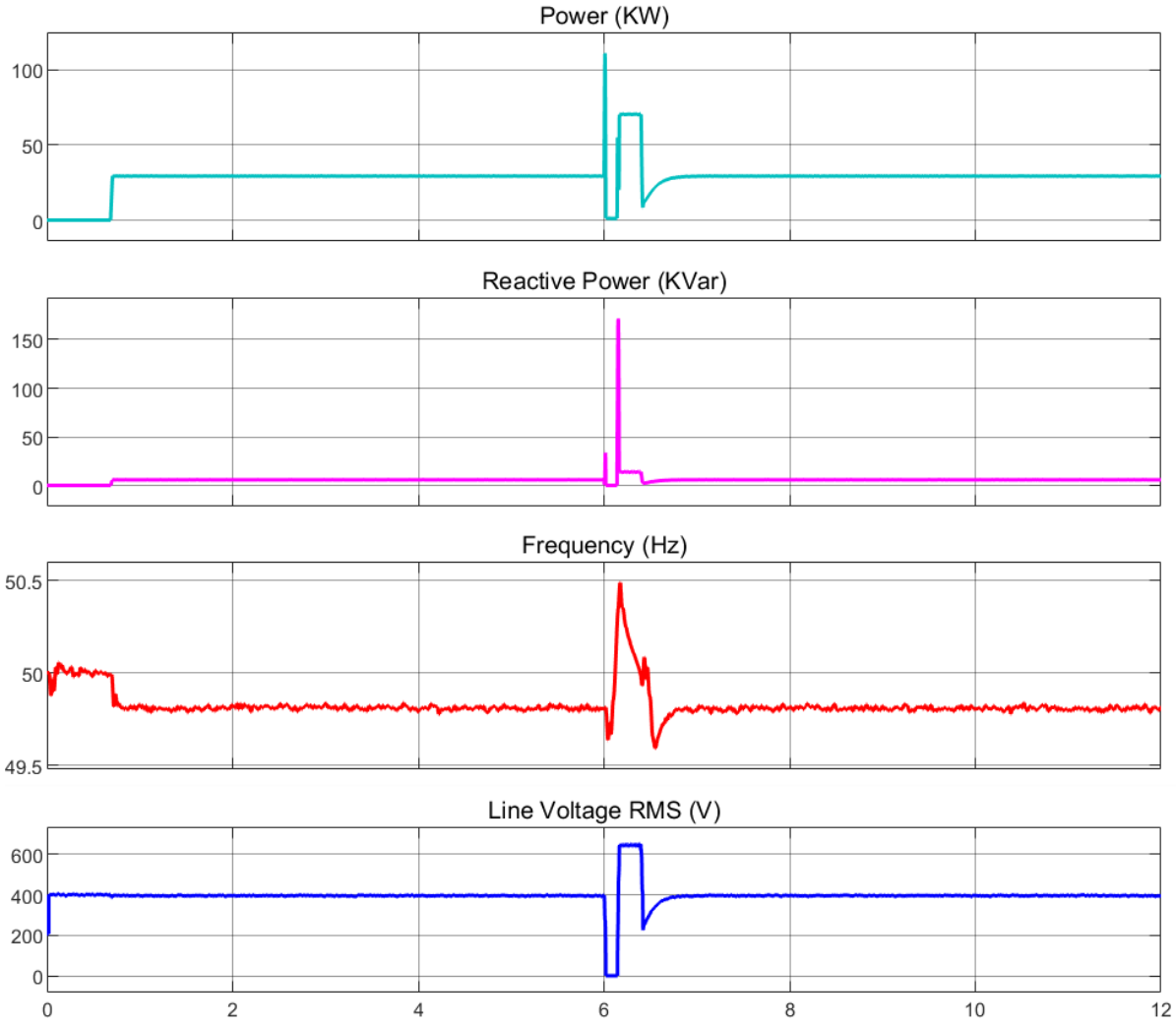


Fig. 6.8: Transient Response in Islanded System

6.4 Grid Connected Mode – HIL Validation

6.4.1 Primary Droop Response – Grid Mode

The primary droop response for the captures the droop characteristics of the inverter in grid connected configuration. A step change in load is applied at t = 3.0s followed by a load decrease at t = 6.0s. Unlike the island mode the load is shared with the grid so a single step up and step-down change in load condition is sufficient for the results show the overall droop performance for the inverter. This is done to capture the response more without compounding the effects of transients with additional load steps.

Fig 6.9 illustrates a fixed load rated to draw 20kW power and 5kVar of reactive power switched on at t = 3.0s corresponds to a dip in frequency and a very slight sag in voltage corresponding to the droop gains of 1% and 5% respectively. When the load is removed on the microgrid at t = 6.0s there is a corresponding rise in both frequency and voltage demonstrating droop-controlled regulation. In grid-connected mode, the no-load condition applies strictly to the local microgrid. Under the infinite bus assumption, the utility grid maintains its base load and nominal parameters regardless of local microgrid switching therefore the net zero power flow is purely an artifact of the simulation's localized boundary conditions. Further analysis will demonstrate grid compliance of frequency and voltage regulation required by the New Zealand grid code.

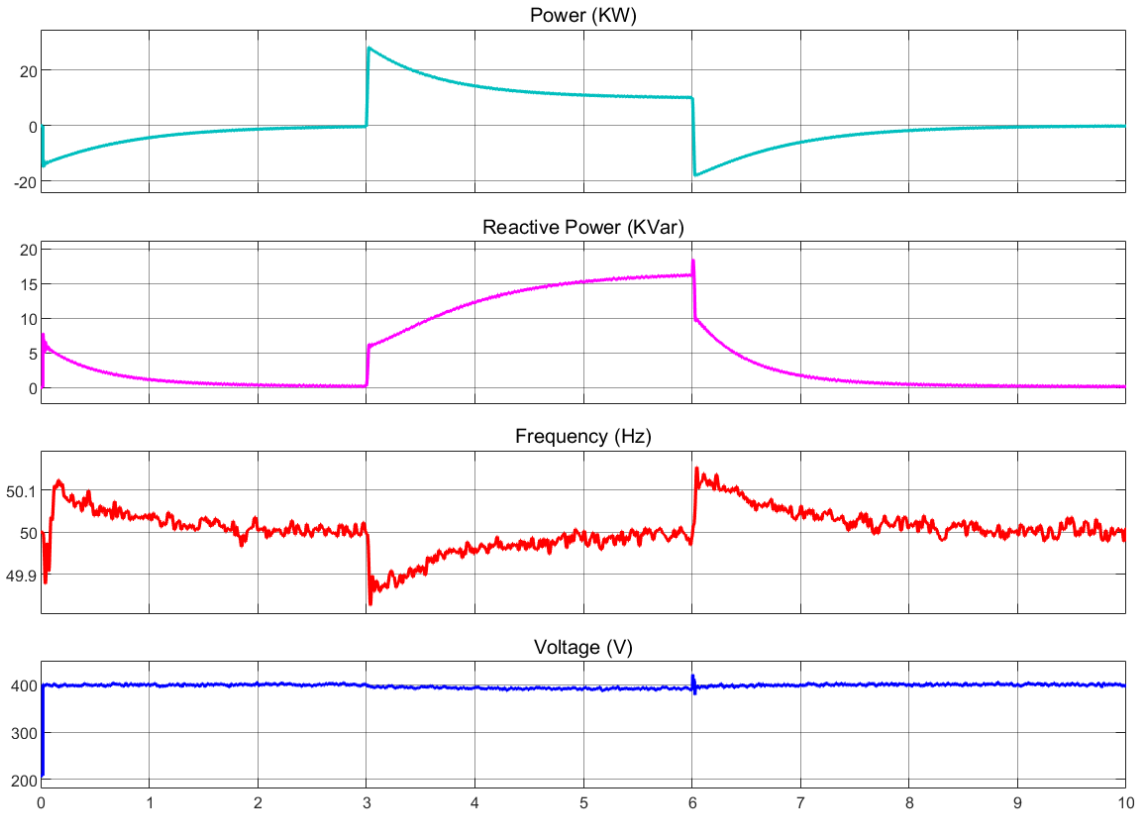


Fig. 6.9: Grid Connected Droop Response

Fig 6.10 illustrates the three-phase voltage and current envelopes corresponding to the load changes from Fig 6.9. The voltage envelope shows that the grid connect inverter behaves like a constant voltage source behind the and impedance much the same as the islanded mode from Fig 6.5. with droop-controlled voltage regulation. The current envelope shows that the additional transients associated with grid connected mode. The initial transient at t = 0.0s as some real power is absorbed back by the inverter and some reactive power is supplied by the inverter as the inverter synchronizes with the grid synchronize. This is a simulation artifact as running the simulation will inherently simulate a black start, however, the necessary protection schemes and modifications required for a high-fidelity black start capable inverter fell outside the scope of this thesis. Nevertheless, this phenomenon was anticipated during the design phase, and its impact on steady-state operation was accounted for by oversizing the DC Bus capacitors of the PV sub-system boost converter as established in chapter 3.2 and in Fig 3.9 each of the boost converter capacitor was set to four times the calculated size in Table 3.1 in order to get twice the DC Bus capacitance due to their inherent series connection. Fig 6.10 also shows transients at t = 3.0s and t = 6.0s that coincide with the step change in load which is expected of droop control inverter sharing power with and ideal grid. The droop controller is able to stabilize the system to supply steady state power from t = 4.0s to t = 6.0s and back to baseline at no load on the microgrid.

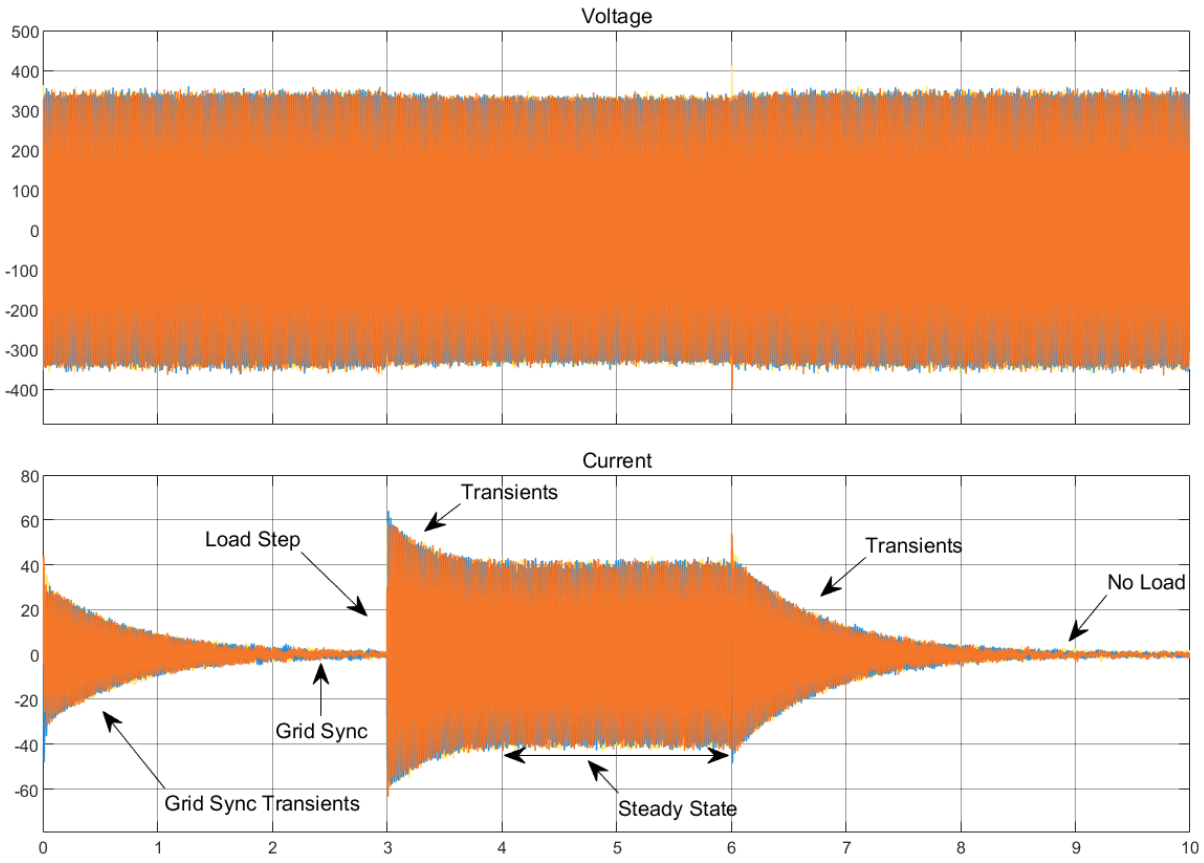


Fig. 6.10: Grid Connected Droop Response – Voltage and Current Envelopes

Fig 6.11 illustrates the three-phase AC signals that correspond to the current envelope in response to load changes. A magnified view of a small time slice is taken at ~4.0s to show the familiar alternating waveforms. The outline of the grid side inverter voltage and current is shown on the left of the figure, a small time slice of the AC signals can be seen on the right of the figure. These AC signals show a higher distortion when compared to similar steady state conditions in islanded mode on Fig 6.6, highlighting the significance of harmonic management when operating in grid connected mode. Further analysis of the harmonics of this system will be discussed in its dedicated section of this chapter.

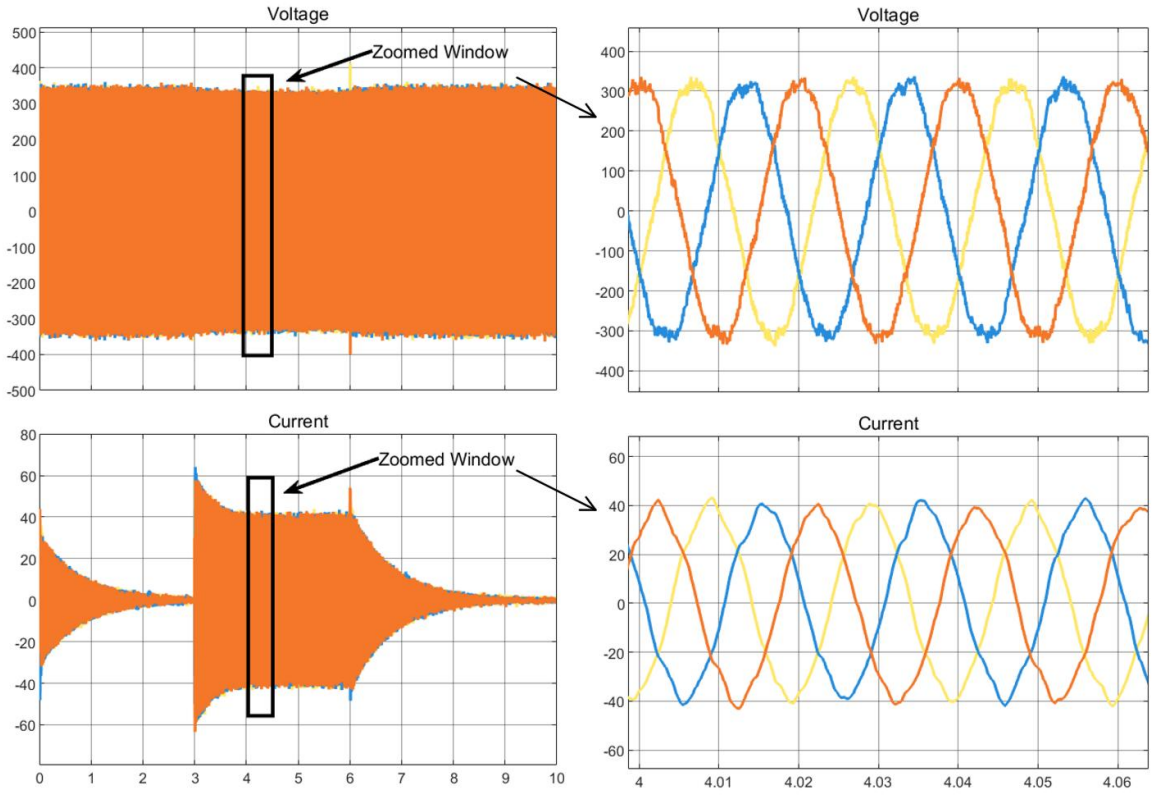


Fig. 6.11: Grid Connected Droop Response – Three Phase Signals

6.4.2 Steady State Response – Grid Mode

In steady-state stability analysis, a step change in load was applied in grid connected microgrid configurations at t = 4s. The results have been compared to the frequency and voltage requirements in New Zealand Grid Code.

Fig. 6.12 shows the corresponding response for the grid-connected configuration. When the load is applied at t = 4s, the inverter again produces the expected droop-based response, including a minor frequency dip and a small voltage deviation, both significantly damped due to the stiff grid forming the infinite bus. The inverter increases active power output smoothly and regulates reactive power to maintain voltage at PCC. Power and voltage settle quickly, demonstrating reliable disturbance rejection while synchronized to the grid.

In grid-connected steady-state conditions, frequency and voltage remain within their New Zealand Grid Code compliance envelopes.

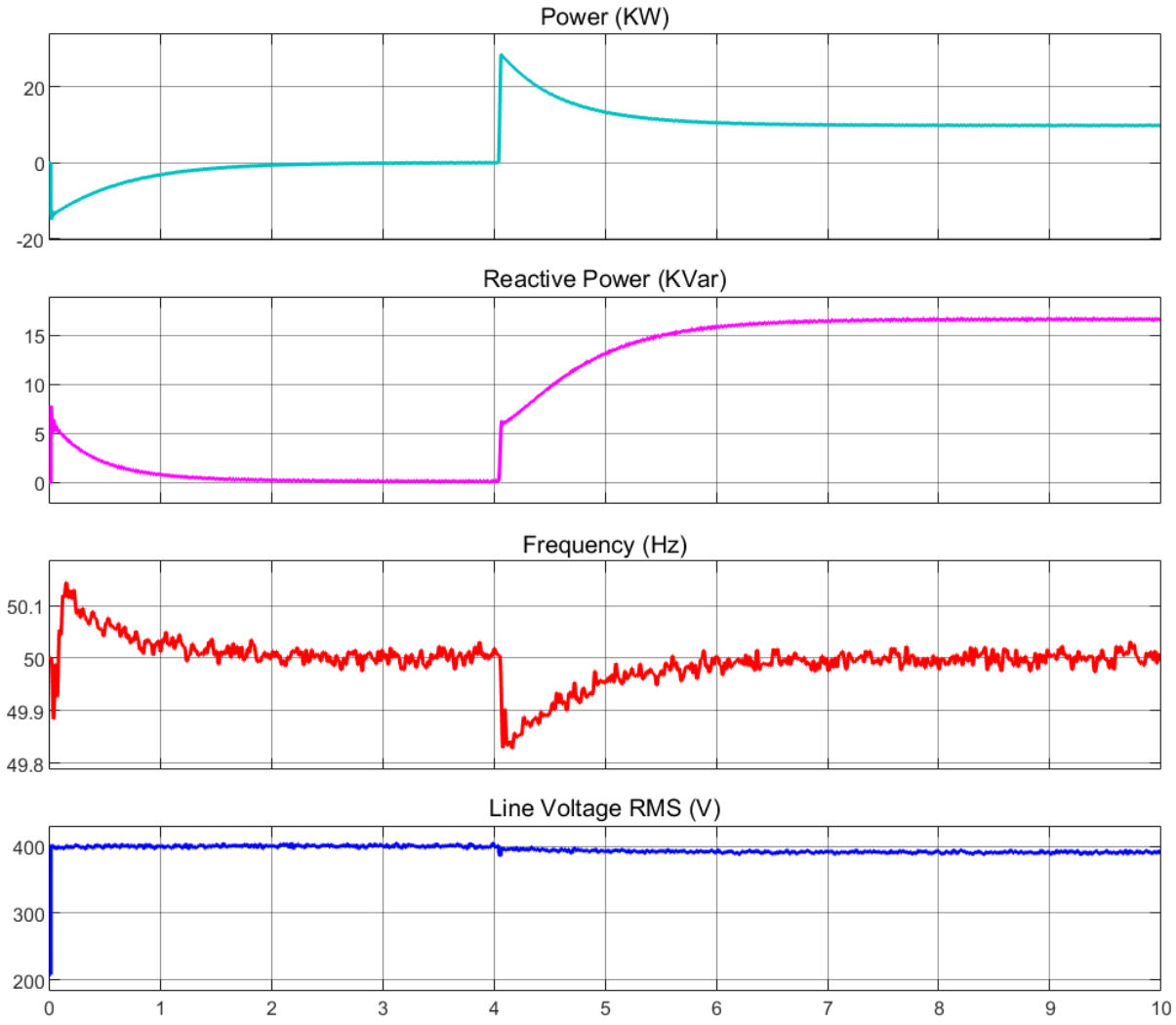


Fig. 6.12: Steady-state Response in Grid-Connected System

6.4.3 Transient State Response – Grid Mode

In transient stability analysis, a three-phase short-circuit fault was applied at PCC. The system was tested under grid connected configuration. The fault was applied to the systems at t = 6s, and cleared after 0.14s which is used to meet the New Zealand grid code LVRT requirement. The steady state load was applied from section 6.4.2 for demonstrate that the systems returns to baseline grid load after the short fault is cleared.

Fig. 6.13 shows the corresponding response in the grid-connected configuration. The stiff grid reference helps maintain synchronization, and the inverter continues to regulate voltage and reactive power during the fault. RMS voltage again collapses during the fault but recovers rapidly once the fault is cleared.

Similar to the islanded case, the system achieves complete recovery within 0.5s, with no loss of synchronism and no-load shedding. Active power and voltage return smoothly to their pre-fault levels, demonstrating strong dynamic stability under grid-side faults.

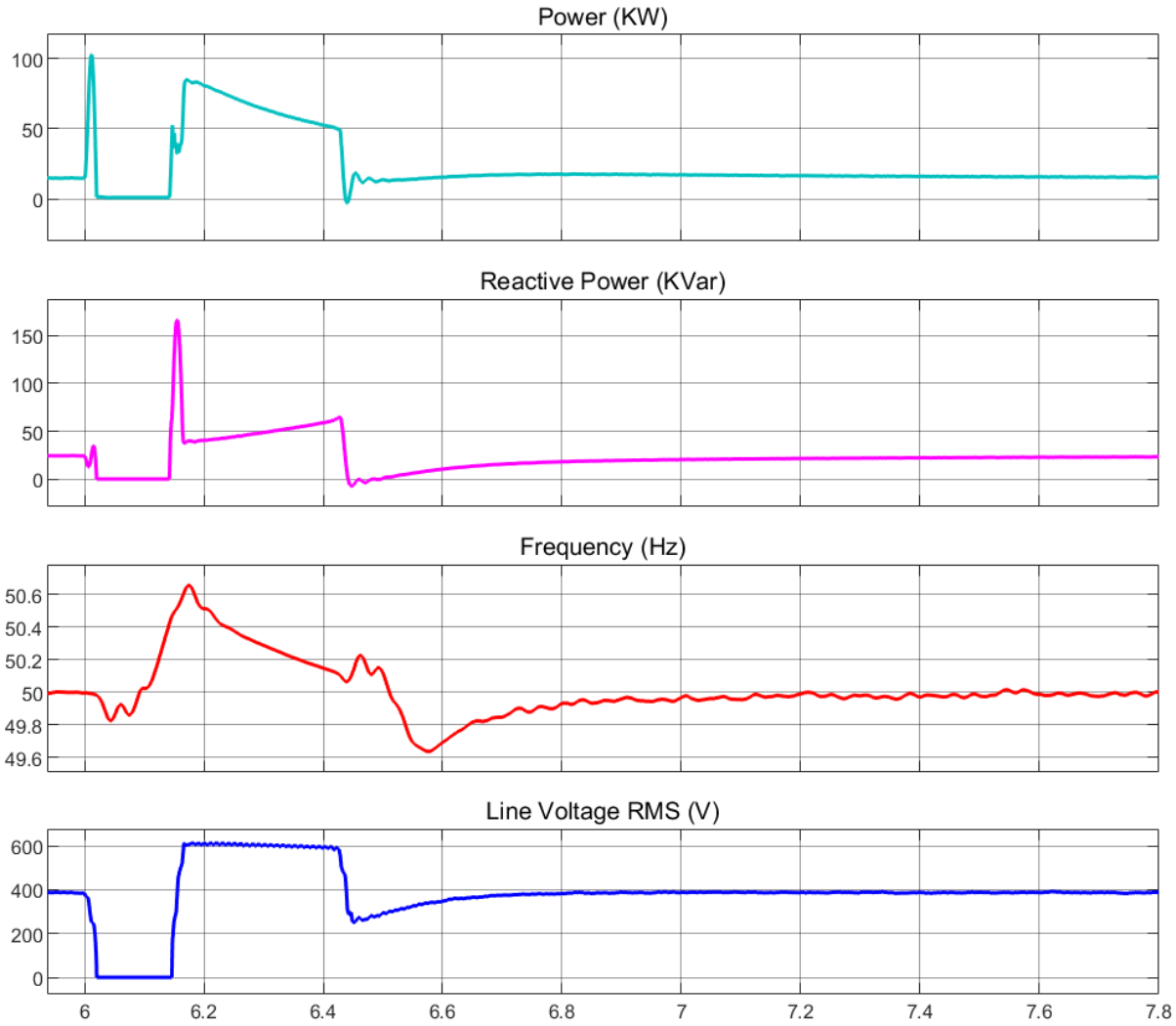


Fig. 6.13: Transient Response in Grid Connected System

6.5 LVRT Compliance – HIL Validation

The low voltage ride through capability is the ability of a system to remain connected to the grid during a momentary fault event on the grid and ride through the transients of the fault without tripping any breakers and return to baseline in the required time frame as specified by the grid code. In New Zealand this is governed by Schedule 8 of the Electricity Participation Code [64] and establishes an envelope that governs the trip and no-trip thresholds.

The system's LVRT capability was evaluated against the New Zealand Grid Code requirements, which specifies the following minimum voltage recovery thresholds: (1). 0.35 pu within 0.5s; (2) 0.76 pu within 1.3s; (3) 0.90 pu within 3.0 s of the post-fault event [64].

Fig. 6.14 shows the voltage recovery trajectory of the grid-connected PV system with proposed smart inverter (blue line). The voltage at PCC reaches 0.98 pu within 0.5s, significantly faster than the minimum requirement. This demonstrates that the system fully satisfies New Zealand LVRT criteria (red line) without requiring any FACTS devices. The system remains connected throughout the event, highlighting the effectiveness of the proposed GFM control strategy during severe fault scenarios.

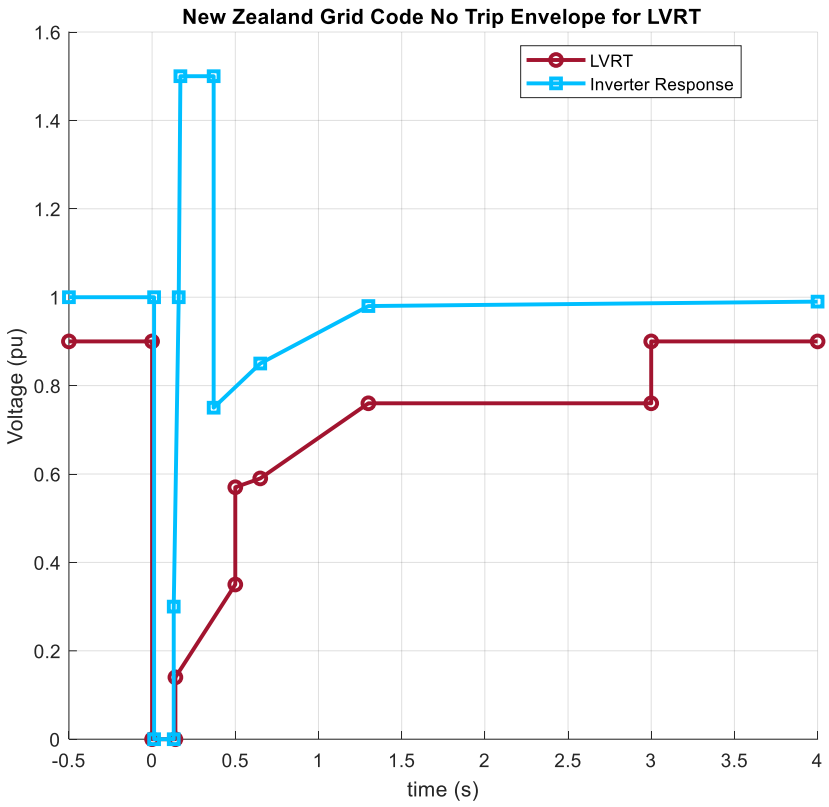


Fig. 6.14: LVRT Capability within the NZ Grid Code No Trip Envelope

6.6 Harmonic Compliance – HIL Validation

Harmonic distortions being a product of the switching harmonics introduced in the early stages of the LCL Filter design have been discussed during the component level system design stage. The allowable total harmonic distortion had been established for the islanded mode during the design of the LCL filter and discussed in detail in chapter 3.4. Table 6.1 summarizes the harmonics response achieved of the droop-controlled inverter in both islanded and grid connected configurations. The islanded harmonics response does not involve any grid dynamics and was determined to be IEEE 519-2022 compliant [63] already in chapter 3. The difference between the AC current waveforms on Fig. 6.6 and Fig 6.11 indicated higher distortions in the current waveform for the grid connected mode, the resulting analysis of which will be presented in this section.

Fig 6.15 illustrates the total harmonic distortion for the steady state current at t = 4.2s over 20 cycles is 5.92%, this increase was as expected from the comparison of the islanded and grid connect waveforms from Fig. 6.6 and Fig 6.11, this increase is still IEEE 519 compliant.

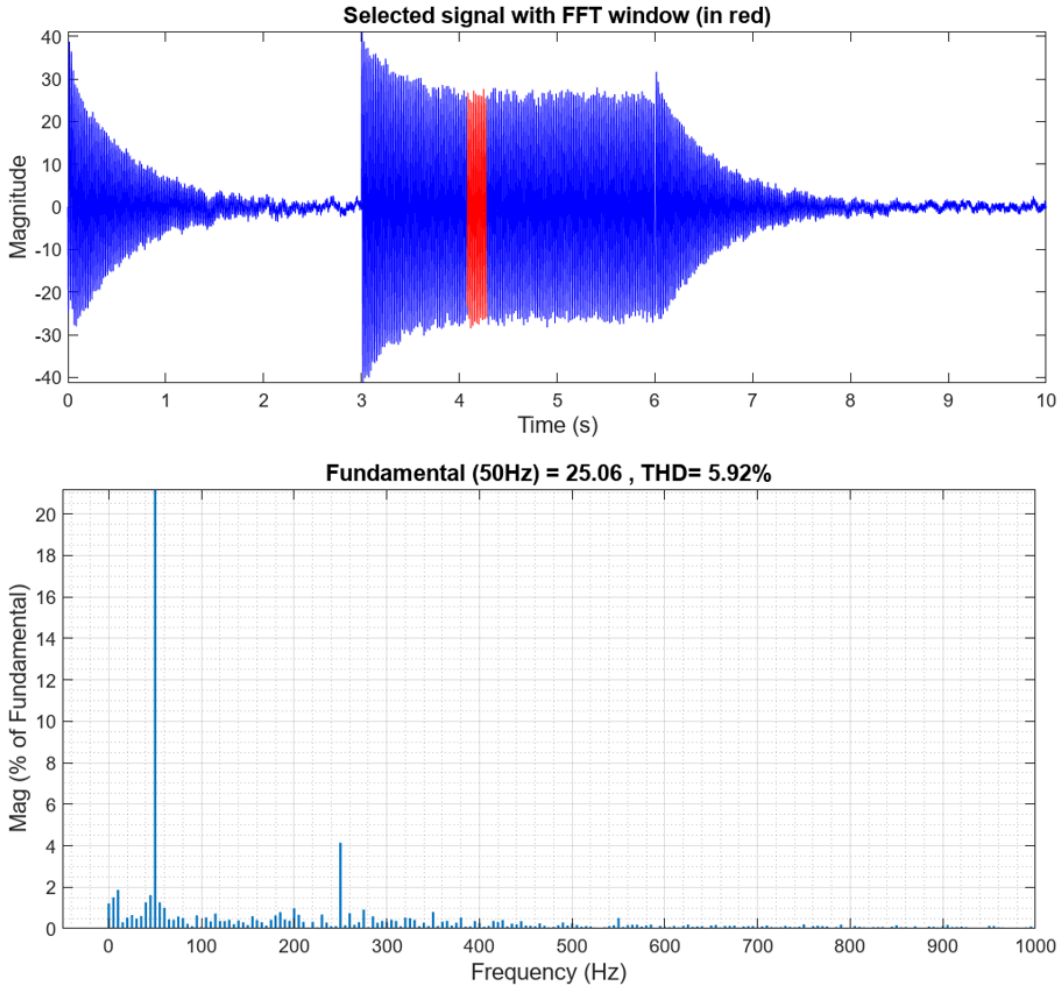


Fig. 6.15: Current Harmonic Analysis for Grid Connect Inverter

Fig 6.16 illustrates the total harmonic distortion for the steady state voltage at t = 4.2s over 20 cycles is 4.99%, this increase was as expected from the comparison of the islanded and grid connect waveforms from Fig. 6.6 and Fig 6.11, this increase takes the voltage up to the compliance threshold but is still considered compliant under IEEE 519 standard [63].

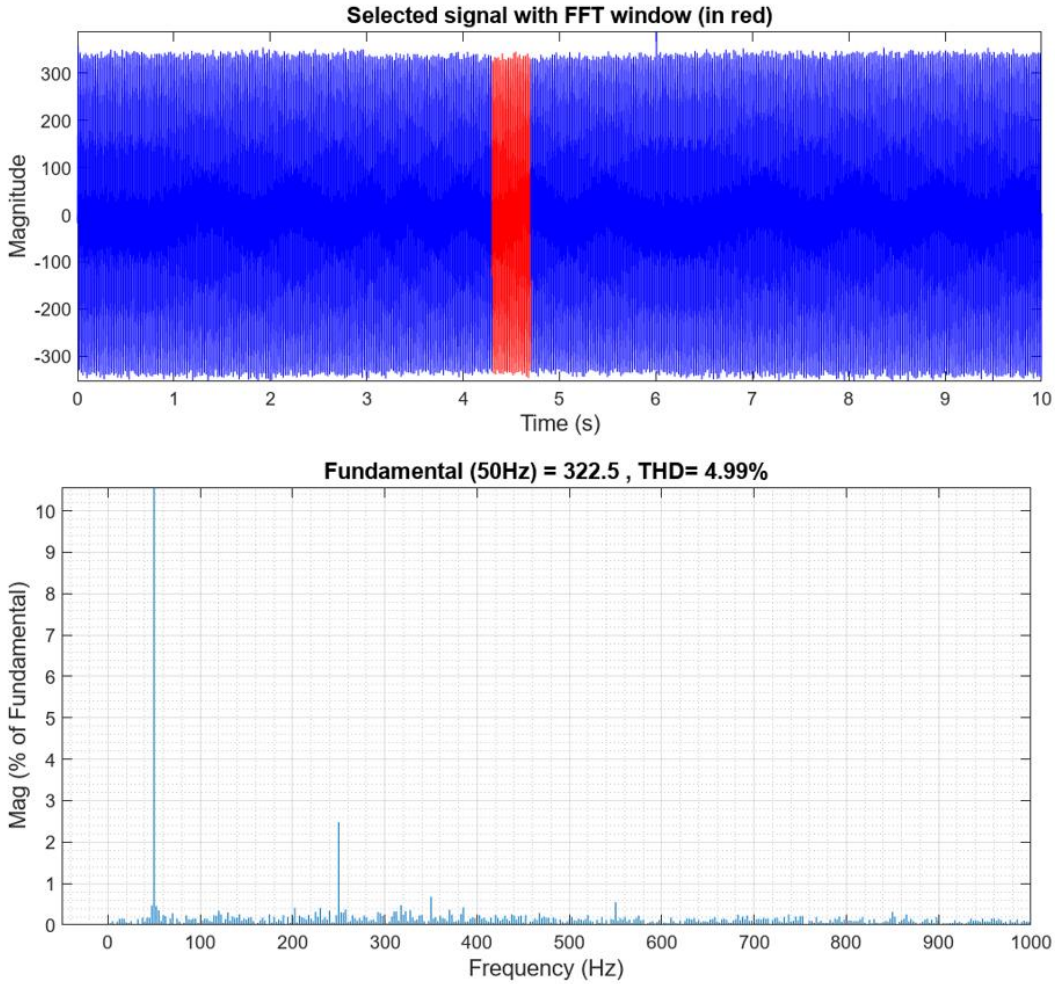


Fig. 6.16: Harmonic Analysis for Grid Connect Inverter

Based on the FFT analysis of both the current and voltage waveforms its can be seen in Fig 6.15 and 6.16 that the 5th order harmonics are still present at ~4.0% for the three-phase current signals and 2.75% for the three-phase voltage signals. The presence of the dominant 5th order components would indicate the outer loop calculations and the inner control loop interactions with the stiff infinite bus that connects the IBR to the grid and since the simulation runs a black start condition each time the model is executed the any simulation mismatch will contribute to the reintroduction of 5th order harmonics and would result in the increased distortions observed. Although the final result was within the tolerance specified each new run produces slightly varying results within 0.02% difference making the outcome slightly non-deterministic and even through the standard would technically assess it as compliant as THD is normally computed on a rolling

window in real power grids. The underlying challenge this highlights is that component level simulation under ideal conditions may not necessarily capture real world behaviour which is an aspect this thesis aimed to directly address or expose based on end-to-end simulation with non-stiff components. However, it must be noted that this thesis is also subject to ideal case simplifications as in the case of infinite bus and ideal grid source, since the goals of this research focused on inverter side design and implementation, extensions of this work to include non-ideal grid sources remain a scope for future research in this domain.

The summary of the harmonic analysis can be found on table 6.1, it must be noted that since the maximum current drawn by the microgrid network was around 80A (rms) and a maximum rated current calculated to ~144A (rms) the islanded and grid connect modes remain low voltage low current application and as such no results were obtained for the high current harmonic distortion and therefore shown as n/a in the table. The steady state load for the islanded connection from section 6.3.2 was used to achieve the island mode THD for voltage and current and the load configuration for steady state grid connected mode from section 6.4.2 was used to generate grid mode THD in table 6.1 to demonstrate that harmonic compliance was met by the inverter to IEEE519 standards.

Table 6.1 Table of IEEE 519 Harmonics Compliance of GFM Inverter

Mode	Total Harmonic Distortion		
	Description	THD %	IEEE 519 %
Island	Voltage (0 < Voltage < 1000V)	4.93	5.0
Island	Low Current (0 < Current < 100)	2.33	8.0
Island	High Current (100 < Current < 1000A)	6.05	15.0
Grid	Voltage (0 < Voltage < 1000V)	4.99	5.0
Grid	Low Current (0 < Current < 100)	5.29	8.0
Grid	High Current (100 < Current < 1000A)	n/a	15.0

6.7 Simulation Results of IEEE 33 Bus System

The baseline IEEE 33 Bus System voltage profile results are compared with the single IBR, the twin IBR and the scaled up single 600kW IBR results are presented in this section.

6.7.1 IEEE 33 Bus System Baseline

Fig. 6.17 illustrates the voltage profile of the IEEE 33 Bus System as a baseline to benchmark the effect of the IBR integration on this network. The figure shows that buses 1 to 5 and buses 19 to 25 would be New Zealand grid compliant [64] and the rest of the buses fall below the 0.95 pu of voltage threshold set by the grid code specification.

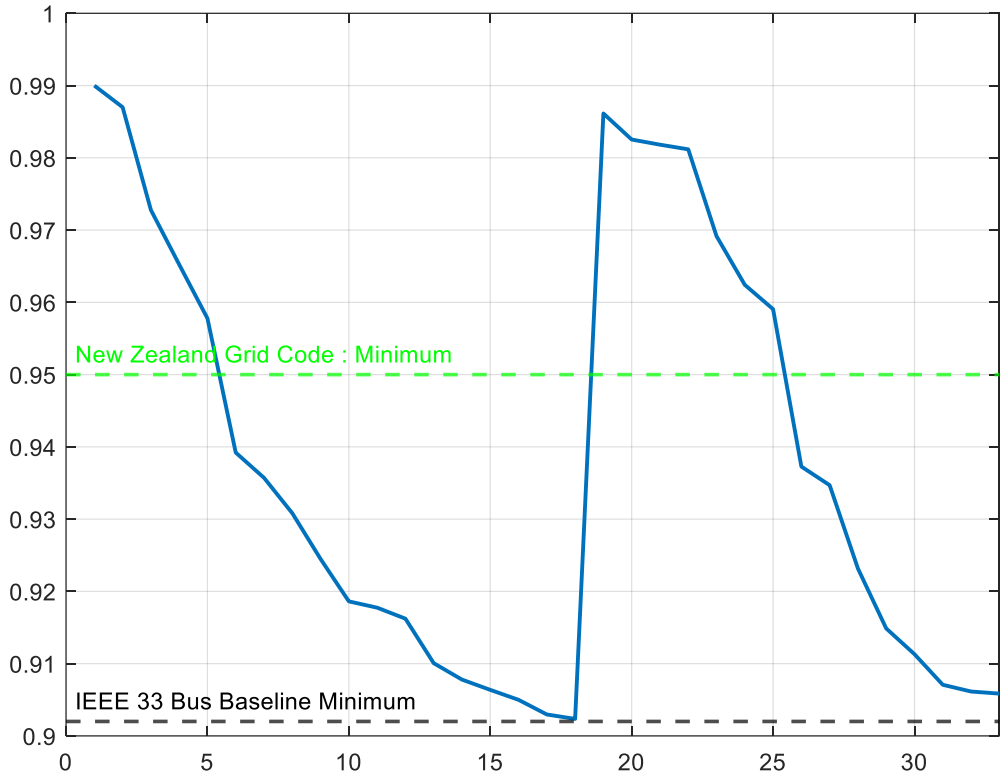


Fig. 6.17: IEEE 33 Bus System Baseline

This benchmark will be used to add the subsequent IBR configurations to the distribution network to investigate the effects on voltage profile. The bus 18 with a bus voltage of 0.902 pu and bus 33 having 0.905 pu are immediately identifiable for ideal candidates for IBR power injection. The bus 18 was identified as the lowest point of the network for IBR integration.

6.7.2 Single IBR on Bus 18

Fig. 6.18 illustrates the effect on voltage profile of the network and shows that one 100kW GFM inverter is not sufficient to make a significant impact on voltage profile. Although technically there is a 1% improvement it would not be sufficient to be grid compliant.

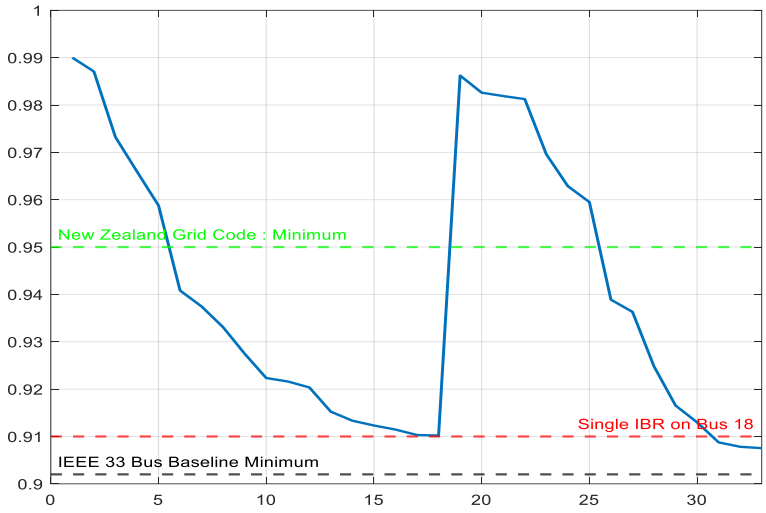


Fig. 6.18: Single GFM IBR on Bus 18

6.7.3 Twin IBR on Bus 18

Fig. 6.19 illustrates the effect on voltage profile of the network a with twin GFM inverter configuration. Even with a total capacity of 200kW, this configuration is not sufficient to make a significant impact on voltage profile. The twin IBR on single bus shows a bus voltage of 0.918 pu marks a less than 1% improvement from the single IBR connection.

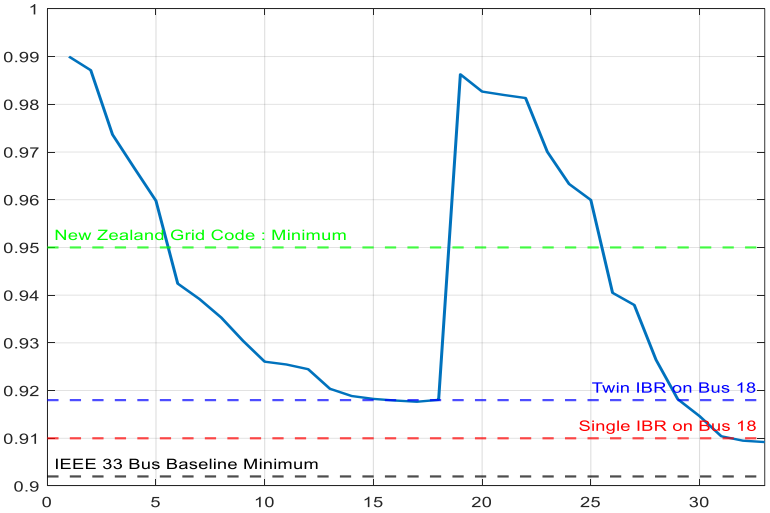


Fig. 6.19: Twin GFM IBR on Bus 18

6.7.4 Grid Integration of Multiple GFM IBR Configuration

Fig. 6.20 illustrates the multi-IBR configuration as it relates to grid compliance in New Zealand. The figure shows that with high penetration of IBR distributed on the tail end of the radial network buses 1 to 28 are New Zealand grid compliant and buses 29 to 33 have remained non-compliant. The scaled-up IBR sizes were kept identical at 600kW each, increasing the size of the IBR on Bus 33 will have the effectively pull the entire 33 bus network into compliance.

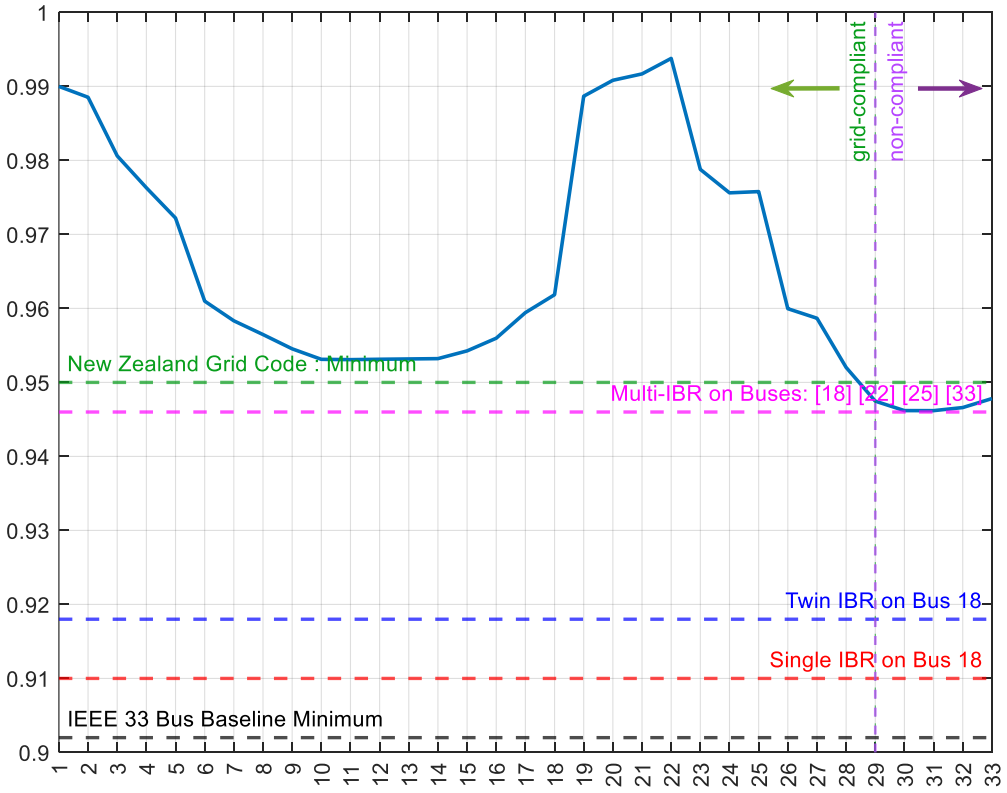


Fig. 6.20: Multiple GFM IBR on IEEE 33 Bus System

6.8 Summary of Results

A summary of the empirical data validates that the GFM IBR implemented in this thesis successfully demonstrates the following characteristics:

1. Frequency and Voltage Regulation Compliant to New Zealand Grid Specification
2. Transient and Steady State Stability of Islanded and Grid Connected Modes
3. Low Voltage Ride Through Compliant to New Zealand Grid Specification
4. Harmonic Stability Compliant with IEEE 519-2022 Standard
5. Steady State Operation when integrated into Radial Distribution Network

The core empirical findings of this thesis presented in this chapter will form the basis of the discussion of the subsequent final two chapters of this thesis. However, because performance metrics were gathered within a controlled simulation environment and their real-world efficacy is fundamentally bound by specific modelling choices. In order to bridge the gap between simulated empirical findings and practical grid deployment, chapter 7 subjects these results to critical evaluation of the underlying assumptions, structural simplifications and engineering limitations.

7 Discussion and Critical Analysis

The empirical findings presented in chapter 6 demonstrate a robust proof of concept for the components required for a high-fidelity end to end model of a grid forming inverter design, all engineering models are defined by their boundary conditions. This chapter contextualizes those results by critically analyzing the structural assumptions, system simplifications and the design limitations inherent to the research framework. By identifying these boundary layers this chapter establishes a transparent hardware translation framework suitable for future testbed designs.

7.1 Model Simplifications and Environmental Assumptions

7.1.1 DC Source Assumptions

In order to use a non-ideal DC source for this thesis research an oversized PV array was selected as discussed in chapter 3.2. Although this allowed for high-fidelity modelling of the inverter side dynamics to investigate the inverter grid dynamics which was the core focus of this research, the DC bus inverter dynamics have not been fully refined. Due to the model performance limitations of the simplified BESS design, the system takes the environmental assumption of operating under full solar irradiance conditions which will not be realistic for any practical design. This remains to subject to future evaluation and analysis, a preliminary account of which is presented in this section.

In practice, any major disturbances that cause the DC bus voltage to dip will cause a corresponding harmonic distortion of the current supplied to the grid due to the instantaneous power balance required within the inverter. Fig 7.1 show the effect of a DC Bus voltage dip due to non-ideal irradiation conditions on the PV array and highlight the importance of DC Bus voltage management for a grid connect PV system.

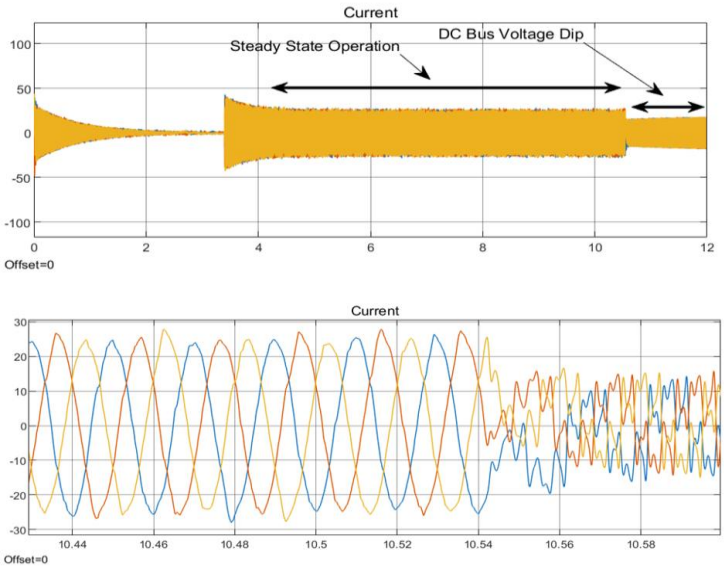


Fig. 7.1: DC Bus Induced Harmonics on Grid Current

As the DC bus voltage dips the inverter the sufficient DC headroom necessary to produce the intended AC voltage waveform this creates PWM errors which when combined with control non linearities that result in the injection of harmonics back into the grid. Future research that implements a detailed model of a BESS over the simplified bi-directional DC-DC converter can seek to address this issue. The steady state grid connect load configuration from chapter 6.4.2 together with deliberately stalling the MPPT controller of the PV array such that the DC input voltage of the inverter terminals dipped by approximately 10% was used to demonstrate the dip grid current and the harmonics induced in Fig. 7.1 above.

7.1.2 IGBT Dead Time Compensation

A physical implementation will need to account for the time between switching of one pair to the switching on of the complementary pair of IGTB gates and will affect the design of the SPWM generation stage. Besides output waveform distortions due introduced low order harmonics into the system, in droop control any waveform distortions will introduce errors in the power calculation stage. A biased P and Q measurements can shift the droop operating point such that uneven real and reactive power sharing can occur with parallel operated inverters.

These effects were excluded in order to manage the scope of this research and as such although non-ideal IGBT characteristics were considered, the generic IGBT model was used in the modelling of the implemented inverter design without any dead-time constraints.

7.1.2 Hardware and Software Simplifications

Any physical implementation of a GFM IBR will need to account for line impedances and power losses on the system which in this research was simplified. Detailed studies of the losses involved, and system optimizations required for commercial viability was not studied in this thesis and remains subject to future research in this domain. In addition to losses measurements in practical systems will have latency due to the physical implementation of the digital signal processing (DSP) control hardware and any latency in measurement will affect the power calculations required for the droop control to function correctly. The implementation simply uses the MATLAB and the OPAL -RT HIL environment to build and run the models with its internal latency of measurements handled by the system. Any practical implementation of this GFM inverter will require selection of DSP and sensors hardware with specifications that can accommodate the high speed and high-power measurement requirements for a power inverter.

7.2 Physical and Operational Limitations

7.2.1 Hunting Oscillations

The implementation of the GFM IBR for this thesis focuses on the design of a single inverter to be operated in islanded and grid connected modes and the HIL validation results produced are reflective of this constraint. However, operating multiple parallel connected IBRs on a single bus of the grid requires the addressing of the specifics of the identical interconnected IBRs and affects the stability margins of the operated parallel system. In the condition were parallel interconnected IBRs approach the stability limit and deviations in line impedances, incorrectly tune droop parameters of the voltage and current controllers and excessive droop gains can result in real and reactive power PQ and voltage oscillations known as hunting oscillations [71]. This phenomenon can be deterministic in terms of if it occurs but non-deterministic in terms of when it can show up in a system and can depend on a multitude of factors such as R/X ratios, SCR, small signal disturbances such as step changes in load and overall grid strength [72].

During the implementation phase of the results that correspond to the twin IBR configuration on a single bus of a radial distribution network the two instances of the implemented GFM IBR were connected in parallel with identical parameters and hunting oscillations were discovered as a consequence of connecting the parallel configuration to a stiff infinite bus modelled for the system testing as established in the literature [72]. This behavior was also non-deterministic as individual runs of the system model would cause the oscillations to occur at different times. This phenomenon was also only exhibited on the isolated bus where the system operated in islanded mode connected to a fixed test load that was created greater demand than single GFM IBR could supply by itself. This hunting oscillations did not occur in grid connect modes and the problem had to be solved to continue with the investigation of the distributed GFM IBR on the IEEE 33 Bus network.

Two approaches were attempted to resolve this issue, the first approach involved reducing the droop gains of the controller to try and illuminate the hunting oscillations. This did successfully manage to remove the hunting phenomenon but involved having tradeoffs in voltage and frequency regulation. The eigen value analysis showed that single and parallel GFM IBR configurations have different stability margins that any practical design must accommodate with the inclusion of gain tuning or the use of more advanced droop gain selection methods such as non-linear droop gain curves. The second approach of removing the hunting oscillations was to increase the bus impedance by addition of a small series RL circuitry to the network. In practice there will always exist bus impedances that must be accounted for and in this instance the introduction of bus impedances in the form of slightly oversized transformers was used to remove the oscillations from the simulation and show stable behavior in parallel configurations. This was done in order to preserves the droop gains required to meet the grid constraints for

frequency and voltage regulation even in parallel configurations, but the tradeoff here would be additional losses incurred with the inclusion of the series resistance with the added bus impedance. The steady state operation and harmonic analysis were conducted to ensure the voltage and current waveforms were able to meet the compliance criteria set out for this implementation.

Identical droop gains allow for equal power sharing between inverters but in practice inverters with different power capacities will result in over-utilization of smaller inverters and under-utilization larger inverters. This was simplified in this research with the use of identical power rated inverters to control the test conditions for comparing the results of the single inverter and parallel inverter results. In practice, no two GFM IBRs will be perfectly identical due to slight variations in line impedances, component tolerances and sensor tolerances can introduce circulating currents between the inverters leading to inefficiencies due to power loss in the form of heat that will need to be dissipated by the inverters and degrade internal components over time.

Fig. 7.2 illustrates the discovery and the process of eliminating the hunting oscillations from the implementation. The figure shows the observed oscillations (top left), the $PQfV$ effects of the added series impedance (top right) and parallel GFM IBR equal power sharing (bottom right) and the removal of harmonic distortion (bottom right).

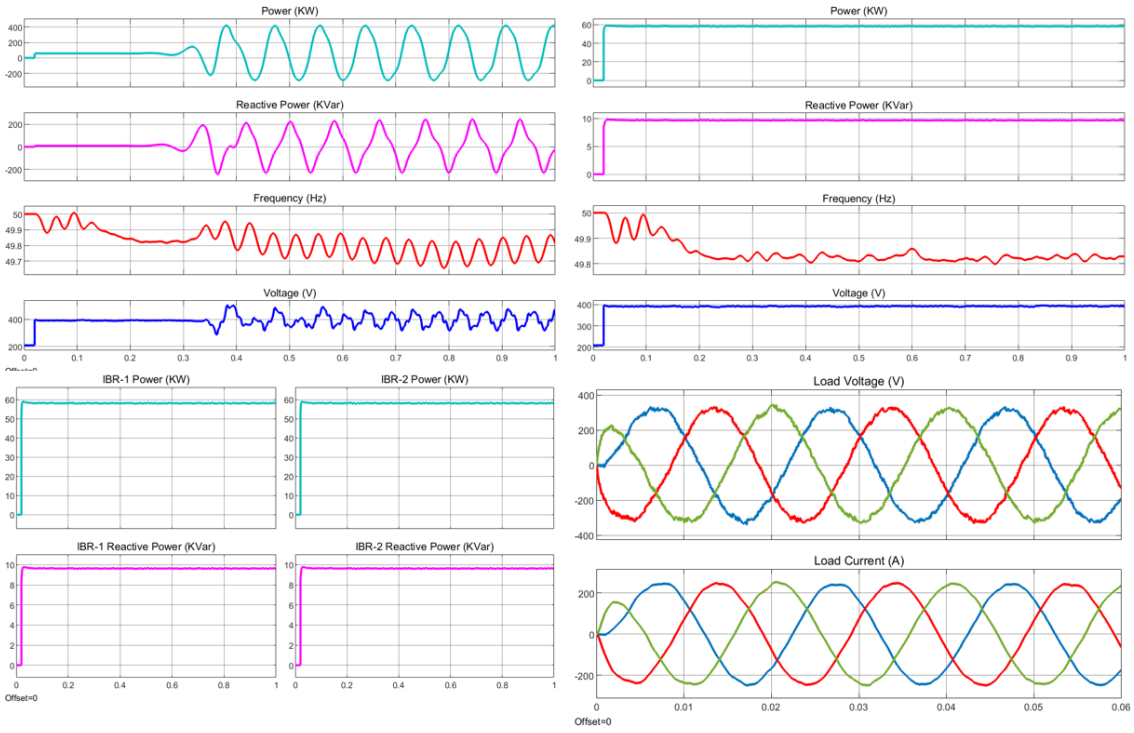


Fig. 7.2: Hunting Oscillations Debugging

Although the solution for the observed oscillation phenomenon was resolved by the addition of bus impedance, at better solution would be the addition of advanced active damping control loop with the droop control to eliminate these behaviors and achieve stability in strongly connected systems remains subject for future research.

Consequently, the parallel inverter oscillations, present stiff isolated bus connections that are not observed in weak grid conditions would indicates that as the distributed multiple GFM IBR configuration improves the strength of a localized grid sub-network the inverters may then introduce a stability problem of their own making as each inverter measures the power flow on the grid and tries to respond with the proportional amount of droop response resulting in N times the regulation response where is the number of parallel inverters, this overshoot of the nominal setpoint will then generate a regulating response proportionally larger than what the overshoot requires as each parallel inverter attempts to generate the entire regulation response by itself. Although this response is not present in distributed deployment of single GFM IBR, in commercial operations the deployment parallel connected GFM IBRs will be necessary for modularity and scalability and incorporating redundancy and reliability required to effectively operate a business. The modular parallel GFM IBR deployment are essential for black start operation where the individual inverters gradually bring up capacity and schedule dispatch by gradually by connecting loads in step with generation capacity on individual islanded sub-networks and as each island is formed, they are subsequently interconnected so that wider grid is formed.

7.2.2 Grid Synchronization

The final limitation that needs to be addressed in order to meet real world application is synchronization. The implemented system demonstrated grid forming characteristics abilities under controlled simulated environment of MATLAB and OPAL-PT HIL platform, however real grid integration will require pre-synchronization procedures. In order to demonstrate that a GFM IBR will in practice be able to black start the grid by generating its own internal reference signals and running the simulation inherently simulated black start conditions was sufficient for simulation purposes. Additionally implementing an automated PLL based pre- synchronization procedure where the grid parameters are measured and feed into the droop control loop for initial synchronization before the grid breakers are closed to connect the GFM IBR to the grid was excluded from the scope of this research. This is because in practice the grid synchronization process is highly dependent on grid conditions at the time of connection for any real-world deployment of GFM inverters and since the simulations used ideal grid conditions for testing the inverter side dynamics, this step could be excluded without significant impact on the results of this thesis.

7.3 Critical Analysis

The deployment of the implemented GFM IBR on a radial distribution network successfully demonstrated steady state operability and autonomous power sharing without requiring inter-inverter communication. However, under black-start conditions within an islanded sub network, this autonomy creates a unique operational challenge. If every GFM IBR simultaneously attempts to form the islanded grid without a coordination framework, the resulting uncoordinated energization leads to competing voltage references. This conflict triggers immediate protection schemes, collapsing the island into a blackout before stable grid conditions can be established. Repeated, automated attempts to black start the system under these conditions could ultimately damage the underlying power electronics. Consequently, this scenario exposes the absolute operational limits of the autonomous power sharing methodologies presented both in this thesis and the wider literature.

The wider implications for operating multiple parallel GFM IBRs in DER configurations on radial distribution networks as would be the case for smaller commercial rooftop applications, are highlighted in this limitation. A network of variably rated and vendor agnostic, single and parallel interconnected GFM IBRs in real world grid scenarios will require the implementation of tunable internal parameters such as droop gain and high-fidelity modelling of the system for analysis such as the Australian AEMO R1 and R2 modelling requirements as established in the literature review [46]. The discovery of this limitation highlights the significance of end-to-end HIL validated modelling approach demonstrated in this research. Under these industry standards, simplified linear or basic average models are insufficient and architectures must demonstrate both steady state operation and transient resilience against severe network faults while accurately reflecting the dynamics of control interactions. However, pursuing this level of industrial-grade modelling fidelity naturally introduces severe computational and numerical boundaries that must be balanced with the scope of research for depth and significance of its findings.

The limitations analyzed in this chapter specifically regarding the physical and operational limitations and the tradeoffs represent the foundational engineering tradeoffs to any high-fidelity model validation pipeline where the grid stability assessment at the macroscopic level must be carefully balanced with the power electronic non linearities at the component level. A core focus of this research was the execution of end-to-end real-time HIL validation to bridge the theoretical domain with physical operation.

In conclusion, while the system simplifications, model constraints and underlying assumptions identified in this chapter define the operational boundaries of the implemented GFM IBR, they do not invalidate the core performance trends established in the empirical results. Instead, these boundary conditions provide the exact

engineering constraints required to safely transition this framework from a simulation model to a physical testbed. The empirical data validated and its practical limitations thoroughly contextualized, chapter 8 summarizes the overarching contributions of this research and outlines a concrete roadmap for future implementation.

8 Conclusions and Future Research

This thesis has investigated the design and implementation of an end-to-end GFM inverter and explored its operation under transient and steady state conditions in islanded and grid connected modes. Throughout this research, a comprehensive framework has been systematically developed, moving from analytical mathematical derivations to rigorous simulation-based stress testing. This final chapter aggregates the core conclusions of this study, formally evaluates the fulfilment of the primary research objectives, and defines the structural roadmap for subsequent development in this domain.

8.1 Fulfilment of Research Objectives

In alignment with the overarching aim of this research, this thesis successfully bridged the gap between conceptual control loop topology and real time HIL anchored platform. To achieve an industrial grade validation environment, the developed framework progressed from decoupled mathematical abstractions into a fully integrated, end-to-end power systems architecture. Specifically, the realized system design successfully incorporated a non-linear solar PV array model acting as the DC source, interfacing directly with a dynamically constrained droop controlled GFM inverter. This generation block was initially embedded within a localized microgrid network supported by an infinite bus utility grid topology to establish steady state baseline performance. To evaluate practical scalability and weak grid resilience, the entire architecture was further integrated into a highly complex radial distribution network characterized by the standardized IEEE 33 Bus network.

The transition from pure software simulation to a physical real-time HIL platform was achieved by mapping the mathematical control structures onto the OPAL-RT real time HIL platform. The system architecture was then subjected to rigorous operational transitions, proving robust operability in both grid connected and intentional islanded microgrid modes. The GFM IBR, while connected to the infinite bus topology was able to demonstrate precise active and reactive power tracking while providing vital localized voltage support.

The GFM IBR assets were then embedded into the IEEE 33-Bus radial distribution network. The research successfully evaluated the scalability of decentralized control under high renewable penetration scenarios. The impact of a single GFM IBR integration on the tail end of the distribution network was investigated to demonstrate the steady state operability of the system. The 33 Bus network baseline voltage profile was used to determine the strategic placement of multiple GFM IBR assets on the identified weak busses of network, in order to demonstrate both the improvements on voltage profile of the system and the autonomous power sharing capabilities of droop control inverter designs without the need for external communication between inverters.

8.2 Synthesis of Empirical Contributions

Following the structural realization of the real time HIL testbed architecture, the empirical data compiled across extensive transient and steady-state simulation trials provides definitive, quantitative validation of the developed grid forming control framework. Rather than relying on idealized mathematical assumptions, the performance metrics extracted from the HIL platform capture the true dynamic responses of the inverter-based resource as it confronts real world grid anomalies and structural topologies. The resulting dataset provides a rigorous empirical foundation proving that decentralized, communication-less GFM architectures can successfully execute autonomous voltage and frequency regulation. The localized, high-fidelity findings established in Chapter 6 are synthesized across three critical performance domains in both islanded and grid connected operational modes highlighting the quantitative victories of the implemented GFM IBR system.

The critical performance domains are as follows:

1. Frequency Regulation
2. Voltage Regulation and LVRT
3. Decentralized Autonomous Power Sharing and Stability

The primary empirical data confirms the ability of the implemented 100kW GFM capable smart inverter to maintain precise frequency and voltage regulation under transient and steady state operating conditions. The inverter could also provide fault tolerance with the ability to survive a 140 ms three phase short fault and return to the pre-fault steady state operating conditions once the fault was cleared without the need for external FACTS devices or triggering load shedding schemes, in both islanded and grid connected modes. This robust prototype ready design represents a key contribution of this thesis.

8.3 Industrial and Regulatory Significance

This represents the current trend of renewable energy integration into the power grid moving away from large, centralized power generation feed by fossil fuel based synchronous machines to a distributed network supplied by smaller utility scale generation. In DER configurations as long, radial feeders experience a high penetration of renewable energy, utility companies globally need to overcome severe operational challenges regarding low system inertia, voltage volatility, and weak grid conditions. The end-to-end implementation and HIL validation compiled in this thesis provide direct industrial and regulatory value in the mitigation of the associated stability challenges with the integration of renewable energy sources on to the power grid.

The ability to provide frequency and voltage regulation, fault tolerance in the form of ride through capabilities and compliance with grid constraints without reliance on external inter-inverter communications at the sub-megawatt utility scale represents a major

milestone in industrial deployment as nation states strive for 100% renewable energy integration. Commercially deployment of vendor agnostic IBR network that integrate renewable energy to the power grid in a universal plug and play GFM interoperability as of 2026 has not been achieved in industry. The research compiled in this thesis take a step in that direction in alignment with industrial modelling requirements that are currently being developed or adopted across the globe.

When viewed from a regulatory standpoint, the connection of utility scale IBRs to the power grid requires fulfilling stringent pre-connection modelling benchmarks that validate transient and steady state stability before commissioning is approved. This thesis directly bridges the gap between conceptual control engineering and commercial connection procedures. Embedding a 100 kW GFM IBR into a real time HIL platform and subjecting them to a worst case 140 ms three-phase short circuit fault, this work provides a verified, industry aligned testing methodology. It proves that GFM assets can satisfy strict LVRT grid codes while operating under the realistic hardware emulation and computational constraints.

The high-fidelity end to end simulation preserved the systemic stiffness of the system and was able to expose adverse active and reactive power oscillations. The uncovering of these volatile interactions underscores the diagnosing and solving of real-world physical dynamics. These critical latencies remain unexposed in unconstrained ideal simulations. Analysis of these oscillation boundaries provide the power system industry with crucial, actionable insights into precise control loop tuning and predictive firmware compensation.

8.4 Recommendations for Future Research

This thesis focused on the inverter side dynamics of a GFM IBR and investigated the constraints underlying the integration of such inverters with the power grid. Although this established valuable empirical insights and implications discussed in this thesis, the grid side dynamics were modelled as stiff infinite bus supported by an ideal grid or ideal slack bus as per industry established benchmarks. The true behavior of such GFM inverters can only be fully established when tested under specific grid conditions of real grids under real operating conditions. The improvements to this research established in the previous chapter notwithstanding, it is the position of this thesis that any scope for future research incorporate the inclusion of non-ideal grid and realistic grid conditions to further build upon the research of this thesis.

References

1. International Energy Agency. (2025, June 6). *Global energy investment set to rise to $3.3 trillion in 2025 amid economic uncertainty and energy security concerns*. https://www.iea.org/news/global-energy-investment-set-to-rise-to-3-3-trillion-in-2025-amid-economic-uncertainty-and-energy-security-concerns

2. S. Hasheminasab, M. Alzayed, and H. Chaoui, "A review of control techniques for inverter-based distributed energy resources applications," Energies, vol. 17, no. 12, p. 2940, 2024.

3. W. Freitas, J. C. M. Vieira, A. Morelato, L. C. P. da Silva, V. F. da Costa and F. A. B. Lemos, "Comparative analysis between synchronous and induction machines for distributed generation applications," in *IEEE Transactions on Power Systems*, vol. 21, no. 1, pp. 301-311, Feb. 2006.

4. IEEE Standard for Interconnection and Interoperability of Distributed Energy Resources with Associated Electric Power Systems Interfaces," in IEEE Std 1547-2018 (Revision of IEEE Std 1547-2003), vol., no., pp.1-138, 6 April 2018.

5. X. Gao, D. Zhou, A. Anvari-Moghaddam, and F. Blaabjerg, "A comparative study of grid-following and grid-forming control schemes in power electronic-based power systems," Power Electronics and Drives, vol. 8, no. 1, pp. 1–20, 2023.

6. D. Ibram and V. Gueorgiev, "Reactive power compensation in grid connected photovoltaic system using static synchronous compensator," in Proc. 2021 13th Electrical Engineering Faculty Conf. (BulEF), Sep. 2021, pp. 1–5.

7. Y. Yuan, J. Zhou, Y. Zhang, X. Zhao, and G. Xu, "Low-capacitance cascaded H-bridge STATCOM for full power operation," Journal of Power Electronics, vol. 22, no. 2, pp. 287–296, 2022.

8. Fortune Business Insights. (2026, January). Grid-Forming Inverter Market Size & Forecast. https://www.fortunebusinessinsights.com/grid-forming-inverter-market-109817

9. Australian Energy Regulator. (2022, June 28). AER Media News Release, AGL Penalties for Breaching Energy Rules.

10. Australian Energy Regulator. (2016, September 28). System Blackout Compliance Report.

11. International Renewable Energy Agency (2025), Renewable Energy Statistics 2025.

12. International Energy Agency (2023), World Energy Outlook Report 2023.

13. Ministry of Business Innovation & Employment (2025), Energy in New Zealand 2025. https://www.mbie.govt.nz/building-and-energy/energy-and-natural-resources/energy-statistics-and-modelling/energy-publications-and-technical-papers/energy-in-new-zealand

14. National Energy System Operator (2019), Technical Report of Events of 9 August 2019.

15. North American Electric Reliability Corporation (2017), 1200MW Fault Induced Solar Photovoltaic Induced Disturbance Report, June 2017.

16. Transpower New Zealand (2020), Transpower Transmission Planning Report 2020.

17. S. F. Zarei, H. Mokhtari, M. A. Ghasemi, S. Peyghami, P. Davari and F. Blaabjerg, "Control of Grid-Following Inverters Under Unbalanced Grid Conditions," in *IEEE Transactions on Energy Conversion*, vol. 35, no. 1, pp. 184-192, March 2020.

18. Y. Li, Y. Gu and T. C. Green, "Revisiting Grid-Forming and Grid-Following Inverters: A Duality Theory," in *IEEE Transactions on Power Systems*, vol. 37, no. 6, pp. 4541-4554, Nov. 2022.

19. A. Sajadi, J. A. Ranola, R. W. Kenyon, B. -M. Hodge and B. Mather, "Dynamics and Stability of Power Systems with High Shares of Grid-Following Inverter-Based Resources: A Tutorial," in *IEEE Access*, vol. 11, pp. 29591-29613, 2023.

20. B. Wen, D. Boroyevich, R. Burgos, P. Mattavelli and Z. Shen, "Analysis of D-Q Small-Signal Impedance of Grid-Tied Inverters," in *IEEE Transactions on Power Electronics*, vol. 31, no. 1, pp. 675-687, Jan. 2016.

21. A. Askarian, J. Park and S. Salapaka, "Enhanced Grid-Following (E-GFL) Inverter: A Unified Control Framework for Stiff and Weak Grids," in *IEEE Transactions on Power Electronics*, vol. 39, no. 5, pp. 5089-5107, May 2024.

22. J. Sun, "Impedance-Based Stability Criterion for Grid-Connected Inverters," in *IEEE Transactions on Power Electronics*, vol. 26, no. 11, pp. 3075-3078, Nov. 2011.

23. B. Wen, D. Dong, D. Boroyevich, R. Burgos, P. Mattavelli and Z. Shen, "Impedance-Based Analysis of Grid-Synchronization Stability for Three-Phase Paralleled Converters," in *IEEE Transactions on Power Electronics*, vol. 31, no. 1, pp. 26-38, Jan. 2016.

24. J. Matevosyan *et al.*, "A Future with Inverter-Based Resources: Finding Strength from Traditional Weakness," in *IEEE Power and Energy Magazine*, vol. 19, no. 6, pp. 18-28, Nov.-Dec. 2021.

25. National Energy System Operator (2020), National Grid ESO debuts Dynamic Containment frequency response service. https://www.neso.energy/news/national-grid-eso-debuts-dynamic-containment-frequency-response-service

26. J. Rocabert, A. Luna, F. Blaabjerg and P. Rodríguez, "Control of Power Converters in AC Microgrids," in *IEEE Transactions on Power Electronics*, vol. 27, no. 11, pp. 4734-4749, Nov. 2012.

27. S. Hadavi, M. Z. Mansour and B. Bahrani, "Optimal Allocation and Sizing of Synchronous Condensers in Weak Grids with Increased Penetration of Wind and Solar Farms," in *IEEE Journal on Emerging and Selected Topics in Circuits and Systems*, vol. 11, no. 1, pp. 199-209, March 2021.

28. Australian Energy Market Operator, AEMO System Security Planning – Inertia Requirements Methodology Report December 2024.

29. Busby, J. W., Baker, K., Bazilian, M. D., Gilbert, A. Q., Grubert, E., Rai, V., ... & Webber, M. E. Cascading risks: Understanding the 2021 winter blackout in Texas. Energy Research & Social Science, 77, 102106, 2021.

30. P. Zafari, A. Zangeneh, M. Moradzadeh, A. Ghafouri, and M. A. Parazdeh, "Various Droop Control Strategies in Microgrids," in Microgrid Architectures, Control and Protection Methods, Cham, Switzerland: Springer, 2020, pp. 527–554.

31. Gurugubelli V, Ghosh A, Panda AK, Rudra S. Implementation and comparison of droop control, virtual synchronous machine, and virtual oscillator control for parallel inverters in standalone microgrid. *Int Trans Electr Energy Syst*. 2021.

32. M. C. Chandorkar, D. M. Divan and R. Adapa, "Control of parallel connected inverters in standalone AC supply systems," in IEEE Transactions on Industry Applications, vol. 29, no. 1, pp. 136-143, Jan.-Feb. 1993.

33. M. Ferrari, L. M. Tolbert and E. C. Piesciorovsky, "Grid Forming Inverter with Increased Short-Circuit Contribution to Address Inverter-Based Microgrid Protection Challenges," in *IEEE Open Journal of the Industrial Electronics Society*, vol. 5, pp. 481-500, 2024.

34. S. D'Arco, J. A. Suul, and O. B. Fosso, "A Virtual Synchronous Machine implementation for distributed control of power converters in Smart Grids," Electric Power Syst. Res., vol. 122, pp. 180–197, 2015.

35. Q. -C. Zhong, P. -L. Nguyen, Z. Ma and W. Sheng, "Self-Synchronized Synchronverters: Inverters Without a Dedicated Synchronization Unit," in *IEEE Transactions on Power Electronics*, vol. 29, no. 2, pp. 617-630, Feb. 2014.

36. Q. -C. Zhong and G. Weiss, "Synchronverters: Inverters That Mimic Synchronous Generators," in *IEEE Transactions on Industrial Electronics*, vol. 58, no. 4, pp. 1259-1267, April 2011.

37. C. Arghir, T. Jouini, and F. Dörfler, "Grid-forming control for power converters based on matching of synchronous machines," Automatica, vol. 95, pp. 273–282, 2018.

38. G. -S. Seo, M. Colombino, I. Subotic, B. Johnson, D. Groß and F. Dörfler, "Dispatchable Virtual Oscillator Control for Decentralized Inverter-dominated Power Systems: Analysis and Experiments," *2019 IEEE Applied Power Electronics Conference and Exposition (APEC)*, Anaheim, CA, USA, 2019, pp. 561-566.

39. L. Harnefors, M. Bongiorno and S. Lundberg, "Input-Admittance Calculation and Shaping for Controlled Voltage-Source Converters," in *IEEE Transactions on Industrial Electronics*, vol. 54, no. 6, pp. 3323-3334, Dec. 2007.

40. A. Rashwan, A. Mikhaylov, T. Senjyu, M. Eslami, A. M. Hemeida, and D. S. Osheba, "Modified droop control for microgrid power-sharing stability improvement," Sustainability, vol. 15, no. 14, p. 11220, 2023.

41. W. Cai, R. Mallik and B. Johnson, "Singular-perturbation-based Control Design of Single-phase Grid-forming Inverters," *2024 IEEE Energy Conversion Congress and Exposition (ECCE)*, Phoenix, AZ, USA, 2024, pp. 893-900.

42. IEEE Data Port, "Integrated IEEE 33-Bus Distribution and Transmission Test System (CLARC-Based)," IEEE Data Port. [Online]. Available: https://ieee-dataport.org/documents/integrated-ieee-33-bus-distribution-and-transmission-test-system-clarc-based.

43. M. E. Baran and F. F. Wu, "Network reconfiguration in distribution systems for loss reduction and load balancing," *IEEE Trans. Power Del.*, vol. 4, no. 2, pp. 1401–1407, Apr. 1989.

44. S. H. Dolatabadi, M. Ghorbanian, P. Siano and N. D. Hatziargyriou, "An Enhanced IEEE 33 Bus Benchmark Test System for Distribution System Studies," in *IEEE Transactions on Power Systems*, vol. 36, no. 3, pp. 2565-2572, May 2021.

45. A. S. Hassan, Y. Sun, and Z. Wang, "Multi-objective for optimal placement and sizing DG units in reducing loss of power and enhancing voltage profile using BPSO-SLFA," *Energy Rep.*, vol. 6, pp. 1581–1589, 2020.

46. Australian Energy Market Operator "Power System Model Guidelines", 2025. https://www.aemo.com.au/energy-systems/electricity/national-electricity-market-nem/participate-in-the-market/network-connections/modelling-requirements

47. David Narang, Sig Gonzalez, Jay Johnson (2022). DOE Laboratory Support for DER and Inverter-Based Resource Integration Standards (ACCEL II) Final Report

48. Transpower New Zealand, "Preparing for an Increase in Inverter Based Resources" 2021. https://static.transpower.co.nz/public/bulk-upload/documents/Preparing%20for%20an%20increase%20in%20inverter-based%20resources%20v1.0.pdf?VersionId=bLFY0dB4Za1FfNAEh1V_75DOZ3_vmPb5

49. Australian Energy Market Operator, "Application of Advanced Grid-scale Inverters in the NEM" 2021. https://aemo.com.au/-/media/files/initiatives/engineering-framework/2021/application-of-advanced-grid-scale-inverters-in-the-nem.pdf

50. L. Li, Y. Sun, Z. Liu, X. Yuan, M. Su, X. Hou, and M. Zheng, "A series-parallel PV-storage independent microgrid and its decentralized control," *International Transactions on Electrical Energy Systems*, vol. 29, no. 2, p. e2715, Feb. 2019.

51. S. Pant and R. P. Saini, "Comparative Study of MPPT Techniques for Solar Photovoltaic System," *2019 International Conference on Electrical, Electronics and Computer Engineering (UPCON)*, Aligarh, India, 2019, pp. 1-6.

52. Y. Wang, Y. Li and X. Ruan, "High-Accuracy and Fast-Speed MPPT Methods for PV String Under Partially Shaded Conditions," in *IEEE Transactions on Industrial Electronics*, vol. 63, no. 1, pp. 235-245, Jan. 2016.

53. H. S. Salama, A. Ali, and K. Mahmoud, "Adaptive control for microgrid frequency stability integrating battery energy storage and photovoltaic," Scientific Reports, vol. 15, no. 1, p. 43839, 2025.

54. P. Jivaganont, P. Limthongkul, and J. Mongkoltanatas, "Profitability of battery energy storage system coupled with photovoltaic at behind-the-meter," Journal of Energy Storage, vol. 121, p. 116357, 2025.

55. S. H. Chen, C. T. Chen, and Y. F. Lin, "Dual-coupled-inductor-based high-step-up boost converter with active-clamping and zero-voltage switching," Energies, vol. 17, no. 9, p. 2018, 2024.

56. A. Sangwongwanich, Y. Yang, D. Sera, F. Blaabjerg and D. Zhou, "On the Impacts of PV Array Sizing on the Inverter Reliability and Lifetime," in *IEEE Transactions on Industry Applications*, vol. 54, no. 4, pp. 3656-3667, July-Aug. 2018.

57. A. A. R. Mohamed, R. J. Best, X. Liu and D. J. Morrow, "A Comprehensive Robust Techno-Economic Analysis and Sizing Tool for the Small-Scale PV and BESS," in *IEEE Transactions on Energy Conversion*, vol. 37, no. 1, pp. 560-572, March 2022.

58. G. Ning *et al.*, "Single-Stage IIOS Converter with Auto-Voltage-Sharing for Distributed Photovoltaic MVDC Collection System," in *IEEE Transactions on Power Electronics*, vol. 39, no. 11, pp. 14172-14178, Nov. 2024.

59. A. S. Alzahrani, "Two-Phase IPOS DC-DC Step-up Converter for PV Interface," *2022 International Conference on Electrical, Computer and Energy Technologies (ICECET)*, Prague, Czech Republic, 2022.

60. M. Liserre, F. Blaabjerg and S. Hansen, "Design and control of an LCL-filter-based three-phase active rectifier," in *IEEE Transactions on Industry Applications*, vol. 41, no. 5, pp. 1281-1291, Sept.-Oct. 2005.

61. H. Cha and T. -K. Vu, "Comparative analysis of low-pass output filter for single-phase grid-connected Photovoltaic inverter," *2010 Twenty-Fifth Annual IEEE Applied Power Electronics Conference and Exposition (APEC)*, Palm Springs, CA, USA, 2010, pp. 1659-1665.

62. J. M. Sosa, G. Escobar, P. R. Martínez-Rodríguez, G. Vázquez, M. A. Juárez and M. Diosdado, "Comparative evaluation of L and LCL filters in transformer less grid tied converters for active power injection," *2014 IEEE International Autumn Meeting on Power, Electronics and Computing (ROPEC)*, Ixtapa, Mexico, 2014, pp. 1-6.

63. "IEEE Standard for Harmonic Control in Electric Power Systems" in *IEEE Std 519-2022 (Revision of IEEE Std 519-2014) - Redline*, vol., no., pp.1-52, 5 Aug. 2022.

64. Electricity Authority, “Electricity Industry Participation Code 2020 – Schedule 8” Common Quality Requirements. https://www.ea.govt.nz/code-and-compliance/the-code-electricity-industry-participation-code-2010/

65. Electricity Authority, “The governance and management of harmonics in New Zealand’s power system” Consultation Paper June 2024.

66. J. C. -H. Peng, G. Raman, J. L. Soon and N. D. Hatziargyriou, "Droop-Controlled Inverters as Educational Control Design Project," in *IEEE Transactions on Power Systems*, vol. 37, no. 2, pp. 1623-1633, March 2022

67. J. M. Guerrero, J. C. Vasquez, J. Matas, L. G. de Vicuna and M. Castilla, "Hierarchical Control of Droop-Controlled AC and DC Microgrids—A General Approach Toward Standardization," in *IEEE Transactions on Industrial Electronics*, vol. 58, no. 1, pp. 158-172, Jan. 2011.

68. M. A. Awal, H. Yu, S. Lukic, and I. Husain, “Droop and oscillator-based grid-forming converter controls: A comparative performance analysis,” *Front. Energy Res.*, vol. 8, p. 168, Jul. 2020.

69. Y. Lu, W. Bu, Q. Chen, P. Qiu, and Y. Tian, “Model Order Reduction and Stability Enhancement Control for AC/DC Converters Through State Feedback Method,” *Electronics*, vol. 13, no. 23, p. 4760, Nov. 2024.

70. OPAL-RT Technologies Canada, manuals library, “OP-5700 User Manual” https://www.manualslib.com/manual/1748291/Opal-Rt-Op5700.html?page=1#manual

71. J. Swartz, F. Celi, F. Pasqualetti and A. Von Meier, "Parameter Conditions to Prevent Voltage Oscillations Caused by LTC-Inverter Hunting on Power Distribution Grids," *2022 European Control Conference (ECC)*, London, United Kingdom, 2022, pp. 1118-1125.

72. B. Cao, G. Chen, W. Chen and X. He, "Anti-Tap Hunting Coordination of Q-V Droop with OLTC/SVR on R/X-Heavy Feede," *2025 3rd Power Electronics and Power System Conference (PEPSC)*, Kuala Lumpur, Malaysia, 2025, pp. 88-93.